Electron Transport in Photon and Electron Beam Modelling

Paul J. Keall, M.Sc.

Thesis submitted for the degree of

Doctor of Philosophy

in the University of Adelaide

Department of Physics and Mathematical Physics

Supervisors:

Dr Peter W. Hoban

Dr John R. Patterson

July 1996

Contents

Abstract

To address the deficiencies of currently available dose calculation algorithms for radiotherapy planning, two rigorous dose calculation methods have been devised.

The first method incorporates Fermi-Eyges multiple scattering theory into the primary dose calculation of the superposition method for external X-ray beam radiotherapy. The inclusion of scattering theory into the superposition technique accounts for the density *distribution* between the primary photon interaction and energy deposition sites, whereas conventional superposition methods only consider the average density between these two points. This method gives depth dose curves which show better agreement with Monte Carlo calculations in a lung phantom than a standard superposition method, especially at high energies and small field sizes where lateral electronic disequilibrium exists. For a 5×5 cm^2 18 MV beam incident on the lung phantom, a reduction in the maximum error between the superposition and Monte Carlo depth dose curves from 5% to 2.5% is obtained when scattering theory is used in the primary dose calculation.

The second method developed is the Super-Monte Carlo (`SMC`) method. `SMC` calculates dose by a superposition of pre-generated Monte Carlo electron track kernels. For X-ray beams, the primary dose is calculated by transporting pre-generated (in water) Monte Carlo electron tracks from each primary photon interaction site. The length of each electron step is scaled by the inverse of the density of the medium at the beginning of the step. Because the density scaling of the electron tracks is performed for each

individual transport step, the limitations of the macroscopic scaling of kernels (in the superposition algorithm) are overcome. The scatter dose is calculated by superposition. In both a lung-slab phantom and a two lung-block phantom, SMC dose distributions are more consistent with 'standard' Monte Carlo generated dose distributions than are superposition dose distributions.

SMC can also be applied to electron beam dose calculation. Pre-generated electron tracks are transported through media of varying density and atomic number. The perturbation of the electron fluence due to each material encountered by the electrons is explicitly accounted for by considering the effect of variations in stopping power, scattering power and radiation yield. For each step of every electron track, these parameters affect the step length, the step direction and the energy deposited in that step respectively. Dose distributions in a variety of phantoms show good agreement with Monte Carlo results.

SMC is an accurate, 3-dimensional unified photon/electron dose calculation algorithm.

Statement

This thesis contains no material which has been accepted for the award of any other degree or diploma in any university or other tertiary institution, and to the best of my knowledge and belief, contains no material previously published or written by another person, except where due reference has been made in the text.

I give consent to this copy of my thesis, when deposited in the University Library, being available for loan and photocopying.

SIGNED: DATE: 15/08/1996

Acknowledgements

Firstly, I wish to warmly thank my primary supervisor, Dr Peter Hoban. Peter's enthusiasm, ideas and solutions to my many problems have been invaluable throughout this project. His hard work and knowledge of the radiation physics have enabled me to complete this degree, attend conferences and have heaps of fun in the meantime!

I am grateful for the supervision and guidance of Assoc Prof Alun Beddoe. Up to his departure for England, Alun was helpful and supportive in many ways: an outstanding research team leader. Alun's departure for Birmingham was a huge loss to the Department.

Thanks also to Dr John Patterson for organisational and beauracratic help, and proof reading this thesis.

Martin Ebert has been an inspiration and motivation for me during this research. His ability to learn, and his incredible work output gave me impetus whenever I needed it. He has also helped me with many problems and proof read much work throughout the thesis. As well as Martin, the other staff of the Medical Physics Department at the Royal Adelaide Hospital have all been very helpful, and I have thoroughly enjoyed their company.

Some of the experimental results in this thesis come from Dr Peter Metcalfe at the

Illawarra Cancer Care Centre. Thanks both for the results, and the hospitality shown on my visits to Wollongong. Also, I appreciate the permission of the authors whose figures are included in this thesis.

The person who in my undergraduate degree enticed me into medical physics, supervised my work at the University of Waikato, and written for me successful grant applications and references is Dr Howell Round. Thanks for all the time and effort!

Thanks must go to my immediate family for their support from across the Tasman, lots of mail, and the fun arguments from physics to religion. Thanks also to the people who have put up with me in Adelaide, kept me sane (and sometimes insane): Yazza, D^2, Nawana, Liz, Les and the members of the Adelaide University Rugby club and Adrian and the members of the Tae Kwon Do clubs of South Australia.

I acknowledge the financial assistance of the National Health and Medical Research Council grant no. 940650, and an Australian Postgraduate Award, without which this project would not have taken place.

This work is dedicated to Brooke, Matthew and Rhys, my three favourite children, who I see far too little of. May the world look after them.

Symbols and Abbreviations

Symbols

A	atomic weight
D	absorbed dose
D_p	primary dose
D_s	scatter dose
E	electron kinetic energy or photon energy
E'	the largest possible energy of photons emitted in electron-electron bremsstrahlung events
E_{dep}	energy in an electron step deposited in the medium
E_{en}	amount of kinetic energy absorbed by the medium
E_{rad}	the amount of energy radiated away in an electron step
E_s	binding energy of an electron
E_{tot}	total energy lost in an electron step
E_{tr}	amount of kinetic energy transferred to electrons of the medium from a photon interaction
$\mathcal{F}$	Fourier transform operation
H	energy deposition kernel
I	mean excitation energy
K	kerma
K_c	collision kerma
L_Δ	restricted collision stopping power
$L_{\Delta',rad}$	restricted radiative stopping power
M_A	molar mass of substance A
N	number of incident particles
N_A	Avogadro's number
$P(\theta_x, x, z)$	probability distribution function of scattered particles
R_γ	ratio of CT to electron density number
S	total stopping power
S_{col}	collisional stopping power
S_{rad}	radiative stopping power
T	terma
T_s	scattering power
W_{air}	average energy required to produce an ion pair in air
X_0	radiation length

Z	atomic number
c	velocity of light in a vacuum
d	physical depth
d'	radiological depth
d_{max}	depth of maximum dose
e	electron charge
g	fraction of energy of secondary charged particles lost to bremsstrahlung
h	Planck's constant
$h\nu$	photon energy
k	energy of photon emitted in the bremsstrahlung process
l	thickness or length
m_e	electron rest mass
n	number of atoms per unit volume
r	ratio of actual cross section to Rutherford value
r'	effective radius
r_e	classical electron radius
u	atomic mass unit
x	lateral position on the x-axis
y	lateral position on the y-axis
z	depth in medium
Γ	attenuation coefficient for the photoelectric effect
Δ	cut off energy for collisional interactions
Δ'	cut off energy for radiative interactions
Φ	particle fluence or azimuthal scattering angle
Φ_E	fluence of particles of energy E
Ψ	energy fluence
Ψ_E	energy fluence of particles of energy E
Ω	polar scattering angle
α	fine structure constant or azimuthal angle
α'	$Z\alpha$
β	ratio of the velocity of the electron to that of light in a vacuum
δ	density effect correction
θ	polar scattering angle
θ_m	cut-off angle
θ_μ	screening angle
θ_x	scattering angle projected onto the x-axis
κ	attenuation coefficient for pair production
λ	ratio of photon energy to electron rest energy ($h\nu/m_e c^2$)
μ	linear attenuation coefficient
μ_{en}	energy absorption coefficient
μ_{tr}	energy transfer coefficient
ν	velocity
ρ	mass density
ρ'	effective density
ρ_e	electron density
ρ_{ew}	fraction of the electron density of water
ρ_e^w	electron density relative to water
ρ_{ave}	average density
σ	atomic cross section

σ_c	attenuation coefficient for the Compton effect
σ_e	electron-electron bremsstrahlung cross section
σ_n	electron-nucleus bremsstrahlung cross section
σ_s	scattering cross section
τ	ratio of the kinetic energy of the electron to the rest energy
φ	particle fluence rate
ψ	energy fluence rate

Abbreviations

CCC	Collapsed Cone Convolution
CF	correction factor
ETAR	Equivalent Tissue-Air Ratio
FE	Fermi-Eyges multiple scattering theory
FWHM	full-width-half maximum
GS	Goudsmit-Saunderson multiple scattering theory
Gy	unit of dose (1 Joule per kilogram)
ICRU	International Commission on Radiation Units and Measurements
keV	kilo-electron Volts
linac	linear accelerator
MeV	Mega-electron Volts
MMC	Macro-Monte Carlo
MV	Megavoltage
PSE	Phase Space Evolution
SAR	Scatter-Air Ratio
SMC	Super-Monte Carlo
SSD	Source-Surface Distance
TAR	Tissue-Air Ratio
VMC	Voxel-based Monte Carlo

Preface

The cause of over a quarter of deaths in Australia is cancer.[1]

Radiotherapy is the treatment option for approximately half of patients with cancer.[2] The aim of radiotherapy is to deliver a prescribed amount of radiation to the tumour in order to kill all the clonogenic cells with minimal complication (radical treatments) or to relieve pain for terminally ill patients (palliative treatments). About half of the radiotherapy patients are treated radically, and of these about half achieve uncomplicated local tumour control.[2] Radiotherapy is optimised when a high dose is delivered to the tumour to increase tumour control probability whilst dose to healthy tissue is minimised, thus reducing normal tissue complication probability. Clinical studies have shown that because of the high dependency of tumour control and normal tissue complication on dose, the accuracy requirement for dose delivered is approximately 5%.[3] Due to the uncertainties associated with other aspects of treatment,[1] the required accuracy in dose calculation is 2%.[5]

Near interfaces of high to low densities (eg. near the muscle/lung interface) where electronic disequilibrium may exist during irradiation, most current clinically used X-ray beam dose calculation algorithms can give errors of over 10%,[6] and electron beam algorithms can give errors of up to 40%.[7] The Monte Carlo method of dose calculation[8, 9]

[1]The sources of uncertainties are found in the calibration of the treatment machine, the characterisation of the beams, the day-to-day positioning of the patient, and the consistency of the patient's geometry.[4]

achieves the required accuracy, but is too computationally intensive to use routinely in a clinical environment. The aim of the research presented in this thesis was to produce a dose calculation algorithm which agrees with experimentally measured dose distributions to within the 2% guideline, and is also computationally viable in a clinical situation.

In chapter 1 of this thesis the physics of electrons and photons at therapeutic energies are introduced. The following chapter outlines the dose calculation methods for both photon and electron beam planning, along with their advantages and limitations.

Chapter 3 details the incorporation of Fermi-Eyges multiple Coulomb scattering theory[10] into the superposition algorithm. Resulting dose distributions are compared to those generated using standard superposition calculations.

The Super-Monte Carlo method of X-ray beam dose calculation is discussed in chapter 4, where the scatter dose component is calculated by a standard superposition method (incorporating a scatter energy deposition kernel), whilst pre-generated Monte Carlo electron tracks replace the kernel for the primary dose calculation.

In chapter 5 the Super-Monte Carlo method is applied to electron beams, where the problems of variations in stopping power, scattering power and radiation yield in different materials are discussed, as well as how these problems are overcome in Super-Monte Carlo.

The final chapter summarises the main findings of this thesis, the benefits and limitations of the new dose calculation algorithms, and explores future research options resulting from this work.

The publications and presentations with which the author has been involved with during the course of this research are:

Publications

- P. J. Keall and P. W. Hoban. Accounting for primary electron scatter in X-ray beam convolution calculations. *Med. Phys.*, **22**(9) 1414-1418, 1995.

- P. J. Keall and P. W. Hoban. An accurate 3-D X-ray dose calculation method combining superposition and pre-generated Monte Carlo electron track histories. *Med. Phys.*, **23**(4) 479-485 1996.

- P. J. Keall and P. W. Hoban. A review of electron beam dose calculation algorithms. *Aust. Phys. Eng. Sci Med.*, (In press) 1996.

Submitted manuscripts

- P. J. Keall and P. W. Hoban. Super-Monte Carlo: An accurate 3-D electron beam dose calculation algorithm. Submitted to *Med. Phys.*, December 1995.

- M. A. Ebert, P. W. Hoban and P. J. Keall. Modelling clinical accelerator beams: A review. Submitted to *Aust. Phys. Eng. Sci Med.*, February 1996.

Published Conference Presentations

- P. J. Keall and P. W. Hoban. Super-Monte Carlo. A combined approach to X-ray beam planning. *Med. Phys.* **22**(6) 930, American Association of Physicists in Medicine (AAPM) Conference, Boston 1995.
  ◇ Awarded 2nd prize in the AAPM Young Investigators Competition

- P. J. Keall and P. W. Hoban. Super-Monte Carlo for electron beam planning. *Med. Phys.* **22**(9) 1544, AAPM Conference, Boston 1995 (poster).

Unpublished Conference Presentations

- P. J. Keall and P. W. Hoban. Convolution: Scaling the primary kernel. *Engineering and Physical Sciences in Medicine (EPSM) Conference Proceedings* p 94, Perth 1994.

- P. J. Keall, P. W. Hoban and P. E. Metcalfe. The future of radiotherapy dose calculations. *Clinical Oncology Society of Australia Conference Proceedings* p 114.8, Adelaide 1994.

- P. J. Keall and P. W. Hoban. Super-Monte Carlo. A combined approach to X-ray beam planning. *EPSM Conference Proceedings* p 118, Queenstown 1995.
  ◇ Awarded Varian prize for the best radiotherapy presentation

- P. J. Keall and P. W. Hoban. Super-Monte Carlo for electron beam planning. *EPSM Conference Proceedings* p 233, Queenstown 1995 (poster).

Other Presentations

- P. J. Keall and P. W. Hoban. Super-Monte Carlo. A combined approach to X-ray beam planning. *South Australian branch of the Australasian College of Physical Scientists and Engineers in Medicine (ACPSEM) Student Presentation Night*, Adelaide 1995.
  ◇ Awarded ACPSEM Airfare Grant

- P. J. Keall and P. W. Hoban. Super-Monte Carlo for electron beam planning. *IEAust, SMBE and ACPSEM (SA branch) Annual Student Paper Night*, Adelaide 1995.

Chapter 1

Photon and Electron Physics at Therapeutic Energies

1.1 Introduction

Photons of medically useful energies (≈10 keV to 50 MeV) interact with electrons and nuclei of matter, producing fast moving electrons and positrons, and other photons. Fast moving electrons (and positrons) interact with matter to produce further fast moving electrons and photons. Electrons deposit energy in matter by causing both atomic and molecular excitations and ionisations. The free electrons, and excited ions and molecules lead to further excited molecules, ion-recombination and chemical bond breaking. In biological systems, these processes can cause base damage and breaks in DNA strands in cells. This damage can sometimes be repaired, but if not, cell death or mutations may occur. In the radiotherapy treatment of cancer, radiation is used to kill proliferating altered cells. It is ironic that in radiotherapy, radiation, a known carcinogen, is used to

treat cancer.

In this chapter, the physics of photon and electron transport, and electron energy deposition are discussed.

1.2 Photon interactions

1.2.1 Introduction

In terms of frequency of occurrence, and importance for energy deposition, the three predominant photon interactions with nuclei and electrons of the irradiated medium at medical energies are Compton scattering, photoelectric absorption and pair production. Rayleigh scattering, triplet production, photonuclear reactions and other interactions can also occur, but the probabilities of these interactions are low, and do not affect the energy deposition on a macroscopic scale.

1.2.2 Compton scattering

In Compton scattering, the incident photon interacts with an electron of the irradiated medium, giving the electron kinetic energy, and also producing a scattered photon, as shown in figure 1.1. For photons with energies from 200 keV to 2 MeV this is the only interaction of importance which occurs in soft tissues.[11] The probability of interaction via Compton scattering is dependent on the electron density of the absorbing medium.[12]

Ignoring the effect of the binding energy of the electron ($\ll$ energy of the incident pho-

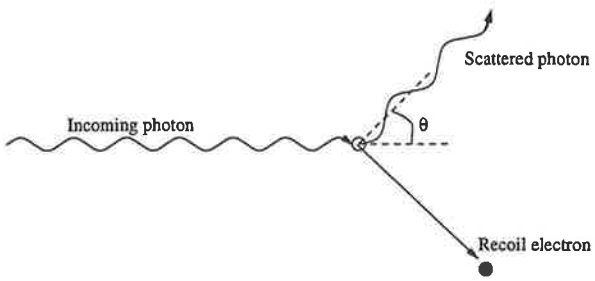

Figure 1.1: **Schematic representation of the Compton process**

ton), the cross section per unit solid angle, $d\sigma/d\Omega$ (refer section 1.2.5), is given by the Klein-Nishina formula[13]

$$\frac{d\sigma}{d\Omega} = \frac{r_e^2}{2}\left(1+cos^2\theta\right)\left[\frac{1}{1+\lambda\left(1-cos\theta\right)}\right]^2\left[1+\frac{\lambda^2\left(1-cos\theta\right)^2}{\left[1+\lambda\left(1-cos\theta\right)\right]\left(1+cos^2\theta\right)}\right], \quad (1.1)$$

where λ $(=h\nu/m_ec^2)$ is the ratio of the energy of the photon to the rest energy of the electron, r_e is the classical electron radius and θ is the polar angle between the incoming and scattered photons. The scattered photon can also interact with the absorbing medium. In Compton scattering, as the incident photon energy increases, the average fraction of energy passed to the electron increases, and also the direction of the recoil electron becomes more forward directed.

1.2.3 Photoelectric absorption

In the photoelectric process a photon of energy $h\nu$ collides with one of the bound electrons in the K, L, M or N shells of an atom, which is subsequently ejected, as shown in figure 1.2. The ejected photoelectron emerges with energy $h\nu - E_s$ where E_s is the binding energy of the electron. The atom is left in an excited state, and emits *characteristic radiation*[1]

[1]The hole created by the ejected electron is filled by an electron from an outer shell. The energy lost in this transformation is emitted as a photon.

and *Auger electrons*[2] as it returns to the ground state. The photoelectric process is most likely to occur if the energy of the photon is just greater than the binding energy of the electron,[11] and hence is important for photon energies below 100 keV. Photon energies less than the binding energy are not energetic enough to eject an electron. Therefore the cross section varies with energy in a complicated way with discontinuities at the energy corresponding to each shell or subshell. However, in general, the cross-section for photoelectric interactions is proportional to Z^3-Z^4 (Z is the atomic number of the absorbing medium).[12] The energy deposited in a photoelectric collision in tissue can be assumed to be absorbed locally (at the point where the photon interacted).[11]

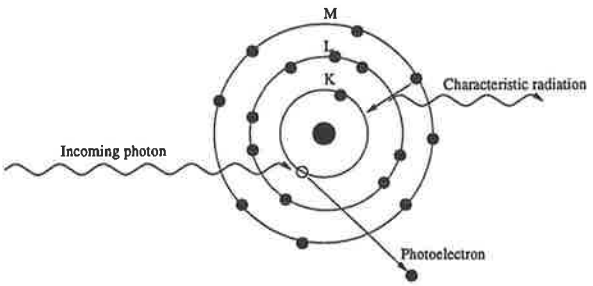

Figure 1.2: **Schematic representation of the photoelectric process.**

1.2.4 Pair production

When the energy of the incident photon is sufficiently high, the photon may undergo a pair production interaction. In this interaction, an electron-positron pair is generated from a photon as it passes near the strong Coulomb field of the nucleus of an atom as shown in figure 1.3. Since the rest mass energy of the positron and electron are both 0.511 MeV, the photon must have an incident energy > 1.02 MeV to create the pair. The excess energy is shared (not necessarily equally) between the positron and electron as kinetic energy. This process is considered as a collision between the photon and the

[2]In some cases the characteristic radiation is absent, or of reduced intensity, and electrons are emitted in its place.

nucleus, and in the collision the nucleus recoils with some momentum.[11] The nucleus also acquires a little energy, but this is negligible compared to the energy given to the positron and electron. Pair production becomes increasingly important at higher photon energies. The cross section per atom for pair production is dependent on Z^2, and hence varies with Z per mass.[12]

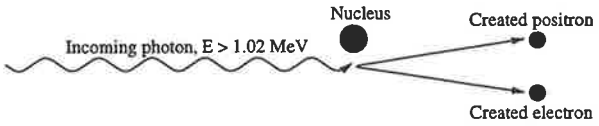

Figure 1.3: **Schematic representation of the pair production process.**

The positron produced in pair production travels through matter exciting and ionising atoms in the same way as an electron, and loses energy until it is brought to rest. The positron combines with a free electron and is annihilated, producing two photons (at $\approx 180^{\circ}$ to each other, thus conserving momentum) of energy 0.511 MeV, as shown in figure 1.4.

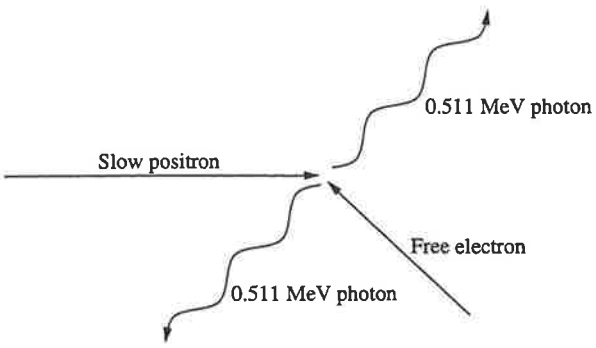

Figure 1.4: **Schematic representation of annihilation photon production.**

1.2.5 Attenuation coefficients

The probability of an incoming photon interacting with an atom of the absorbing medium is given by the energy dependent atomic cross-section, σ. The interactions photons undergo are governed by quantum probability, and consequently the interaction site cannot be accurately predicted. Statistical uncertainties are eliminated however when interaction probabilities are determined per unit spatial dimension. Hence, the linear attenuation coefficient, μ, is defined as the fraction of photons, dN/N expected to interact per unit thickness of attenuator, dl,

$$\mu = \frac{dN}{Ndl}. \tag{1.2}$$

The total cross section of an atom is the sum of the cross sections of the Compton, photoelectric and pair production cross sections. Therefore the attenuation coefficient is the sum of the attenuation coefficients for each interaction type, ie the Compton effect, σ_c, the photoelectric effect, Γ, and pair production, κ,

$$\mu = \sigma_c + \Gamma + \kappa. \tag{1.3}$$

It is often convenient to use the *mass* attenuation coefficient, μ/ρ instead of μ.

To calculate the energy given to charged particles at an interaction site from a beam of photons (refer section 1.2.7) the energy transfer coefficient, μ_{tr}, is needed. The energy transfer coefficient is the fraction of photons that interact per unit thickness multiplied by the fraction of energy of the photons transferred to the medium. The ICRU[14] define the energy transfer coefficient as

$$\mu_{tr} = \frac{1}{NE}\frac{dE_{tr}}{dl}, \tag{1.4}$$

where E_{tr} is the amount of kinetic energy of the photon transferred to electrons of the

medium.

To determine the energy absorbed by a medium from a photon interaction, the bremsstrahlung energy radiated away by the electron set in motion at the interaction site needs to be subtracted from the energy transferred in the photon interaction,

$$\mu_{en} = \mu_{tr}(1 - g), \tag{1.5}$$

where g is the fraction the electron energy that is lost to bremsstrahlung in the medium. As the radiative cross section increases with electron energy, g increases with photon energy (in water $g = 0$ for 1 MeV photons and 0.05 for 10 MeV photons[11]).

1.2.6 Fluence

The concept of fluence is independent of particle type, and therefore applies for both incident electrons and photons. The particle fluence, Φ, is the quotient of dN by da, where dN is the number of particles incident on a sphere of cross sectional area da,

$$\Phi = \frac{dN}{da}. \tag{1.6}$$

The energy fluence, Ψ, is the quotient of dR by da, where dR $(= EdN)$ is the radiant energy incident on a sphere of cross sectional area da,

$$\Psi = \frac{dR}{da}. \tag{1.7}$$

Where the incident particles vary in energy, the particle fluence is obtained by

$$\Phi = \int_E \Phi_E dE, \tag{1.8}$$

where Φ_E is the fluence of particles of energy E. Similarly the energy fluence for a spectrum of incident particles is

$$\Psi = \int_E \Psi_E dE. \tag{1.9}$$

The particle fluence rate, φ, and the energy fluence rate, ψ, can be determined by taking the derivative with respect to time of Φ and Ψ respectively.

1.2.7 Kerma

The transfer of energy from a photon beam to a medium takes place in two stages, (i) the interaction of a photon, causing an electron to be set in motion, and (ii) the transfer of energy from the fast-moving electron to the absorbing medium by excitations and ionisations. To describe the first stage of this process the ICRU define kerma, K, as the *kinetic energy released per unit mass.* Kerma is the amount of kinetic energy given to electrons at a photon interaction site per unit mass, and is given by

$$K = \frac{d\overline{E}_{tr}}{dm} = \Phi \left(\frac{\mu}{\rho}\right) \overline{E}_{tr}, \tag{1.10}$$

where $\overline{E}_{tr}$ is the average amount of kinetic energy transferred to electrons of the medium at each interaction.

Kerma can be divided in to collision and radiative components.[15] The collision kerma, K_c is defined as

$$K_c = K(1-g) = \int_E \Psi_E \left(\frac{\mu_{en}}{\rho}\right)_E dE, \tag{1.11}$$

and the radiative terma, K_r, as

$$K_r = gK = \int_E \Psi_E \left(\frac{\mu_{tr} - \mu_{en}}{\rho}\right)_E dE. \tag{1.12}$$

1.2.8 Terma

The *total energy released per unit mass*, or terma, was introduced by Ahnesjö *et al.*[16] for use in the superposition/convolution method of dose calculation (refer section 2.2.5). The terma, $T(\mathbf{r})$, is the total energy removed from the primary (incident) beam per unit pathlength at point $\mathbf{r}$, and can be calculated from the divergence of the vectorial energy fluence, $\Psi(\mathbf{r})$ of primary photons,

$$T(\mathbf{r}) = \frac{-1}{\rho(\mathbf{r})} \nabla . \Psi(\mathbf{r}), \tag{1.13}$$

where $\rho(\mathbf{r})$ is the density distribution of the medium. Only the incident photons are used in the terma calculation, as the scattered photons are accounted for in the scatter convolution kernel (refer section 2.2.5).

For a spectrum of primary photons, the terma becomes[16]

$$T(\mathbf{r}) = \int_E \left(\frac{\mu}{\rho}\right)_{E,\mathbf{r}} \Psi_E(\mathbf{r}) dE, \tag{1.14}$$

where $(\mu/\rho)_{E,\mathbf{r}}$ is the mass attenuation coefficient of the primary photons of energy E at $\mathbf{r}$, and $\Psi_E(\mathbf{r})$ is the primary photon fluence differential in energy and position. From the terma distribution function, the resultant absorbed dose can be obtained if the energy transport of the secondary particles around each interaction point is known.

Kerma and terma can be quickly and exactly calculated if the initial spectra and patient density are known. The difficulty is in accounting for the transfer of energy from the secondary electrons to the absorbing medium, especially if inhomogeneities are present.

1.3 Electron interactions I. Energy losses

1.3.1 Introduction

Electrons at medical energies lose energy principally in Coulomb interactions with bound electrons in the absorbing medium. Because the relativistically corrected mass of the incoming electron is of a similar order as the mass of the bound electron (a 3 MeV electron has a mass seven times the electron rest mass[17]), the interactions are inelastic resulting in energy loss. These interactions are termed *collisional* energy losses. The electron creates a trail of ionisations and excitations along its path, and hence energy is deposited in the medium. Electrons also lose energy as they are decelerated in the field of a nucleus, thus causing a photon to be emitted. This process is called *radiative* energy loss, and the radiation called bremsstrahlung.

Because of the uncertainty involved in the energy loss events, electrons of the same energy, and incident at the same point will travel different distances along different paths. This spread of path lengths and energy loss is termed *energy-loss straggling.*

1.3.2 Ionisation and excitation energy losses

A fast electron loses most of its kinetic energy by ionisations and excitations of atoms in the absorbing medium. Ionisation occurs when the incoming electron (or positron) passes close enough to an orbital electron to eject the orbital electron from the atom. If the fast moving electron passes an atom at a larger distance, energy transfer can still occur by way of an orbital electron being elevated to a higher energy state, thereby exciting the atom.

1.3.3 δ-ray production

δ-rays (also termed knock-on electrons) are produced when the incoming charged particle interacts sufficiently violently with a bound electron that the ejected electron forms a track of its own, as shown in figure 1.5. Both the ejected electron, and the incident charged particle can undergo further interactions and deposit energy. If the incoming charged particle is an electron, the δ-ray event is called Møller scattering,[18] and if the incoming particle is a positron the event is termed Bhahba scattering.[19][3]

The maximum energy loss in a Møller interaction is half of the kinetic energy of the incoming electron, as the two ejected electrons are indistinguishable. The highest energy particle is defined as the primary electron. The maximum energy loss in Bhahba scattering is the total kinetic energy of the positron, as the particles are distinguishable.

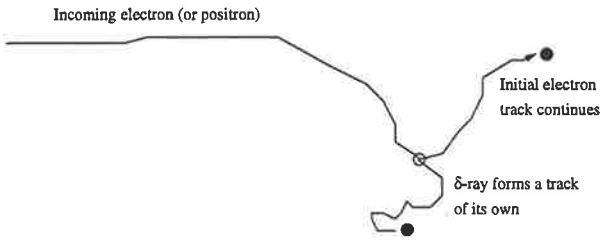

Figure 1.5: **Schematic representation of δ-ray production.**

1.3.4 Bremsstrahlung production

A fast electron passing very close to the nucleus of an atom will feel the Coulomb attraction of the nucleus and its path will be slightly altered towards the nucleus. To conserve momentum, a bremsstrahlung photon is emitted (as shown in figure 1.6) and

[3] An excellent overview of the physics of Møller and Bhahba scattering is outlined in the EGS4 manual[8].

the energy of the electron is reduced. Interactions of a positron and a nucleus can also produce bremsstrahlung, as well as electron-electron and positron-electron interactions.

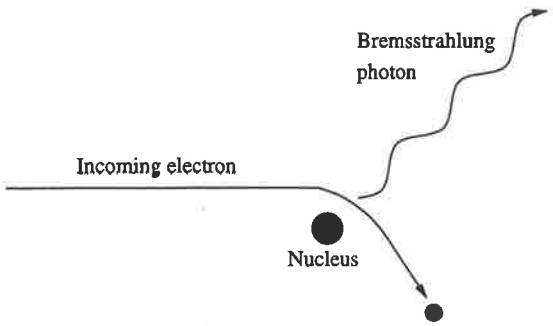

Figure 1.6: **Schematic representation of bremsstrahlung production.**

1.3.5 Collisional stopping power

The amount of kinetic energy lost by electrons per unit pathlength due to ionisations and excitations is called the collisional stopping power, S_{col}. Often it is convenient to define the mass collision stopping power, $(S/\rho)_{col}$.

Berger and Seltzer's[20] expression for the mass collision stopping power is

$$\left(\frac{S}{\rho}\right)_{col} = \frac{2\pi r_e^2 m_e c^2 N_A Z}{\beta^2 M_A}\left[\ln\left(\frac{\tau^2(\tau+2)}{2(I/m_e c^2)^2}\right) + F(\tau) - \delta\right], \tag{1.15}$$

where N_A, Z, M_A, β, τ, I and δ are Avogadro's number, the atomic number (effective for the mixture/compound), the molar mass of substance A, velocity of the electron relative to the velocity of light in a vacuum, ratio of the kinetic energy of the electron to the rest energy, mean excitation energy and the density effect correction. $F(\tau)$ is given by

$$F(\tau) = 1 - \beta^2 + [\tau^2/8 - (2\tau+1)\ln 2]/(\tau+1)^2. \tag{1.16}$$

δ, the density effect correction causes (i) a decrease of stopping power with density, and (ii) a decrease in stopping power with energy.[13] Phenomena (i) is due to the passage of the charged particle which results in polarisation of the medium. In a dense media, where the atoms are packed close together, the field of distant atoms are 'screened' by the polarisation of near atoms. In a less dense media, the charged particle will interact more strongly with distant atoms, as shown in figure 1.7. The density effect increases with energy, because as the velocity of the particle is increased, the electric field is stronger at the sides of the moving charge due to the Lorentz contraction of the Coulomb field, as shown in figure 1.8.[21] Hence the interactions of more distant atoms becomes important, and it is these interactions that are reduced in intensity by the polarisation of intervening atoms.

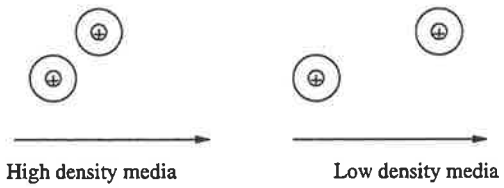

Figure 1.7: **Schematic representation of the reduction in stopping power in dense media. In the high density media the effect of the more distant atom is reduced by the induced polarisation of the field of the intervening atom, thus partially screening the distant atom from interacting with the moving electron. In the less dense media, where the atoms are further apart, this screening occurs less often.**

The density effect causes the ratio of the mass stopping power in water to that in air to be significantly energy dependent above 0.5 MeV[22] since the stopping power of water is affected more by the density effect than that of air. This effect occurs despite water and air having a very similar atomic number. Because of the density effect, the water/air mass stopping power ratio needs to be accounted for when using ion chambers for radiation dosimetry in water.

The terms in equation 1.15 that account for the composition of the absorbing medium are Z/M_A and I. As Z/M_A is approximately constant ($\approx 1/2$) for most elements, the

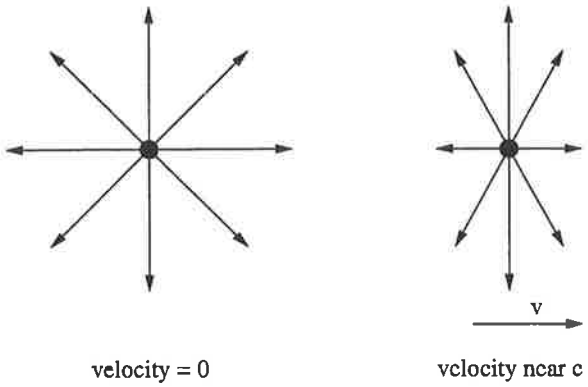

Figure 1.8: **Schematic representation of the effect of the Lorentz contraction on the electric field of a fast moving charged particle.**

mass collision stopping power is fairly independent of absorbing medium. However, water tends to have a higher mass collision stopping power than other absorbing media, as it contains a large amount of hydrogen (Z/M_A for hydrogen is 1).

In dealing with radiation interactions it is sometimes convenient to measure thickness in terms of the material dependent radiation length, X_0,[23] which is defined by

$$\frac{1}{X_0} = 4\alpha\frac{N_A}{A}Z^2 r_e^2 \ln(183Z^{-1/3}). \tag{1.17}$$

1.3.6 Restricted collisional stopping power

In some situations, such as dosimetry and radiobiological modelling, only those energy losses which lead to secondary electrons with energies below a cut-off energy, Δ, are of interest. Hence, the restricted collision stopping power, L_Δ, includes only these energy losses. L_Δ is fractionally smaller than S_{col}, and can be obtained from equation 1.15 by substituting $F(\tau, \Delta)$ for $F(\tau)$,[20]

$$F(\tau, \Delta) = -1 - \beta^2 + \ln\left[4\Delta(\tau - \Delta)\tau^{-2}\right] + \tau/(\tau - \Delta)$$

$$+\left[\Delta^2/2+(2\tau+1)\ln(1-\Delta/\tau)\right](\tau+1)^{-2}, \tag{1.18}$$

where Δ is expressed as fraction of the rest energy of the electron.

1.3.7 Radiative stopping power

Radiative electron interactions (bremsstrahlung production) are frequently large energy loss events, and can significantly contribute to the total stopping power, especially for high energy electrons in high atomic number materials. The mean energy loss of electrons due to radiative collisions cannot be given a general analytical form covering all energies and materials.[24] However, a general form of the mass radiative stopping power for high energies (assuming complete screening: $\tau \gg 1/\alpha Z^{1/3}$) is[25]

$$\left(\frac{S}{\rho}\right)_{rad} = \frac{4r_e^2\alpha}{\beta^2}N_A\frac{Z(Z+1)}{M_A}(\tau+1)m_ec^2\ln(183Z^{-1/3}+1/18), \tag{1.19}$$

where α is the fine structure constant. An approximation for the ratio of radiative to collisional losses is

$$\frac{S_{rad}}{S_{col}} = \frac{EZ}{800}. \tag{1.20}$$

The total stopping power, S, is found by summing S_{col} and S_{rad},

$$S = S_{col} + S_{rad}. \tag{1.21}$$

1.3.8 Restricted radiative stopping power

In some dose calculation algorithms such as EGS4[8] and SMC (refer chapter 5) it is necessary to incorporate a restricted radiative stopping power, $L_{\Delta',rad}$, the stopping power

due to photons produced with energies below Δ' due to bremsstrahlung interactions of the incoming electron with the nuclei and electrons of the absorbing medium.

$L_{\Delta',rad}$ can be calculated by replacing the upper limits of the integrals of equation 9.1 in ICRU 37[26] with Δ', and using the cross sectional data from Berger and Seltzer[27]), ie

$$\frac{S_{rad}(E)}{\rho} = \frac{1}{uA}\left[\int_0^E k\frac{d\sigma_n}{dk}dk + Z\int_0^{E'} k\frac{d\sigma_e}{dk}dk\right] \tag{1.22}$$

becomes

$$\frac{L_{\Delta',rad}(E)}{\rho} = \frac{1}{uA}\left[\int_0^{\Delta'} k\frac{d\sigma_n}{dk}dk + Z\int_0^{\Delta'} k\frac{d\sigma_e}{dk}dk\right], \tag{1.23}$$

where E is the kinetic energy of the incident particle, E' is the largest possible energy of photons emitted in electron-electron bremsstrahlung events, u and A are the atomic mass unit and atomic weight respectively, k is the energy of the photon emitted in the bremsstrahlung process, and $d\sigma_n/dk$ and $d\sigma_e/dk$ are the differential cross section for electron-nucleus and electron-electron bremsstrahlung respectively.

1.4 Electrons interactions II. Scattering

1.4.1 Introduction

Electron scattering significantly affects the absorbed dose distribution in a medium, especially where inhomogeneities are present.[28, 29] Angular deflections cause a lateral displacement of the incident electrons, thereby broadening the dose distribution and decreasing the depth of penetration. If the beam passes through adjacent regions of different density, the difference in scattering will cause a perturbation in the dose distribution.[30] A consequence of scattering is the build-up region in an electron depth dose curve (refer section 1.8.2), where increased obliquity of the electrons in the beam

causes an increase in fluence with depth, and a subsequent increase in the rate of energy deposition.

Electron scattering and energy losses are not independent events. Large energy loss events such as bremsstrahlung or δ-ray production will result in a larger scattering angle than a low energy interaction. However, on a macroscopic scale, scattering and energy losses can be examined independently.

Therapeutic electron beams are scattered predominantly by elastic collisions with atomic nuclei.[28] The scattering is elastic because the nucleus has a mass to the order of 10^2 times the relativistic mass of the incoming electron, so the energy transfer to the nucleus is negligible.

Elastic scattering can be divided into single scattering, plural scattering or multiple scattering. If the thickness, l, of the scattering medium is very small, there will be practically only *single scattering*: most of the electrons are scattered by only one nucleus. This occurs when $l \ll 1/\sigma_s n$, where σ_s is the energy dependent scattering cross section and n the number of scattering atoms per unit volume. Larger thickness values, where $l \approx 1/\sigma_s n$, results in *plural scattering*: there is a higher probability that the electrons are scattered by several nuclei. When the thickness becomes so large that the mean number of processes is greater than 20-30, the term *multiple scattering* is used.

1.4.2 Single scattering

For non-relativistic energies, and neglecting the shielding effect of the orbital electrons on the nuclear charge, the differential cross-section per atom for scattering from a pure Coulomb field through an angle between θ and $\theta + d\theta$ into a solid angle $2\pi \sin\theta d\theta$ is

given by the Rutherford formula[28]

$$d\sigma_s(\theta) = \frac{\pi e^4 Z^2}{2m_e^2 \nu^4} \frac{\sin\theta d\theta}{\sin^4(\theta/2)}, \tag{1.24}$$

where e is the electron charge, and ν is the velocity of the electron.

The neglect of the shielding is valid at higher energies.[28] At relativistic energies the mass of the electron is significantly higher than the rest mass, hence the relativistic mass needs to be accounted for by including a β $(= \nu/c)$ term. Thus the Rutherford cross-section becomes

$$d\sigma_s(\theta) = \frac{\pi e^4 Z^2 (1-\beta^2)}{2m_e^2 \nu^4} \frac{\sin\theta d\theta}{\sin^4(\theta/2)}. \tag{1.25}$$

A more accurate cross-section invokes the Dirac equation to account for the spin of the electron. This expression takes the form of an infinite series. This series was simplified by McKinley and Feshback[31] who expanded the cross-section obtained in powers of α' $(= Z/137)$ up to terms of the order of α'^3. They have given the ratio, r, of the actual cross-section to the Rutherford value as

$$r = \left(1-\beta^2\right) \sin^2\left(\frac{\theta}{2}\right) + \pi\alpha'\beta \sin\left(\frac{\theta}{2}\right)\left[1 - \sin\left(\frac{\theta}{2}\right)\right]. \tag{1.26}$$

This ratio is correct for low atomic number elements $(Z < 27)$ such as those considered in practical dosimetry.

The cross-section for scattering in the field of an electron, instead of a nuclear charge, is identical, except for a factor of Z. This difference occurs because the scattering cross-section per unit area is proportional to the number of targets multiplied by the square of the charge (refer equation 1.24). Hence for an atom with Z electrons, electron-

nuclear scattering is proportional to $1.Z^2 = Z^2$, whereas electron-electron scattering is proportional to $Z.1^2 = Z$. Though electron-electron collisions are the main way by which an electron loses energy (refer section 1.3), their contribution to scattering is small. To account for both electron-electron and electron-nucleus scattering the Z^2 term in 1.25 is replaced by $Z(Z+1)$. For high Z elements, $Z(Z+1)$ tends towards Z^2, so for these elements electron-electron scattering can be ignored.

1.4.3 Multiple scattering

Grouping together a number of ionisation and excitation events is called multiple scattering. Because electrons lose most of their energy this way, multiple scattering is an important process, though is difficult to calculate accurately. Three separate multiple scattering theories have been proposed by Goudsmit and Saunderson,[32] Molière[33, 34] and Eyges[10] (based on the solution to Fermi's equation[35] where the energy loss is significant). The simplest of the three theories, Fermi-Eyges, only accounts for small angle multiple scattering, ignoring large angle scattering. This theory is used in the pencil beam dose calculation method (refer section 2.3.3).

The Fermi-Eyges (FE) equation describing multiple Coulomb scattering is[36]

$$\frac{\partial P(\theta_x, x, z)}{\partial z} = -\theta_x \frac{\partial P}{\partial x} + \frac{T_s(z)}{4} \frac{\partial^2 P}{\partial \theta_x^2}, \tag{1.27}$$

where $P(\theta_x, x, z)$ is the probability distribution function of the scattered particles travelling initially in the z-direction, z is the depth in the scattering medium, x and θ_x are the lateral position and angle of travel projected onto the x-z plane respectively, and $T_s(z)$ is the linear scattering power.

The solution to Eq. 1.27, for a particle travelling initially in the z-direction is[37]

$$P(x,\theta_x;z) = \frac{1}{\pi\sqrt{A_0A_2 - A_1^2}} e^{-(A_0x^2 - 2A_1x\theta_x + A_2\theta_x^2)/(A_0A_2 - A_1{}^2)}. \tag{1.28}$$

A_i (i = 0,1,2), the scattering moments of the pencil beam,[36] are

$$A_i(z) = \frac{1}{2}\int_0^z T_s(z') \cdot (z - z')^i dz'. \tag{1.29}$$

The resulting planar fluence, $P_L(x;z)$, gives the probability that an electron will have a lateral displacement x at depth z irrespective of θ_x). P_L is found by integrating P over all θ_x:

$$P_L(x;z) = \frac{1}{\sqrt{2\pi}\sigma_x} e^{\left(\frac{-x^2}{2\sigma_x^2}\right)}. \tag{1.30}$$

The lateral distribution is thus Gaussian with mean $x = 0$, standard deviation σ_x and amplitude $1/\sqrt{2\pi}\sigma_x$. σ_x can also be calculated directly by

$$\sigma_x = \sqrt{\frac{1}{2}\int_0^z T_s(z').(z - z')^2 dz'}. \tag{1.31}$$

FE theory can also be used to transport electrons through layers of different material if the linear angular scattering power, $d\bar{\theta}^2/dz$, for each material is known. The parameters describing the spatial angular distribution are obtained from the scattering moments A_0, A_1 and A_2. These values can be calculated recursively, using the value at the end of the previous layer and the scattering power of the current layer:[38]

$$A_0(z_i) = A_0(z_{i-1}) + \frac{\Delta z}{2}\frac{d\bar{\theta}^2}{dz} \tag{1.32}$$

$$A_1(z_i) = A_1(z_{i-1}) + \Delta z A_0(z_{i-1}) + \frac{(\Delta z)^2}{4}\frac{d\overline{\theta}^2}{dz} \tag{1.33}$$

$$A_2(z_i) = A_2(z_{i-1}) + 2\Delta z A_1(z_{i-1}) + (\Delta z)^2 A_0(z_{i-1}) + \frac{(\Delta z)^3}{6}\frac{d\overline{\theta}^2}{dz}. \tag{1.34}$$

From the scattering moments, the following parameters are obtained:

i) the x-component of the lateral standard deviation at depth z

$$\sigma_x = \sqrt{A_2}, \tag{1.35}$$

ii) the mean x-component of electron direction at depth z and lateral position x

$$\overline{\theta}_x = \frac{A_1}{A_2}x, \tag{1.36}$$

iii) and the x-component of the angular standard deviation about the mean angle at (x, z)

$$\sigma_{\theta_x} = \sqrt{A_0 - A_1^2/A_2}. \tag{1.37}$$

Scattering power

The mean square angle of scattering increases linearly with the thickness of the absorbing medium[23] because the scattering events in different layers are statistically independent, and their respective mean square scattering angles thus add up linearly. A mass scattering power, T_s/ρ, can be defined as the increase in the mean square scattering angle, $d\overline{\theta}^2$, per unit mass thickness, ρdz in terms of the mass traversed per unit cross sectional area.[3, 39] ICRU 35[25] gives the expression for mass scattering power as

$$\frac{T_s}{\rho} = \frac{d\overline{\theta}^2}{\rho dz}\pi\left(\frac{2r_e Z}{(\tau+1)\beta^2}\right)^2 \frac{N_A}{M_A}\left[\ln\left(1+\left(\frac{\theta_m}{\theta_\mu}\right)^2\right) - 1 + \left(1+\left(\frac{\theta_m}{\theta_\mu}\right)^2\right)^{-1}\right], \tag{1.38}$$

where θ_m is the cut-off angle due to the finite size of the nucleus, and θ_μ the screening angle. θ_m is given by the ratio of the reduced de Broglie wavelength of the electron to the nuclear radius and is

$$\theta_m = \frac{2A^{-1/3}}{\alpha\beta(\tau+1)}. \tag{1.39}$$

For $\theta_m > 1$, θ_m should be set to 1.[23] The screening angle, θ_μ, is due to the screening of the nucleus by the orbital electrons. This angle is given by the ratio of the reduced de Broglie wavelength of the electron to the atomic radius and is

$$\theta_\mu = 1.13\frac{\alpha Z^{1/3}}{\beta(\tau+1)}. \tag{1.40}$$

1.5 Absorbed dose

The absorbed dose, D, is defined as the quotient of $d\overline{E}_{en}$, the mean energy imparted by ionising radiation to matter of mass dm,[14]

$$D = \frac{d\overline{E}_{en}}{dm}. \tag{1.41}$$

In the case of a photon beam, this energy is imparted to electrons by photons, and the secondary electrons set in motion deposit energy to the medium. Attix[15] showed that under charged particle equilibrium conditions, absorbed dose equals collision kerma, $D = K_c$. However, in general, as K_c is defined at the photon interaction site, and because of the finite range of secondary electrons (up to several cm), most of the energy is deposited away from the photon interaction site. After the buildup region, absolute dose is greater than collision kerma because of the combined effect of the attenuation of the photon beam (refer section 1.7.2) and the predominantly forward directed motion of the secondary electrons.

The unit of dose is the gray (Gy), which equals 1 Joule of absorbed energy per kilogram of matter.

1.5.1 Primary and scatter dose

The total dose for a photon beam can be partitioned into primary, D_p, and scatter, D_s, components. The primary dose is the dose deposited by electrons set in motion by the interaction of incident photons. The scatter dose is that deposited by electrons set in motion by scattered photons, annihilation photons and bremsstrahlung photons. The separation of primary and scatter dose is useful for calculation of dose in inhomogeneous media.

The concept of primary and scatter dose has less relevance for electron beams, but still has validity. The primary dose can be considered to be that due to incident electrons, and the scatter dose the sum of the dose contribution from bremsstrahlung contamination photons (refer section 1.8.1), and photons produced in the absorbing medium.

1.5.2 Measurement of absorbed dose

Because of the strong dependence of the tumour control probability and normal tissue complication probability curves with dose,[40] it is necessary to accurately determine the quantity of dose delivered in a radiotherapy procedure. Absorbed dose can be measured directly by calorimetry,[41] which is based on the principle that the energy absorbed in a medium from radiation appears ultimately as heat energy and a small chemical change. From the temperature change the energy deposited can be calculated. Though calorimetry is easy to apply in principle, it is difficult to perform due to the small temperature change, and is not used in radiotherapy centres. To measure dose from

medical linear accelerators, the most common approach is to measure exposure, X. Exposure us defined as[11]

$$X = \frac{dQ}{dm}, \tag{1.42}$$

where dQ is the absolute value of the total charge of the ions of one sign produced in air when all of the electrons liberated by photons in a volume element of air having a mass dm are completely stopped in air. Exposure is usually measured using an ion chamber. The ion chamber electrically captures the liberated ions, and produces a current proportional to the amount of liberated ions. This measured experimental value is converted to dose by multiplying the total charge liberated in air by the average energy required to produce an ion pair, W_{air}/e,

$$D_{air} = X\frac{W_{air}}{e}. \tag{1.43}$$

The dose to the medium in which the ion chamber is inserted, D_{med} is given by

$$D_{med} = X\frac{W_{air}}{e}\frac{(\mu_{en}/\rho)_{med}}{(\mu_{en}/\rho)_{air}}\frac{\Psi_{med}}{\Psi_{air}}. \tag{1.44}$$

(For a derivation of equation 1.44 see Khan.[12])

Other commonly used techniques for measuring dose involve using diodes, radiographic film and diamond detectors.

1.6 The main components of a linear accelerator

Medical linear accelerators (linacs) are used to produce X-ray and electron beams which are used clinically in the radiotherapy treatment of cancer. A modern linear accelerator is composed of a modulator, magnetron or klystron, electron gun, accelerating waveguide and a treatment head, as shown in figure 1.9. There are many types of linac design, but all have a similar structure.

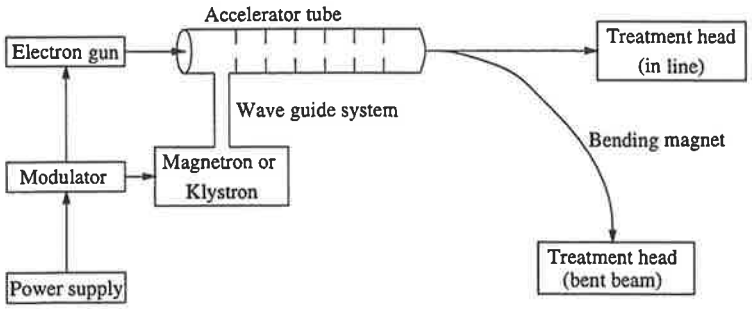

Figure 1.9: **A block diagram of a therapeutic linear accelerator. Adapted from Khan.[12]**

The modulator converts the DC power supply into high voltage pulses of a few microseconds in duration using a pulse forming network and hydrogen thyratron switch. These pulses are simultaneously delivered to the electron gun, and the klystron or magnetron. Magnetrons and klystrons are both devices for producing microwaves. Klystrons are more expensive, but have a longer life span, and are capable of delivering higher power levels.

In a magnetron, electrons are generated from the cathode by thermionic emission into an evacuated chamber. A combination of a static magnetic field and a pulsed DC electric field cause the electrons to move in complex spirals towards resonant cavities, radiating energy in the form of microwaves.

A klystron is a microwave amplifier rather than a microwave generator, and therefore needs a low power microwave oscillator. Electrons produced by a cathode are energised by the low power microwaves. These microwaves set up an alternating electric field across the cavity, bunching the electrons by velocity modulation. The electron bunches accelerate down a drift tube until they reach a second cavity, where by a reverse process, the amplified high power waves are tapped.

The microwaves from the magnetron or klystron are led to the accelerator structure via

a waveguide. The electron gun injects electrons of about 50 keV into the accelerator tube. These electrons interact with the electromagnetic field of the microwaves, and are accelerated through each cavity of the tube by the sinusoidal electric field to near light speed (a 3 MeV electron has a velocity of 0.99c), by either a travelling or standing wave mechanism.[42]

Depending on the linac design, the electrons emerging from the accelerating waveguide are either focussed directly onto the beam production material (where the accelerating waveguide is 'in-line' in the treatment head), or are magnetically bent 90° or 270° before focussing occurs. To produce X-ray beams, the beam production material is a high atomic number material target (typically tungsten); to produce electron beams thin high atomic number scattering foils are used. The particles in the radiation beam are shaped into a useful field by collimators in the treatment head, and in the case of electrons with an applicator placed ≈5 cm from the patient. The proximity of the applicator to the patient is needed to confine the electrons which scatter in the air column between the treatment head and patient.

1.7 Clinical photon beams

1.7.1 Introduction

For photon beam generation, electrons from the waveguide of a linear accelerator (refer section 1.6) are focussed onto a thick target, producing a thick target bremsstrahlung spectrum.[11] To increase the photon yield a high atomic number material is used to maximise the ratio of radiative energy losses to collisional energy losses (refer equations 1.19 and 1.15), and therefore maximise the radiation yield. Below the target is a flattening filter, which is shaped to obtain a flat dose profile across the beam, in order to

deliver a uniform dose to the tumour. To achieve this flatness, the target is thicker in the centre to attenuate some of the normally incident photons. The increased thickness in the centre leads to a 'harder' (higher average energy) beam at the central axis, with a softer average spectrum with off axis distance (eg. for a 10 MV beam Mohan *et al.*[43] found the average photon energy between 0 and 2 cm off-axis was 2.97 MeV, which decreased to 2.52 MeV between 5 and 10 cm off-axis).

The photon beam is shaped using collimators in the treatment head, and often external shielding blocks to give a clinically useful beam. Photon beams are generally used to treat deep seated tumours.

There are a wide range of electron accelerating energies used to produce photon beams. Low energy beams have a higher surface dose, shallower depth of maximum and steeper fall-off curves (refer section 1.7.2). The lower energy also means lower energy secondary electrons produced which have a shorter range, resulting in tighter penumbra (refer section 1.7.3), and accurate dose calculation is easier. Higher energy beams increase the likelihood of pair production which will result in increased photon interactions in bone.

In choosing the 'best' accelerating energy, both the physical characteristics outlined above, as well as the size and depth of the tumour and surrounding critical structures need to be taken into account.

1.7.2 Photon beam depth dose curves

The main features of a photon beam depth dose curve as shown in figure 1.10 (where the photon beam is incident on a surface located at depth 0 cm and the absorbed dose is normalised to 100% at maximum) are the initial increase in dose, the depth of maximum dose, d_{max}, and the exponential fall-off. The initial increase, or build-up is due to the finite, predominantly forward directed range of electrons set in motion by the incident

photons. As more photons interact, the electron fluence increases, and hence the build-up of dose. Electrons emitted from the target, and those produced in the air column between the treatment head and the patient also increase dose in the build-up region (termed electron contamination).

The fall-off in dose in the depth dose curve is due to the logarithmic reduction in planar photon fluence as the photons traverse the absorbing medium. As the attenuation coefficient decreases with increasing energy, the low energy photons in the spectrum are preferentially attenuated. This attenuation results in a higher average energy spectrum with depth, called beam hardening. Hoban *et al.*[44] found that a 10 MV spectrum of average incident energy 3.0 MeV was hardened to an average of 3.7 MeV at 20 cm depth in water.

The energy of the secondary electrons produced by the photon beam increases with energy, therefore d_{max} increases with energy (eg. for 6 and 18 MV beams d_{max} is 1.5 and 3.3 cm respectively). The attenuation coefficient is less sensitive to energy than the secondary electron range, and hence the difference in fall-off between different energy beams is less pronounced than the change in d_{max}. The beam quality can be determined by a ratio of the dose at 20 cm depth to the dose at 10 cm depth, ie. D_{10}^{20}. For 6 and 18 MV beams D_{10}^{20} is 0.56 and 0.66 respectively.

1.7.3 Photon beam dose profile curves

A dose profile curve is the dose measured along a line which is perpendicular to the incident beam direction. The centre of the dose profile curve of figure 1.11 is fairly uniform because of the design of the target. The 'shoulders' of the profile are rounded because of the finite lateral range of the electrons set in motion by the photon beam. The electrons scattered out of the beam are not replaced by the electrons scattered in from outside the beam, and hence lateral electron disequilibrium occurs. Another contributing

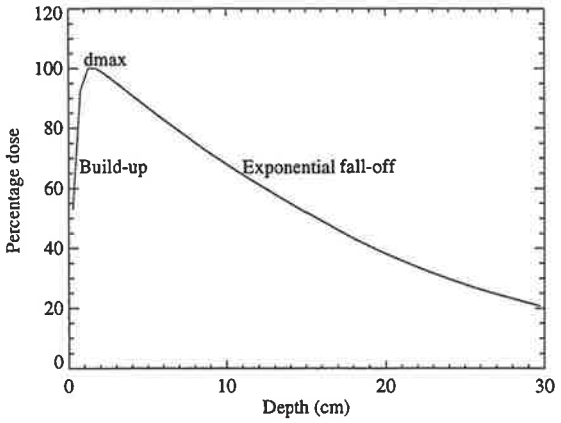

Figure 1.10: **A 10×10 cm^2, 6 MV photon beam depth dose curve showing the build-up region, the depth of maximum dose, d_{max}, and the exponential fall-off.**

factor to the roundness of the profiles is the geometric penumbra due to the finite source size. Because of the range of the electrons inside the target, and the finite width of the initial electron beam above the target, the photon source is not a point. Treuer *et al.*[43] experimentally measured the source density function for a 15 MV photon beam to have a FWHM of 2.5 mm.

The dose at the edges of the profiles does not fall away to zero because of the contribution of photons scattered out of the useful beam by Compton scattering and bremsstrahlung production, and from photons scattered from the treatment head.

1.7.4 Photon beam isodose curves

The isodose distribution gives a 2-dimensional picture of how dose is distributed through the irradiated medium. The increase in beam size (divergence) due to the finite source-surface distance (SSD) can be seen in figure 1.12.

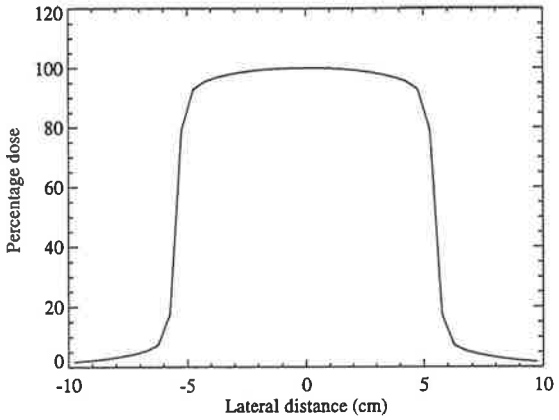

Figure 1.11: **A 10×10 cm^2, 6 MV photon beam dose profile curve, at 10 cm depth, showing the flat dose region in the field, and the penumbra.**

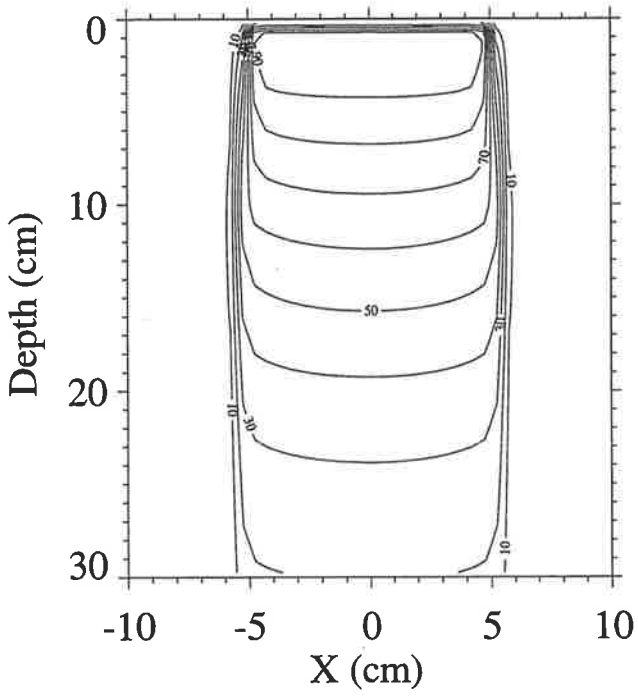

Figure 1.12: **A 10×10 cm^2, 6 MV photon beam isodose curve.**

1.8 Clinical electron beams

1.8.1 Introduction

For clinical electron beam generation from a linac, electrons from the waveguide are focussed onto a thin high atomic number scattering foil (or foils) to diverge electrons to obtain a clinically useful broad beam. A high atomic number material is used to maximise electron scattering, whilst minimising energy degradation (ie. maximise T_s/S from equations 1.38 and 1.21). However, the high atomic number scattering foils also produces a high radiation yield (refer equation 1.19), and hence clinical electron beams have a photon contamination component. Ebert[45] has determined that there are more photons than electrons in an electron beam. However, because the photons are of lower average energy, and deposit this energy over a larger volume, the maximum contribution is approximately 4% of the maximum dose for a 15 MeV electron beam.[46]

To produce a clinical beam, generally two scattering foils separated by an air gap (a dual foil system) are used instead of one foil. To produce a beam of the same width, the sum of the thickness of the dual foils is considerably less than the thickness of a single foil. Therefore, there is less energy degradation and less photon contamination in a dual foil system. Electron beams are generally used to treat superficial tumours, or tumours of the skin.

1.8.2 Electron beam depth dose curves

A typical electron depth dose curve (refer figure 1.13) has a region of build-up to the depth of maximum dose, a steep fall-off region, and a bremsstrahlung tail. An electron beam depth dose curve is characterised by the depth of maximum dose, d_{max}, the mean

range of the electrons, R_{50} (the point where the dose falls to 50% of the value of the dose at d_{max}), and the practical range of the electrons, R_p (where the extrapolation from the linear part of the fall-off curve and the bremsstrahlung tail meet). The therapeutic range, R_{80} is also sometimes used to indicate the depth to which the beam is clinically useful.

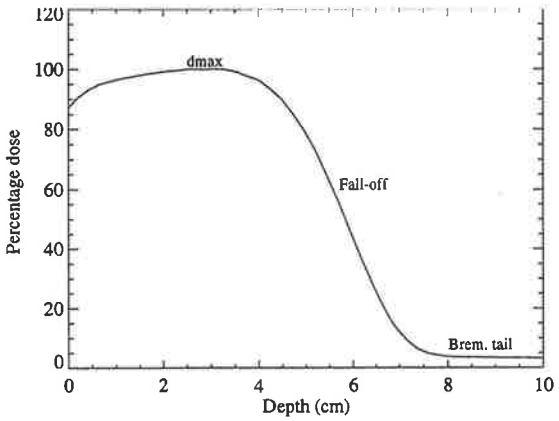

Figure 1.13: **A 10×10 cm^2, 15 MeV electron beam depth dose curve showing the depth of maximum dose, the fall-off region and the bremsstrahlung tail.**

The build-up is due to the rise in fluence due to the increasing obliquity of electrons with depth due to scattering in the absorbing material. The ratio of surface dose to dose at d_{max} increases with energy because the scattering power of a medium decreases with energy to the power of approximately 1.8,[47] while the stopping power is approximately independent of energy (above ≈0.3 MeV). Note that if the scattering power was proportional to $1/E^1$, then the ratio of surface dose to d_{max} would be the same for all energies, as the increase in obliquity would be linear with energy.

The fall-off in dose occurs because some of the electrons have run out of energy and stopped. The fall-off is not sudden because of energy-loss straggling.

The bremsstrahlung tail is due to dose deposited by photons interacting in the absorbing medium. These photons are produced mostly in the scattering foils and other treatment

head components, but also in the irradiated medium itself.

1.8.3 Electron dose profile curves

The electron beam dose distribution can also be presented as a dose profile. A profile is flat at the central axis (beam axis) for most field sizes, and then falls away at the field edge. The region of a profile where the dose falls off is called the penumbra.

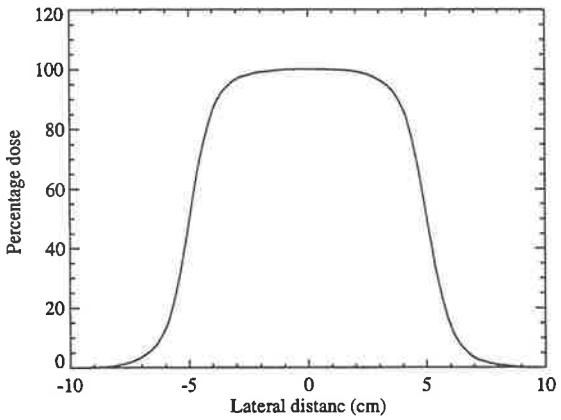

Figure 1.14: **A 10×10 cm^2, 15 MeV electron beam dose profile curve at 4 cm depth.**

An electron beam dose profile curve is similar in shape to a photon beam dose profile curve because of the similar physical factors governing the penumbra, however the penumbral width increases rapidly with depth for an electron beam.

1.8.4 Electron isodose curves

Electron beam dose distributions can be represented in 2 dimensions by an isodose curve, as shown in figure 1.15. The figure shows how the penumbra width increases with depth

as the electrons are deflected laterally.

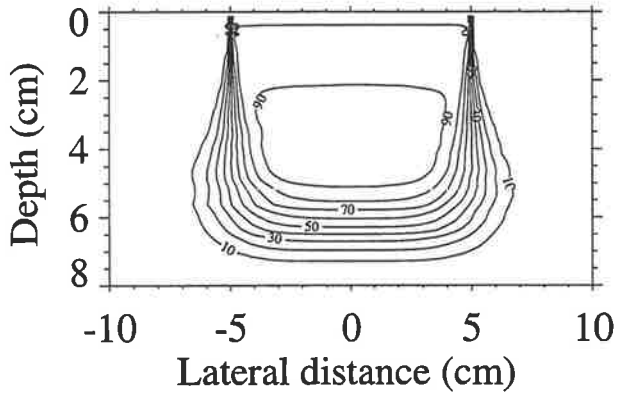

Figure 1.15: **A 10×10 cm^2, 15 MeV electron beam isodose curve.**

1.9 Electron density

The electron density, ρ_e, is the number of electrons in a medium per unit volume. The electron density is important for dose calculation since in the dominant X-ray interaction process (Compton scattering) the photon interacts with electrons in the absorbing medium. Hence the probability of interaction is proportional to the electron density. The electron density ρ_e is related to the mass density by the equation

$$\rho_e = N_A \rho \frac{Z}{A}. \tag{1.45}$$

Electron density is usually given as a fraction of the electron density of water, ρ_{ew}. The electron density relative to water ρ_e^w is

$$\rho_e^w = 1.80 \rho \frac{Z}{A}. \tag{1.46}$$

The relative electron density of a patient can be determined from a computed tomography (CT) examination. A CT exam involves arcing a diagnostic energy X-ray source around a patient. The photons passing through the patient give a detector response from which an image of CT numbers (Hounsfield numbers) are formed by back-projection of the transmitted X-rays. The Hounsfield numbers (H) are given by

$$H = \frac{\mu_{tissue} - \mu_{water}}{\mu_{water}} \times 1000. \tag{1.47}$$

The electron density relative to water is derived from Hounsfield numbers by[48]

$$\rho_e^w = R_\gamma \frac{H}{1000} + 1, \tag{1.48}$$

where R_γ is the ratio of CT to electron density number. R_γ for soft tissues is 1.0, however R_γ is reduced for bone as the increased attenuation of the CT scanner photon beam in bone compared to water because of the dominance of the photoelectric effect at CT energies.

1.10 Radiological depth

Radiological depth is the depth d' in water, which attenuates a photon beam as much as the physical depth in a heterogeneous medium, d. Radiological depth is used in the calculation of kerma and terma, and is calculated by a raytrace along a line $\mathbf{r}$ from the surface (or another point of interest) to the point d,

$$d' = \int_{surface}^{d} \rho_e^w(\mathbf{r}) d\mathbf{r}. \tag{1.49}$$

Chapter 2

Current Dose Calculation Methods

2.1 Introduction

In radiotherapy procedures it is advantageous to achieve a high uniform dose to the tumour volume, whilst minimising dose to healthy tissue. Such a treatment is achieved by varying the particle type, number of fields, field size, beam energy and position, and the inclusion of external beam shaping devices such as blocks, wedges and cut-outs. To determine the dose to the patient from each field (and hence the summed dose for treatment), an accurate dose calculation method is needed.

The benefit of accurate dose calculation in radiotherapy is the availability of better quality information with which to prescribe treatments, and confidence when radiobiological models and/or optimisation procedures are applied in the planning phase. The complexity of electron transport and energy deposition in radiotherapy (as outlined in chapter 1) makes an accurate calculation of the dose to a patient difficult in situations where density

inhomogeneities or atomic number variations are present. The tumour control probability and normal tissue complication probability are very sensitive to absorbed dose[40] and therefore accurate dose calculation algorithms are needed.

The accuracy of dose calculation algorithms installed on commercial treatment planning systems is dependent on how rigorously the actual physical particle transport processes are modelled. Until the recent availability and affordability of adequately powerful computers on which to base treatment planning systems, rigorous dose calculations were impractical for routine treatment planning because of the excessive computation time required. Currently, much research is being conducted to develop sophisticated, accurate dose calculation software which can take advantage of the powerful hardware available. The ideal dose calculation method should: (i) include 3-D geometry, (ii) use 3-D density [CT] information, (iii) utilise a 3-D description of the beam, (iv) include 3-D scatter and interface effects within the patient, (v) calculate the dose at all points in the volume and (vi) be fast enough for routine clinical use.[49] The challenge for designers of dose calculation algorithms is to incorporate (i) through (v) without needing excessive computation time (and ultimately calculate dose in real time). The advantages and disadvantages of the currently used dose calculation algorithms for photon and electron beam planning, as well as contemporary algorithms yet to be used in treatment planning are discussed in this chapter.

Realistic dose calculation algorithms require accurate incident beam data or beam characterisation to obtain results consistent with experiment. With beam modelling techniques such as the implementation of BEAM[50] and other models,[51, 52, 17, 46, 53, 54, 55] accurate beam data is available.

2.2 Photon beam dose calculation algorithms

Inhomogeneity corrections for photon beams can be broadly grouped into four categories (i) those that correct for primary photon transport only (eg. effective pathlength), (ii) those that correct for primary and scattered photon transport (eg. the Equivalent Tissue-Air Ratio method), (iii) those that account for primary and scattered photons, and charged particle transport by macroscopic means (eg. superposition) and (iv) those that account for primary and scattered photon transport, and charged particle transport by modelling microscopic interactions (eg. Monte Carlo).

2.2.1 The Effective Pathlength method

The effective pathlength method uses a simple correction factor to modify depth dose data. The correction factor is a ratio of the dose at the radiological depth to dose at the geometrical depth in water, and an inverse square correction to account for the difference in distance from the beam source to the radiological and geometrical depths respectively.

The radiological depth, d', of point d, is found by summing the product of the thickness, l, and the density, ρ, of the material that each ray passes through,

$$d' = \sum_{i=surface}^{d} l_i \rho_i. \tag{2.1}$$

The dose to this point, $D(d)$, is found from a dose distribution measured in water, modified by the effective depth and inverse square fall-off,

$$D(d) = D_w(d') \times \frac{(SSD + d')^2}{(SSD + d)^2} \tag{2.2}$$

where $D_w(d')$ is the dose value in water at depth d'.

The result gives a consistent overprediction of dose in low density media because this method only scales depth dose data, and does not attempt to correct for secondary interactions.

2.2.2 The Equivalent Tissue-Air Ratio method

Introduction

The Equivalent Tissue-Air Ratio (ETAR) method devised by Sontag and Cunningham[56] was the first algorithm which attempted to correct for the scatter dose component. This correction is achieved by scaling the beam size in proportion to the lateral electron density distribution and associated photon scattering. At each calculation point, the contribution of surrounding voxels to the scatter dose is calculated using weighting factors. The scatter dose is then calculated as that which would exist in a unit density medium with the same effective beam radius.

ETAR is a scatter function model (calculates scatter dose separately) taking some account of the density distribution throughout the medium in calculating the dose to a point. ETAR uses two simplifications (i) CT slice coalescing to produce a single CT slice from which to calculate effective radii at an appropriate offset from the calculation plane and (ii) the use of geometric distances instead of radiological distances when the weighting factors are calculated.

The ETAR method relies on O'Connor's range scaling theorem[57] which predicts that the dose to a point in a homogeneous non-unit density medium is the same as the dose to a point in a unit density medium provided the depth and beam radius are scaled with density.

Tissue-Air Ratio

A Tissue-Air Ratio (TAR) is the ratio of the dose at a given point in tissue to the dose in air at the same point. A TAR describes the effect of attenuation (by the effective pathlength) and scatter (by the effective radius) on X-ray beams. A TAR can written as a sum of these two components,

$$TAR(d,r) = TAR(d,0) + SAR(d,r), \tag{2.3}$$

where $TAR(d,r)$ is the TAR at depth d and radius r, $TAR(d,0)$ is the TAR for primary radiation only, and $SAR(d,r)$ is the Scatter-Air Ratio (SAR) used to calculate the amount of scattered radiation in a phantom. Similar to a TAR, a SAR is defined as the ratio of the scatter dose at a given point in tissue to that in air at the same point.

Method

The inhomogeneity correction factor, CF, is defined as

$$CF = \frac{TAR(d',r')}{TAR(d,r)}, \tag{2.4}$$

where d' is the radiological depth (which accounts for the modification in primary dose), and r' is the radius of the equivalent homogeneous medium of unit density (to account for the relative 'scattering power' of neighbouring voxels). r' is found by first calculating the effective density, ρ', by performing a weighted sum of the density elements $\rho_{i,j,k}$ represented by pixels in CT scans surrounding the calculation point (a 3-D summation),

$$\rho' = \frac{\sum_{i,j,k} \rho_{i,j,k} W_{i,j,k}}{\sum_{i,j,k} W_{i,j,k}}, \tag{2.5}$$

where $W_{i,j,k}$ are the weighting factors for each of the density volume elements in the irradiated volume. In practice this 3-D summation is too time consuming so the CT

scans are coalesced into one slice. For each i, j in the condensed scan, these is an effective density $\rho_{i,j}$. The effective density ρ' is found from the 2-D summation,

$$\rho' = \frac{\sum_{i,j} \rho_{i,j} W_{d'}}{\sum_{i,j} W_{d'}}. \tag{2.6}$$

r' is simply the beam radius multiplied by the effective density.

Results

A problem with ETAR is that is cannot account for electronic disequilibrium. Scatter function models cannot predict situations of electronic disequilibrium because they rely on TAR measurements obtained under equilibrium conditions to calculate the primary and scatter dose components. This assumption is valid for low energy photons (eg. ^{60}Co) as the range of the secondary electrons produced is small, but not for megavoltage beams. Figure 2.1 shows the central axis depth dose curves in a lung phantom for a 5x5 cm^2 18 MV beam, as measured by experiment and calculated by ETAR and superposition. Because of the low density of the lung tissue, the secondary electron range is increased, and hence electrons scattered from the central axis of the beam are not replaced by electrons scattered into the central axis, resulting in a situation of electronic disequilibrium at the central aixs. The ETAR calculations significantly overpredict the dose in lung as the electronic disequilibrium at the central axis in the lung region is not accounted for.

2.2.3 The Delta Volume method

The Delta-Volume method[58] uses an approach similar to the differential scatter-air ratio method[59] for the first-scatter contribution, and a method similar to ETAR in approximating the primary and multiple scatter contribution. This method assumes electronic equilibrium exists and that Compton scatter dominates when calculating dose.

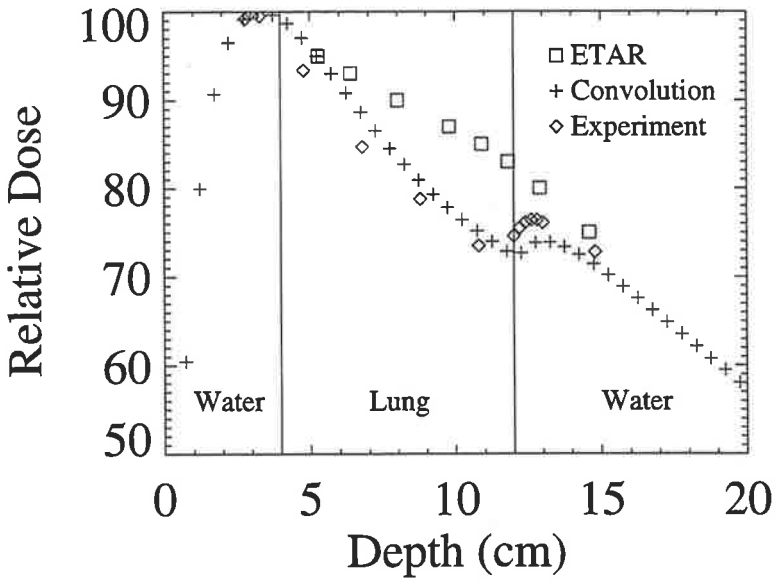

Figure 2.1: **Convolution, ETAR and experimental depth dose curves in a lung phantom for a 5x5 cm^2 18 MV beam. The curves are normalised to 100% at the depth of maximum dose. The density from 0–4 cm and 12–20 cm is 1.0 g cm^{-3} and from 4–12 cm is 0.3 g cm^{-3}. The experimental measurements are courtesy of Metcalfe** *et al.*[6]

Scattered dose is accounted for by a two-stage approach (i) a first-scatter dose is calculated by ray-tracing, to which is added the second-scatter component, assumed to be in the same direction as the first scatter component, and (ii) the residual multiple scatter dose is approximated by a function such that the total dose calculation accounts for the effects of small voids on the dose in water and the dose in homogeneous non-unit density media.

Experimental results in a variety of phantoms give maximum errors of less than 3% (less than those found for other scatter function models). However, only ^{60}Co beams were used in the experimental verification,[58] so the range of the secondary electrons is small and electronic equilibrium exists. The delta-volume method will not accurately predict dose in regions of electronic disequilibrium.

2.2.4 The Monte Carlo method

Introduction

Monte Carlo techniques involve simulating physical and mathematical situations by the sampling of random variables. These methods are well suited to the simulation of particle transport, since probability is implicit in the quantum mechanical interaction of the particles. Full Monte Carlo modelling is a direct simulation of the physical processes occurring in radiation transport, and therefore has the capability of giving results as accurately as statistical errors (and the mathematical representation of the physical processes) will allow, if the radiation source and phantom are accurately modelled.[60, 61, 62]

To calculate dose using Monte Carlo radiation transport simulations, the input data required are the phase space (location, direction and energy) of the incident particles and the composition of the absorbing medium.

The two main Monte Carlo codes used in medical physics are Electron Gamma Shower version 4 (EGS4)[8, 63] and Electron TRANsport (ETRAN)[9, 64] though there are a number of other codes in use such as the Integrated Tiger Series (ITS)[65, 66] code (a derivative of ETRAN), the Monte Carlo Neutron-Photon (MCNP)[67] code, and the PEREGRINE[68, 69] all-particle Monte Carlo code. These programs explicitly model coupled photon and electron transport through arbitrary media and geometries using quantum mechanically derived cross-section, scattering and particle production routines.

Electron Gamma Shower version 4 (EGS4)

Originally developed for high energy physics at Stanford Linear Accelerator Center, the most commonly used and cited Monte Carlo code used in medical physics research is EGS4. EGS4 is freely available from the ftp site: anonymous@nrcnet0.nrc.ca [132.246.160.2], has its own World Wide Web site: http://ehssun.lbl.gov/egs/egs.html, and EGS4-related discussions are held on the listserver: egs4-l@slacvm.bitnet.

EGS4 consists of both user-written code and EGS4 code. The user-code consists of three sub-programs:

(i) MAIN sets up the simulation parameters, initialises particle histories and outputs the results of the simulation,

(ii) HOWFAR is a geometry routine, where the distance from the particle to the nearest region boundary is calculated before a particle step is taken, and the step is modified if necessary. The geometry can include structures defined in Cartesian, cylindrical, polar, elliptical etc co-ordinates, and

(iii) AUSGAB is a scoring routine where the particle parameters, such as dose deposition, particle energy, position and angle are recorded.

The EGS4 code system has four main subroutines:

(i) HATCH performs a once-only initialisation for an EGS4 simulation by reading material data for the media from a data set that has been previously created by PEGS4 (a pre-processor for EGS4 which calculates cross-sections, branching ratios and scattering coefficients for the absorbing media),
(ii) SHOWER is called to initiate a particle history, given the particle's initial position, charge, direction and energy,
(iii) ELECTR transports all electrons initiated by SHOWER, and any subsequently produced electrons (eg in pair production interactions), and similarly
(iv) PHOTON transports all photons produced by SHOWER, and any subsequently produced photons (eg in bremsstrahlung interactions).

The physical processes of electron transport are bremsstrahlung production (BREMS), Bhahba[19] (BHAHBA) and Møller[18] (MOLLER) scattering, annihilation[13] (ANNIH), Molière scattering[33, 34] (MSCAT) and ionisational losses. The photon interaction processes are Compton scattering (COMPT), pair production (PAIR) and photoelectric interactions (PHOTO). These processes are outlined in chapter 1.

Figure 2.2 shows the structure of EGS4, and the relationships of the various subroutines to the user-written code.

To calculate electron transport, each incident particle, and any particle subsequently set in motion, is transported until its energy drops below a cut-off value (see below) or has left the geometry defined in the simulation. The position of interaction, type of interaction and the energy and direction of the particles after interaction, are calculated using random numbers to sample the relevant probability distribution produced from physical formulae. The physical set up of the simulation, such as field size, SSD and particle energy are specified in the input file, as well as the geometry and composition of the medium (eg. a slab of water divided into a number of cubic voxels). The output options, such as energy deposited in the water voxels, are also specified in the input file. As the number of particle histories simulated increases, statistical fluctuations decrease, and hence the results obtained become more reproducible and, if the setup is accurate,

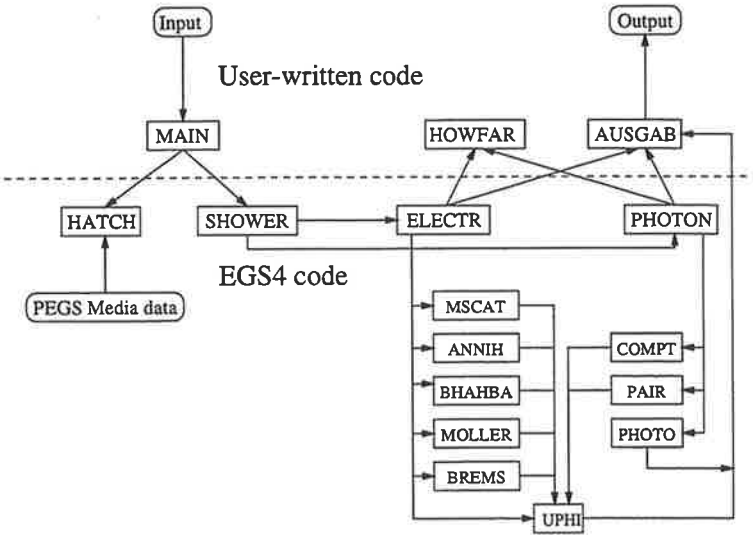

Figure 2.2: **The structure of EGS4, and the relationships of the various subroutines to the user-written code.**

approach those which would be obtained experimentally.[1]

Electron-photon transport in EGS4 requires four energy cut-off parameters: AE, AP, ECUT and PCUT. AE (electrons) and AP (photons) are the energy loss cut-off values, below which discrete energy loss events, such as δ-ray and bremsstrahlung production, do not occur, and these energy losses are included in the stopping power. ECUT (electrons) and PCUT (photons) are the energy transport cut-off values, below which a particle is discarded, and its remaining kinetic energy is deposited locally. Increasing these parameters can significantly reduce computation time, at the expense of a decrease in the accuracy of the results obtained.[8]

The EGS4 code has been shown to be accurate to within experimental error in many situations.[60] Figure 2.3 (courtesy Shortt *et al.*[70]) shows experimental and EGS4 calculated depth dose distributions from a 20 MeV beam of electrons incident on a water phantom with air and aluminium cylinders at 2 mm depth. Excellent agreement is found

[1]The number of particles per joule delivered experimentally is of the order of 10^{12}, and hence the statistical uncertainty in energy deposition experimentally is reduced to a negligible value.

between EGS4 and experimental results in all three situations.

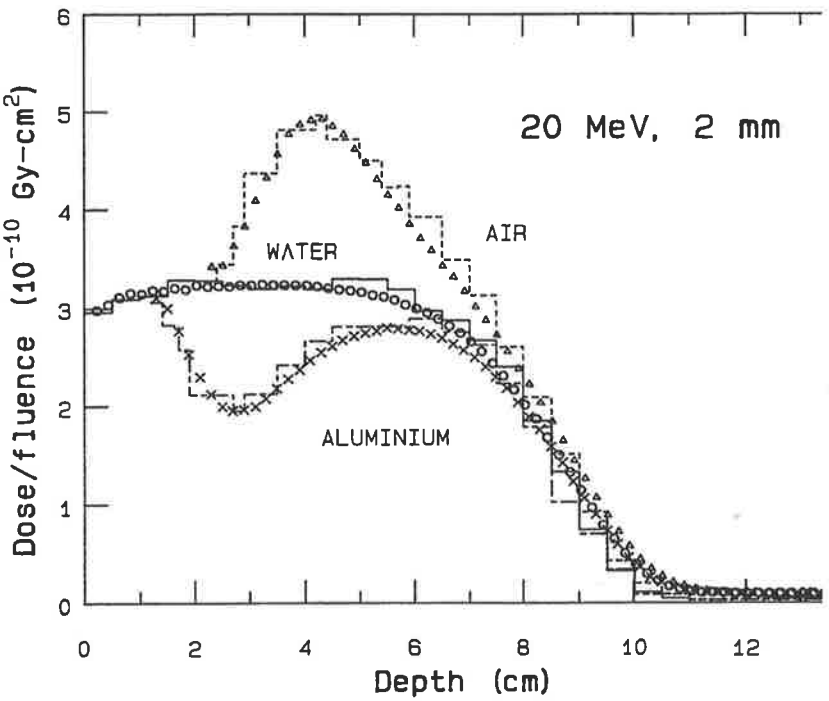

Figure 2.3: **Depth dose distributions from a 20 MeV beam of electrons incident on a water phantom with air and aluminium cylinders at 2 mm depth. The o's represent measured homogeneous phantom data, the x's the case with the aluminium cylinder, the triangles the case with the air cylinder. The histograms are EGS4 calculated results. Figure courtesy Shortt *et al.*[70]**

Electron TRANsport (ETRAN)

The ETRAN[9, 64] Monte Carlo codes have been developed at the (US) National Bureau of Standards over the past 25 years. In its current form, ETRAN is accurate for transport of electrons above 10-20 keV (in low atomic number materials) to 1 GeV. The current version accounts for incident electrons, positrons and photons, and all secondary radiations, including knock-on electrons, bremsstrahlung and annihilation radiation, Compton electrons, photoelectrons, electron/positron pairs, K-shell characteristic X-rays and Auger electrons.

Because the individual elastic and inelastic Coulomb interactions that occur during the passage of a high energy electron through matter are too numerous to simulate directly (currently!), the electron trajectories are condensed into macroscopic steps, each representing numerous interactions (multiple scattering steps). For each segment, the net angular deflection and energy loss are sampled from the Goudsmit-Saunderson (GS) multiple scattering distribution.[32]

The advantages of GS theory over Molière theory (used by EGS4) are that the GS theory is not derived in a small angular approximation, so is exact for any angle, and it can be evaluated with any desired single scattering cross section (however by modifying the Molière formalism according to Bethe[71] by a $\sqrt{\sin\theta/\theta}$ term, large angle scattering can be accounted for as well).

As with EGS4, ETRAN has been shown to agree with experimental results for a wide variety of physical situations.[72] Figure 2.4 (from Berger[72]) shows a comparison of ETRAN calculated, moment method calculated (from Spencer[73]) and measured (from McLaughlin and Hussman[74]) depth dose curves from 3 MeV electrons incident on aluminium. Close agreement is obtained between ETRAN and experimental results.

Comparing EGS and ETRAN

Apart from using different multiple scattering theories, ETRAN and EGS differ in the creation and transport of secondary particles. ETRAN accounts for this within the multiple scattering theory, and the creation of a secondary electron does not directly affect the primary electron (a class I algorithm[75]). However EGS explicitly creates and transports secondary electrons, and the energy of the primary electron is directly correlated to the creation of secondary electrons (a class II algorithm).

ETRAN transports electrons more rigorously than EGS at low energies as it uses the total Compton cross-section for bound electrons, whereas EGS uses only the free electron cross

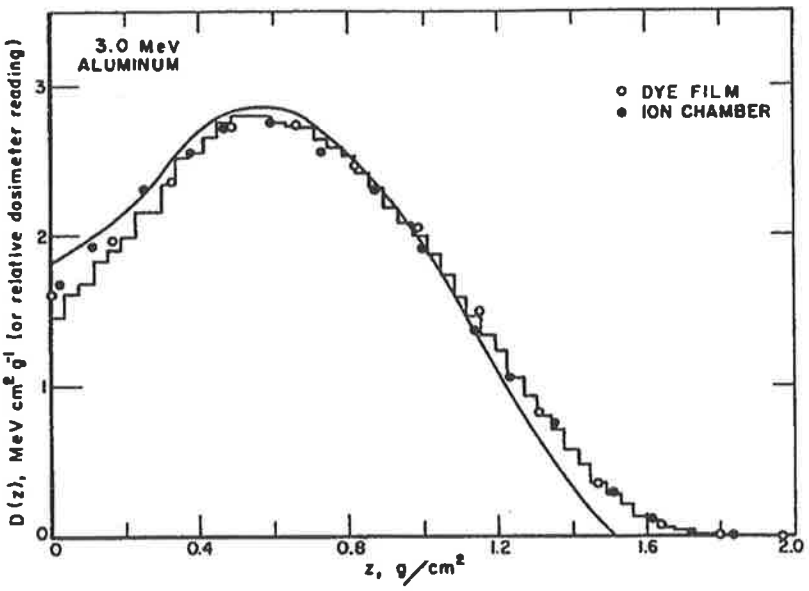

Figure 2.4: **A comparison of ETRAN (histogram) and measured (dots) depth dose curves for 3 MeV electrons incident on aluminium. (The solid curve is from a moment method). Figure courtesy of Berger.[72]**

section. Also, EGS does not generate fluorescent photons or Auger electrons after a photoelectric event while ETRAN does. However EGS includes Rayleigh scattering which ETRAN ignores.[76]

The electron transport step length is determined in ETRAN by decreasing the electron's energy by an (on average) constant fraction. However EGS allows all physical processes and boundaries to affect the choice of step size.[76]

ETRAN is a packaged code in which the user only need install the code and then prepare the appropriate input files. The code then produces its standard output which includes energy and charge deposition within regions, fluence spectra within regions etc. With the EGS system, it is up to the individual user to write a user code (such as INHOM[8] and the RTP series[77]). This gives the user much flexibility in terms of geometry and scoring quantities, however the user needs to know much more about the details of the system. It also means that EGS can more easily be adapted to execute efficiently for a

particular problem by taking advantage of variance reduction techniques.[78] Therefore ETRAN is easier for certain situations, however is virtually impossible to adapt to specific situations; for such problems EGS has many advantages.[76]

Summary

The only limitation of these Monte Carlo codes is the computation time needed to obtain a dose distribution, and of course errors in set-up or analysis at the human interface. The time limitation prohibits the use of Monte Carlo for routine planning with today's technology. The challenge is to create an electron dose calculation algorithm approaching the accuracy of Monte Carlo, which can be calculated in a clinically realistic time, and eventually real time.

Already codes are being developed, such as the PENELOPE[79] code, which model individual elastic and inelastic particle scattering events. The simulation of individual scattering events are likely to be a standard feature for future Monte Carlo particle transport codes, however, they will require even more intensive computation.

2.2.5 The Superposition/Convolution method

Introduction

The *convolution* of two functions $f(x)$ and $g(x)$, denoted $f \otimes g$, is defined as[80]

$$f(x) \otimes g(x) = \int_{-\infty}^{\infty} f(u)g(x-u)du. \tag{2.7}$$

If the function $g(x-u)$ is variant (ie. dependent on another variable such as mass

density), the convolution becomes a *superposition.*

Superposition/convolution methods for photon beam dose calculation have been under development for the past decade, and have been shown by many researchers to provide accurate and time efficient dose calculation.[16, 81, 82, 83, 84, 85, 86, 87, 88, 44, 89, 6, 90, 91] The superposition technique accounts for the range of secondary electrons, and hence situations of electronic disequilibrium: in particular, the increased range of electrons in lung, and the resulting lateral electronic disequilibrium, is explicitly modelled. Metcalfe *et al.*[6] showed that ignoring secondary electron range can lead to large errors in the dose calculated by methods which only account accurately for scattered photons, such as the ETAR[56] algorithm described in section 2.2.2.

Method

In a convolution calculation, the total energy released per unit mass (*terma*[16]) is convolved with *energy deposition kernels*[87] to obtain the dose distribution, as shown schematically in figure 2.5. For a medium that is in general inhomogeneous, the dose at a point $\mathbf{r}$ is given by[86, 88]

$$D(\mathbf{r}) = \int_{\mathbf{r}'} T(\mathbf{r}')\rho(\mathbf{r}')H(\mathbf{r}-\mathbf{r}', \rho_{ave})/\rho_{ave} d^3\mathbf{r}', \tag{2.8}$$

where $T(\mathbf{r}')$ is the terma at a photon interaction site $\mathbf{r}'$ and $H(\mathbf{r}-\mathbf{r}', \rho_{ave})$ is the energy deposition kernel value for a dispacement $\mathbf{r}-\mathbf{r}'$ in a medium where the average density between $\mathbf{r}$ and $\mathbf{r}'$ is ρ_{ave}.

Conventional convolution algorithms rely on a rectilinear density scaling method based on O'Connor's theorem[57] to account for secondary electron and scattered photon transport in inhomogeneous media. The rectilinear scaling method is discussed in detail below.

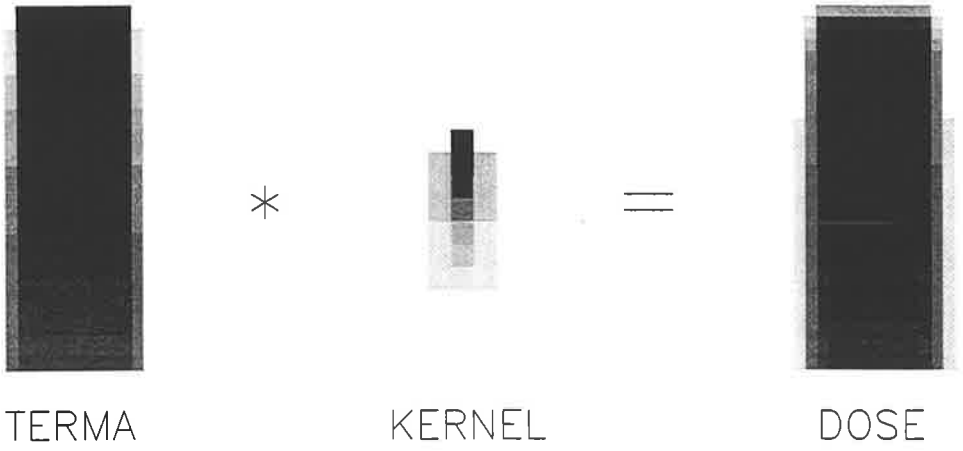

Figure 2.5: **The dose is obtained by convolving the terma with the energy deposition kernels.**

Constructing kernels for experimental beams

In order to calculate dose using convolution for experimental beams both the terma and the kernels need to be accurately defined. Experimental photon beams have a spectrum of photon energies, which soften off axis (refer section 1.7.1), and it is often difficult to obtain kernels to fit these beams.

Single value decomposition or simulated annealing optimisation can be used to extract kernels from experimentally derived dose distributions[92, 93] (without requiring Monte Carlo or analytically generated kernels). Methods which use Monte Carlo energy deposition kernels use previously derived beam spectra such as those published by Mohan *et al.*[43] and Ahnesjö *et al.*[82] These spectra can be adjusted to fit dose distributions for individual clinical beams. Analytical kernels have been constructed using multiple scattering theory.[94]

Kernel tilting

Clinical photon beams originate from a virtually point source. Therefore, for a finite field size at the patient plane, the photons off-axis will be divergent. In creating the kernels, the energy deposition grid is aligned in the incident photon direction, so it is logical that for a divergent beam the energy deposition grid should be orientated (or tilted) in line with the photon direction. However, in tilting the kernels they are no longer aligned with the dose grid, and a computationally expensive kernel tilting operation is needed to transform the tilted kernel onto the dose grid. Sharpe and Battista[91] conducted a study of kernel tilting in homogeneous media, and concluded that the difference between a calculation incorporating kernel tilting and that incorporating only parallel kernels showed differences of less than 3% for SSD's greater than 80 cm. However, they state that the validity of the parallel kernel approximation in the presence of tissue heterogeneities requires further study, as the importance of kernel orientation may be accentuated near low density structures because of the increased range of secondary photons and electrons. Throughout this thesis the parallel kernel approximation is made when using superposition-based calculations.

The rectilinear density scaling method

Using rectilinear scaling, the average density between the interaction and the deposition site, ρ_{ave}, is

$$\rho_{ave} = \frac{1}{r - r'} \int_{\mathbf{r}'}^{\mathbf{r}} \rho(\mathbf{r})\, d\mathbf{r}. \tag{2.9}$$

Woo and Cunningham[95] showed that using rectilinear scaling for secondary electron transport leads to an over-estimation in dose in a layer beyond a high to low density interface due to primary interactions before the interface. This over-estimation is because the largest contribution to lateral electron spread at a plane is from scattering events furthest from the plane, and this effect is not accounted for by rectilinear scaling.[88]

Similarly, the dose beyond a low to high density interface due to primary interactions before the interface is underestimated. Evidence of this problem is highlighted in figure 2.6, where Monte Carlo dotplots of the electrons resulting from 100 incident 5 MeV photons traversing (a) a low density region (0.25 g cm^{-3}) to a high density region (1.0 g cm^{-3}), and (b) a high density region to a low density region, are shown. The dashed lines shown in figure 2.6 are where the average density from the interaction site is the same in both plots. Note that the spread of electrons at the dashed line plane in the low to high density case (left) is significantly narrower than the spread of electrons in the high to low density case (right). This difference is because in the high to low density case (right), the bulk of the scattering is occurring closer to the interaction site and hence gives a wider projection at the deposition layer, whereas the opposite is occurring in the low to high density case. The current rectilinear scaling method assumes the spread to be the same in both cases, and ignores the density distribution between the interaction and deposition site.

The dose due to electrons set in motion at the interaction site (primary dose) makes up most of the total dose,[96] especially for small fields. Hence, any errors in the primary dose will result in similarly sized errors in the total dose. The rectilinear approximation is valid for dose due to electrons set in motion by scattered photons (scatter dose)[96, 97] since the photons travel in straight lines from the interaction site, and the range of the subsequently ejected electrons is much less than the mean free path of the scattered photons. These scattered photons can produce further scattered photons, to which the rectilinear density scaling method is not valid, but the dose contribution from these second and multiply scattered photons is small.[81]

Results

Figure 2.1 shows depth dose curves for a 5×5 cm^2, 18 MV beam in a water-lung-water phantom predicted by superposition (using rectilinear scaling) and ETAR. Also shown

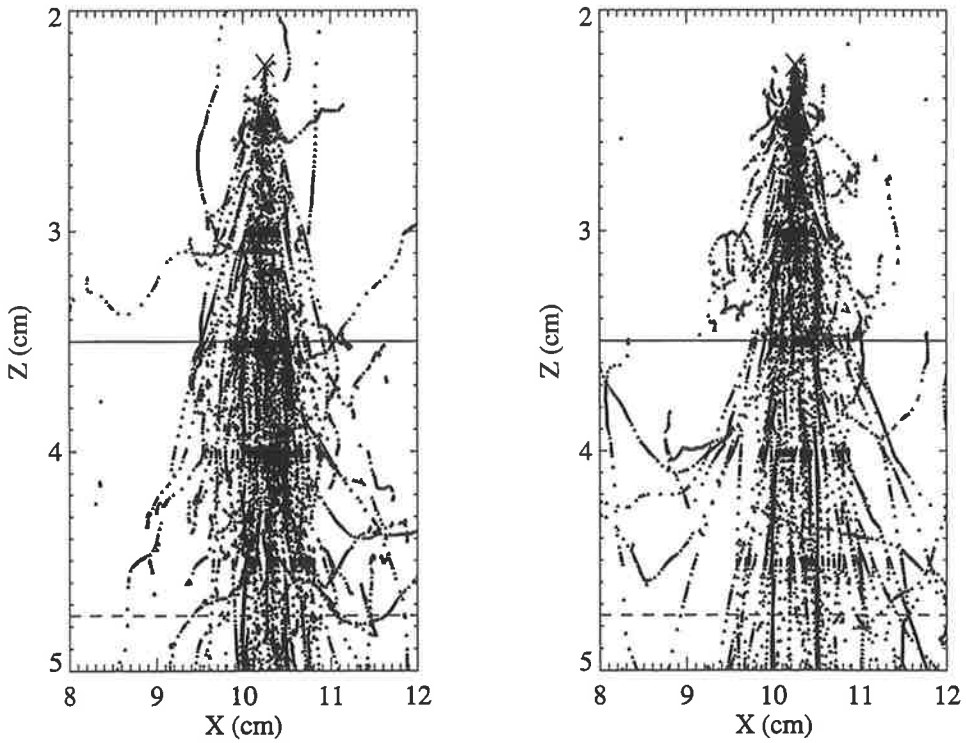

Figure 2.6: **Monte Carlo generated dotplots of electrons ejected by 5 MeV photons forced to interact at X. The plot on the left shows a low to high density geometry (0.25-1.0 g cm^{-3}) while the plot on the right shows a high to low density geometry. The solid line shows the boundary between the media of different density, and the dashed line in both plots is a line of equivalent average density from the interaction site. These plots were obtained using Monte Carlo by forcing photon interactions at X, and recording the x and z positions of the subsequently ejected electrons as they were transported through the medium.**

are experimental results from Metcalfe *et al.*[6] This figure shows that the superposition curve is much closer to the experimental curve than is the ETAR curve. However, there is still a dose discrepancy in the superposition curve of approximately 5% in the beginning of the lung region (at 6 cm deep) and 3% in the build-up part at the second water interface. The superposition algorithm accounts for electronic disequilibrium, but not for the different scattering conditions across the water/lung interface, and the lung/water interface.

2.2.6 Variations of superposition

Single polyenergetic superposition vs components superposition

Clinical X-ray beams are composed of photons with a spectrum of energies. Superposition for a beam composed of a spectrum of photon energies can be performed either by summing monoenergetic kernels to obtain a polyenergetic kernel prior to the convolution (single polyenergetic method), or alternatively by performing a separate convolution for each component of the photon beam spectra (components method) weighted according to the photon spectrum. For a spectrum of N bins, the components method will take up to N times as long to calculate as the single polyenergetic method.

The terma calculation accounts for the loss of primary photons from the beam correctly, but does not account for the different fraction of energy given to secondary electrons as the average energy of the beam increases with depth, nor does it account for the increased range of the secondary electrons with depth due to the increasing average energy. The single polyenergetic method has these limitations, which are overcome by the components method (at the expense of increased computation time).

Methods have been proposed to account for the change in the fraction of energy given to

secondary electrons when using the single polyenergetic superposition method.[44, 98, 99] None of these methods account for the increased range of the secondary electrons, but this has little effect on the dose distribution. Throughout this thesis, the single polyenergetic method is used for the superposition calculations.

Collapsed cone convolution

In order to increase the speed of convolution calculations, Ahnesjö[81] proposed the collapsed cone convolution (CCC) method (also called run-length raytracing[100]). In CCC the energy deposition kernel is divided into a number of cones, with each cone radiating away from the interaction site and contributing to a fraction of the solid angle around the interaction site. The energy deposited along each cone is 'collapsed' into a line which passes through the centre of the cone. The energy deposition along this line is then described by an analytic function. Hence the kernel becomes a number of energy deposition lines. This implementation reduces the superposition time from being proportional to N^6, to being proportional to MN^3, where N is the number of voxels along one side of the dose grid, and M is the number of cones to be considered for each point. As the number of cones decreases the computation time decreases, but less voxels are intersected by cones, so the accuracy of the method also decreases. CCC has been implemented on two radiotherapy treatment planning systems, TMS[101] and PINNACLE3.[102]

Fourier transform convolution

For a homogeneous medium (where the kernel is invariant, and the calculation is a true convolution) the convolution can be performed in Fourier space,[83, 103, 104, 105, 106, 107, 108]

$$\mathcal{F}(D) = \mathcal{F}(T) \times \mathcal{F}(H), \tag{2.10}$$

where $\mathcal{F}$ denotes the Fourier transform operation. The use of fast Fourier transforms[80] increases the speed of the convolution calculation (eg. by a factor of 250 times for a 64×64×64 matrix[104]), however the Fourier transform is strictly only valid for homogeneous, water equivalent phantoms with monoenergetic, monodirectional photon beams.

Atomic number effects superposition

Apart from the limitation of rectilinear scaling at interfaces, another limitation of superposition is that it takes no account of the effect of non-waterlike composition materials on the radiation transport. Papanikolau and Mackie[109] extended the superposition method to include the effects of higher atomic number (Z>8) inhomogeneities that can be encountered in clinical situations.

Superposition kernels were computed for media with varying atomic numbers, and the raytracing and kernel scaling was implemented so that when a medium interface is crossed, the kernel specific to that medium is used in the superposition equation. This algorithm was tested for different photon energies and the results were in good agreement with measurements.

2.3 Electron beam dose calculation algorithms

2.3.1 Introduction

Electron beam radiotherapy is the treatment mode of choice for a number of treatment situations. Tumours of the skin, or at shallow depths are particularly suited to electron beam treatment because the electron beam dose distribution is uniform to a well defined

depth, after which the dose falls off rapidly as the electrons lose energy and stop. Dose can thus be delivered to a shallow or superficial tumour while minimising dose to the underlying healthy tissue. The increased use of electron beam therapy has encouraged the development of accurate electron beam dose calculation algorithms. Most computerised treatment planning systems can now be used for electron beam planning, however clinical electron beam dose calculation algorithms are not as well developed as those for photon beam planning, and hence have been shown to produce dosimetric errors of up to 40%.[7, 110] When the electron field is only used as a 'boost' (eg. 10 Gy out of a total treatment of 60 Gy), the overall error becomes small. However, the accuracy becomes significant for large non-boost treatments involving cavities.

This section reviews the two currently implemented methods of electron beam dose calculation on clinically used radiotherapy treatment planning systems, the Effective Depth Method[3] and the Pencil Beam Method[111, 112, 113, 47, 114, 115, 116, 117, 38] and also the more advanced analytical based calculations of the 3-D Pencil Beam method,[118, 119, 29] Pencil Beam Redefinition,[120, 121, 122, 36] the Multi- ray model,[123, 124] David Jette's multiple scattering work,[37, 125, 126, 127, 128, 129, 130, 131] Phase Space Evolution,[132, 133, 134] and the Monte Carlo based algorithms of ETRAN,[9, 64] EGS4,[8, 63] Superposition[135, 136, 137] and Macro-Monte Carlo.[138, 139] Where possible, a dose calculation result for each method is compared to experiment or Monte Carlo. As different geometries have been studied in the literature it is not possible to compare the accuracy or computation time of these methods for the same geometry.

2.3.2 The Effective Depth method

In the effective depth method[3] [also called the Coefficient of Equivalent Thickness (CET) method[140]] each point in the dose calculation matrix is assigned a radiological depth by a ray trace from the surface to the calculation point, as in the effective pathlength method for photon beams (refer section 2.2.1). The dose $D(d)$, is found from

a dose distribution measured in water, modified by the effective depth and inverse square fall-off,

$$D(d) = D_w(d') \times \frac{(SSD + d')^2}{(SSD + d)^2}. \tag{2.11}$$

Note that the SSD for electron beams is a measured quantity due to the scattering in the foils and air. It generally lies between the two foils.

The effective depth method does not account for the change in the multiple scattering of electrons in heterogeneous media. As multiple scattering is the dominant physical process in electron beam radiotherapy[130] this method is prone to error. Increases in the dose in bone and soft tissue immediately downstream of bone, as well as the 'hot' and 'cold' spots lateral to the edge of the bone-water interface are not predicted.[141]

2.3.3 The Pencil Beam method

Introduction

A pencil beam refers to a beam of electrons of small cross-sectional area. The dose resulting from a broad beam can be calculated by summing the contribution from elemental pencil beams.

The most sophisticated electron beam algorithms installed on contemporary commercial treatment planning systems are based on the Pencil Beam Method. In the 2-D pencil beam method, the pencil beams are 'strip' beams, defined within the limit of the collimator projected to the calculation depth. There are currently two main pencil beam models: (i) the Gaussian model[111, 112, 47, 114, 115] which assumes that the dose due to each pencil beam has a Gaussian off-axis profile, and (ii) the generalised Gaussian model[113, 117, 116, 142] (a superposition of several Gaussian distributions), which takes large angle scattering events into account. The Gaussian model ignores important large

angle scattering processes, and assumes that electrons only undergo multiple small angle deflections. The true pencil beam dose profile is more sharply peaked than a Gaussian, and has longer tails.[117]

Theoretically any electron transport model can be used to calculate the angular scattering with depth. The resulting accuracy in the angular scattering calculations used in the electron transport (and hence the dose distribution) will depend on the assumptions and limitations used in the transport model. The most commonly used transport model is FE theory (refer section 1.4.3).

Method

Each pencil beam is considered to be composed of mono-energetic electrons having an angular divergence (mean angle), and a spread in angles about the mean angle. These parameters can be found using FE theory. The dose distribution resulting from each pencil beam can then be summed to give the dose distribution in the material lying beneath the collimator by

$$D(x,y,z) = \int\int_{collimator} W(x',y',0)d(x,y,z;x',y')dx'dy' \tag{2.12}$$

where $W(x',y',0)$ is the relative strength of the beam at $x',y',0$, and $d(x,y,z;x',y')$ is the dose contribution at (x,y,z) from a pencil beam whose central axis passes through (x',y',z).

Equation 2.12 is evaluated assuming the incident beam to be a collection of parallel pencil beams incident normally to the collimation plane (and hence the beam must be integrated over the projection of the collimator to the surface). In practice, the intensity profile of the beam at depth z is assumed to be due to the scattering occurring in the air (in the absence of the patient), given by the projected angular spread from the collimator

face, σ_{air}.[2] The further spread of each pencil beam, σ_{pat}, is then due only to the multiple Coulomb scattering occurring in the patient. This 'deconvolution' of the lateral pencil beam spread allows differences in scattering between adjacent pencil beams within the patient to have an effect, rather than being dominated by the scattering occurring in the air.

The Gaussian distributions from each pencil beam are summed to give a broad beam distribution using error function terms.

Using the method of Hogstrom *et al.*[112] for a rectangular field of size $WXZ \times WYZ$[3] and incorporating the 2-D inhomogeneity correction, equation 2.12 is redefined as[38]

$$\begin{aligned} D(x,y,z) = W(x,y)\sum_{i=1}^{N_x}\frac{1}{2}\left[erf\left(\frac{WXZ/2-x_i}{\sqrt{2}\sigma_{air}(z)}\right)+erf\left(\frac{WXZ/2+x_i}{\sqrt{2}\sigma_{air}(z)}\right)\right] \\ \times\frac{1}{2}\left[erf\left(\frac{x_i+\Delta x/2-x}{\sqrt{2}\sigma_{pat}(x_i,z)}\right)+erf\left(\frac{x_i-\Delta x/2-x}{\sqrt{2}\sigma_{pat}(x_i,z)}\right)\right] \\ \times\frac{1}{2}\left[erf\left(\frac{WYZ/2-y}{\sqrt{2}\sigma(x_i,z)}\right)+erf\left(\frac{WYZ/2+y}{\sqrt{2}\sigma(x_i,z)}\right)\right] \\ \times D^{\infty}_{H_2O}(0,0,Z_{eff}(x_i,z))\times\left[\frac{SSD+Z_{eff}(x_i,z)}{SSD+z}\right]^2, \end{aligned} \tag{2.13}$$

where erf is the standard error function, σ_{air} and σ_{pat} are the standard deviation of the lateral electron spread in air and the patient respectively, and Δx is the thickness of the strip beams (a beam of width WYZ and thickness Δx). The last term in equation 2.13 is a central axis depth dose factor for infinite field size multiplied by the inverse square law correction factor. This empirical term gives the correct central axis depth dose, which accounts for electron stopping, and buildup, which are not modelled properly by the FE theory.

Commercial implementations of this method have a number of serious limitations which

[2] $\sigma_{air} = \sigma_{\theta_x}(L_0+z)$, where σ_{θ_x} is the x-component of the angular standard deviation at the applicator face and (derived from beam profiles in air), and L_0 is the gap between the collimator face and the medium surface.

[3] $WXZ \times WYZ$ is the projected collimator size at z, given by $WX(1+z/SSD)$ and $WY(1+z/SSD)$ respectively.

reduce the accuracy of the calculations for various beam and patient configurations, such as:

(i) The algorithms are 2-dimensional. In calculating the dose distribution in a transverse cross section of the body (the x-z plane), the body is assumed to be invariant in the y-direction. This means that variations in body structure away from the plane of calculation have no effect on the calculation. Large errors can then arise, especially when small air cavities or bone regions exist.[119, 29]

(ii) Dose due to each pencil beam is calculated as though the body consisted of slabs with faces perpendicular to the beam (the infinite slab approximation), where the composition of the slabs is determined by the material encountered along the central axis of the pencil beam (for the central axis slice). It has been shown that this approximation can lead to errors of 10-20% in the dose behind an air cavity.[143]

(iii) The range of the electrons is finite and differences in electron range (range straggling) reduces the lateral spread of pencil beams at large depths which is not predicted by FE theory.[144] To overcome this limitation Werner *et al.*[47] and van Gasteren[144] proposed modifications to FE theory to take account of the finite range of the electrons. Also, Lax *et al.*[145, 116] used an empirical correction function obtained from the quotient between FE theory and the Monte Carlo calculations of Berger and Seltzer.[146] Bruinvis *et al.*[142] and Antolak *et al.*[147] included electron range straggling modifications to the FE theory, obtaining good agreement with Monte Carlo results in the angular distribution shape and radial width.

Results

Figure 2.7 (from Mah *et al.*[119]) shows the dose distribution behind a 1 cm long cylinder of hard bone irradiated by a 10 cm square field of 10 MeV electrons as measured experimentally and calculated by a 2-D pencil beam method. The 2-D calculation cannot distinguish between a 1 cm rod, and a rod which extends the full length of the field. The method will overpredict the dose to points just beneath the rod, because it assumes lateral scatter equilibrium in the y-direction, where in reality electrons are scattered away from the region below the rod and are not replaced by electrons scattering into

that region. Similarly, the 2-D model ignores inhomogeneities which are not in the plane of calculation, and the modification to electron fluence which they cause.

For air and aluminium slab beam geometries (1-D inhomogeneities) disagreements between pencil beam dose calculations and Monte Carlo results are rather small.[148] Differences are due to the lack of backscatter, lack of large angle scattering and the intrinsic small angle nature of the underlying theory. Cygler *et al.*[7] found up to a 40% underprediction of the hot spot in a 'spine' phantom and up to a 35% disagreement in a single aluminium cylinder phantom when the pencil beam method was compared to experimental results.

2.3.4 The 3-D Pencil Beam method

The 3-D pencil beam method[118, 119, 29] is a logical extension of the 2-D pencil beam model. In the 3-D case both beam dimensions are treated the same, instead of incorporating a y-scatter factor term. The 3-D algorithm has recently been implemented on some commercial treatment planning systems. This method requires the same input data as is already used in the 2-D method. To perform a 3-D heterogeneity correction, equation 2.12 becomes[29]

$$
\begin{aligned}
D(x,y,z) = \sum_{l=1}^{N_y}\sum_{k=1}^{N_x} W(x_k,y_l)\frac{1}{2}\left[erf\left(\frac{x_k+\Delta x/2-x}{\sqrt{2}\sigma_{pat}(x_k,y_l,z)}\right)-erf\left(\frac{x_k-\Delta x/2-x}{\sqrt{2}\sigma_{pat}(x_k,y_l,z)}\right)\right] \\
\times\frac{1}{2}\left[erf\left(\frac{y_l+\Delta y/2-y}{\sqrt{2}\sigma_{pat}(x_k,y_l,z)}\right)-erf\left(\frac{y_l-\Delta y/2-y}{\sqrt{2}\sigma_{pat}(x_k,y_l,z)}\right)\right] \\
\times D^{\infty}_{H_2O}(0,0,Z_{eff}(x_k,y_l,z))\times\left[\frac{SSD+Z_{eff}(x_k,y_l,z)}{SSD+z}\right]^2 \\
\times\frac{1}{2}\left[erf\left(\frac{WXZ/2-x_k}{\sqrt{2}\sigma_{air}(z)}\right)-erf\left(\frac{WXZ/2+x_k}{\sqrt{2}\sigma_{air}(z)}\right)\right] \\
\times\frac{1}{2}\left[erf\left(\frac{WYZ/2-y_l}{\sqrt{2}\sigma_{air}(z)}\right)-erf\left(\frac{WYZ/2+y_l}{\sqrt{2}\sigma_{air}(z)}\right)\right] \qquad (2.14)
\end{aligned}
$$

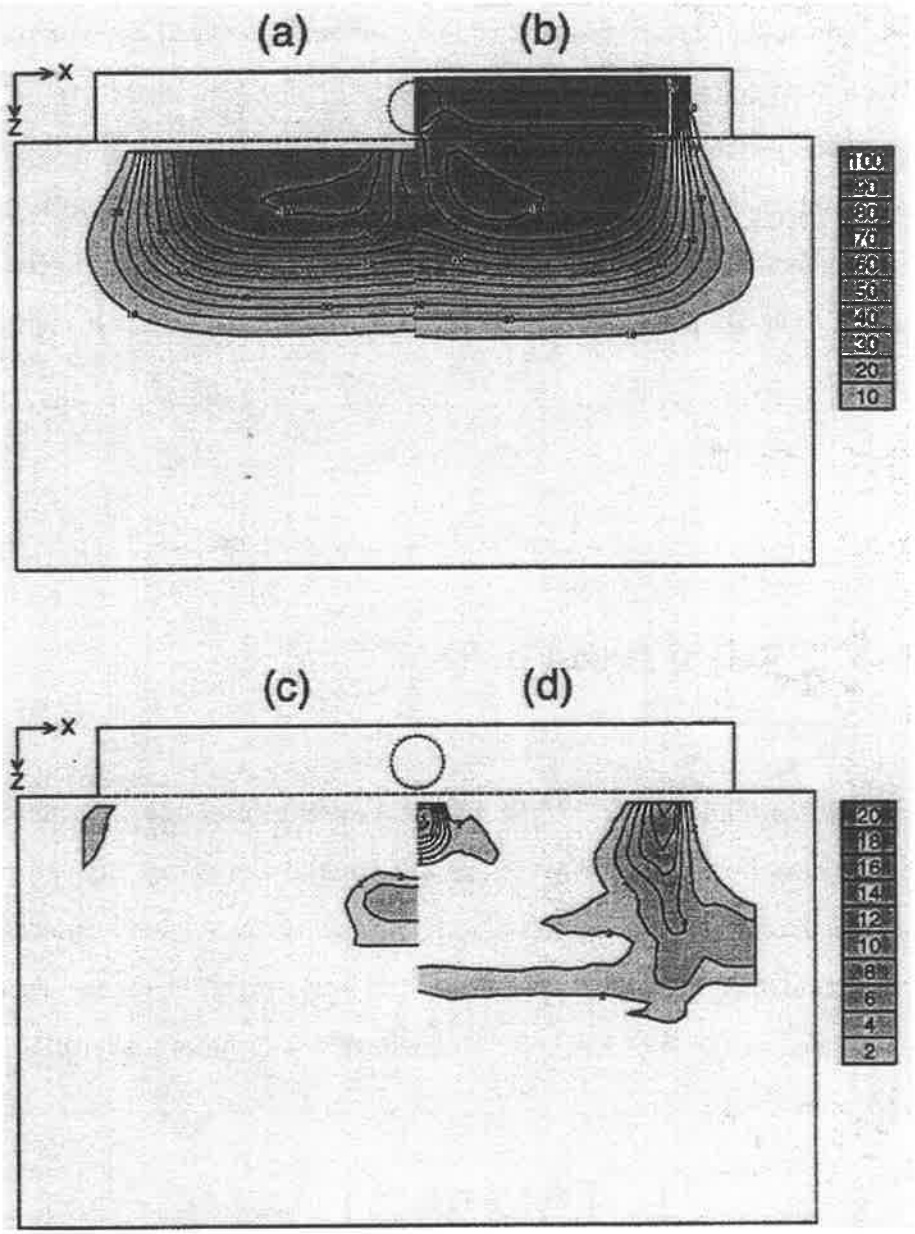

Figure 2.7: **The dose distribution behind a 1 cm long hard bone rod inserted in water, irradiated by a 10 cm square field of 10 MeV electrons: (a) measured distribution; (b) 2-D pencil beam calculated distribution; (c) measured greater than calculated; (d) calculated greater than measured. Figure courtesy Mah *et al.*[119]**

Figure 2.8 (from Mah *et al.*[119]) shows the dose distribution behind a 1 cm long cylinder of hard bone irradiated by a 10 cm square field of 10 MeV electrons as measured experimentally and calculated by a 3-D pencil beam method. The 3-D algorithm improves agreement with measurements over the 2-D algorithm as the off-axis length of the rod is accounted for. In the area of the bone the 25% error found using the 2-D method is reduced to 12%.[119] Both the 2-D and 3-D methods fail to predict the dose correctly in the penumbral region due to (i) the underprediction of large angle scattering and (ii) neglect of the initial angular distribution at the surface.

The 3-D algorithm is much better at predicting the enhanced and reduced dose regions below small inhomogeneities, such as bone and air cavities, since density changes in the y-direction are accounted for. However, residual errors in the 3-D method suggest further development is needed in the fundamental theory and implementation.[119]

For a 15 MeV 10×10 cm^2 beam, the time taken to calculate the dose distribution is 300 s on a VAXstation 3500,[29] four times slower than that of the 2-D method.

2.3.5 The Pencil Beam Redefinition algorithm

Introduction

Pencil beam redefinition[120, 121, 122, 36] (also termed the 'moments method') overcomes the 'infinite slab' approximation of the pencil beam model, in which a pencil beam at the surface is considered to penetrate through a slab-like medium defined by the material encountered along the central axis of the pencil beam. Rather, in the redefinition method, the lateral distribution of the pencil beam at each depth is used to redistribute electrons into adjacent pencil beams when the beam is propagated from one depth to the next. The parameters of the electron pencil beam are redefined continuously with depth in

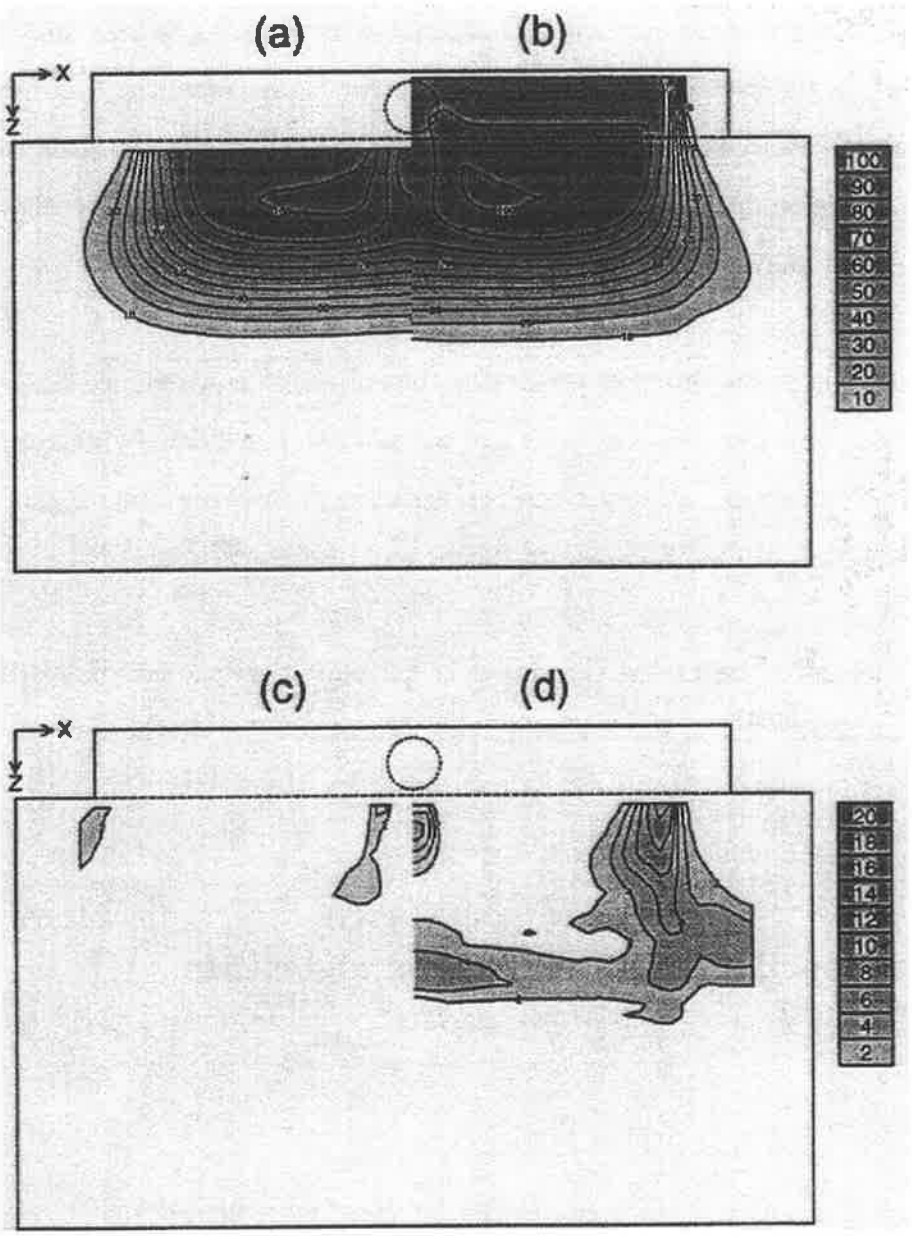

Figure 2.8: **The dose distribution behind a 1 cm long hard bone rod inserted in water, irradiated by a 10 cm square field of 10 MeV electrons: (a) measured distribution; (b) 3-D pencil beam calculated distribution; (c) measured greater than calculated; (d) calculated greater than measured. Figure courtesy Mah** *et al.*[119]

tissue by employing multiple energy and angular bins at each depth. The redefinition concept was first used by Hogstrom *et al.*[112] but was limited to a single redefinition.

As with the pencil beam method, it is possible to use various models of angular scattering: Shiu and Hogstrom[121, 122] used the approximation of a 3-term Gaussian function for the angular distribution, McLellan *et al.*[36] used a moments method to expand the angular distribution of each pencil beam in terms of a sum of Hermite polynomials to calculate higher moments of the angular distribution. However, although the accuracy of the generalised moments method increases with the number of moments calculated, the computation becomes increasingly complex.

Method

In the redefinition method, pencil beams are defined at points on the surface and may have initial energy and angular distributions. In propagating to the next layer, each angular bin is projected to determine the point at which electrons in that bin will reach. Scattering is simulated in each projection step so that electrons in each angular bin are redistributed into other bins after the step. The angular distribution is calculated from the scattering power of the current layer, and the distance to the next layer.

In each step, electrons lose energy and eventually stop. This energy loss per bin corresponds to energy deposition, and thus absorbed dose. The energy loss of electrons going from a depth z to $z + \Delta z$ is calculated by the product of the linear collisional stopping power of the medium and the path length $[\Delta z/\cos(\text{polar angle})]$. The mean electron energy in a pixel (at depth $z + \Delta z$) is then calculated, from which the projected angular distribution on the x-z and y-z planes are determined. The pencil beam is now redefined at depth $z + \Delta z$, with all the pencil beam parameters and mean energy available for each characteristic energy bin. The fluence is then calculated from the planar fluence for each energy bin.

In theory, the redefinition method can model electron transport and calculate a dose distribution without the necessity of adjusting the dose distribution to match measured data. However in practice, because only the most significant physical interactions of electrons with tissue have been modelled, an energy dependent correction factor is incorporated.

Results

Figure 2.9 (from Shiu and Hogstrom[122]) shows the dose distribution beneath a 0.5 cm thick bone at 2.0 cm depth of water situated in the centre of a 15 MeV, 10×10 cm^2 field at 100 cm SSD as measured and calculated by the redefinition algorithm and the M. D. Anderson Cancer Center 2-D pencil beam algorithm. The redefinition algorithm is able to predict the hot and cold spots beneath the bone better than that of the 2-D pencil beam algorithm.

The redefinition dose distribution shows better agreement with experimental results in both homogeneous and heterogeneous phantoms than do conventional pencil beam methods, especially in the region just distal to, and shadowed by the edge of the inhomogeneity. Shiu and Hogstrom[122] stated that discrepancies between redefinition and experiment may occur because energy straggling is not accounted for by their model.

McLellan *et al.*[36] are currently working on incorporating the angular distribution using theories of Molière,[33, 34] and Goudsmit and Saunderson,[32] as well as the incorporation of electron energy loss straggling theories such as that of Landau[149] into their moments method to increase the accuracy of their algorithm with experiment.

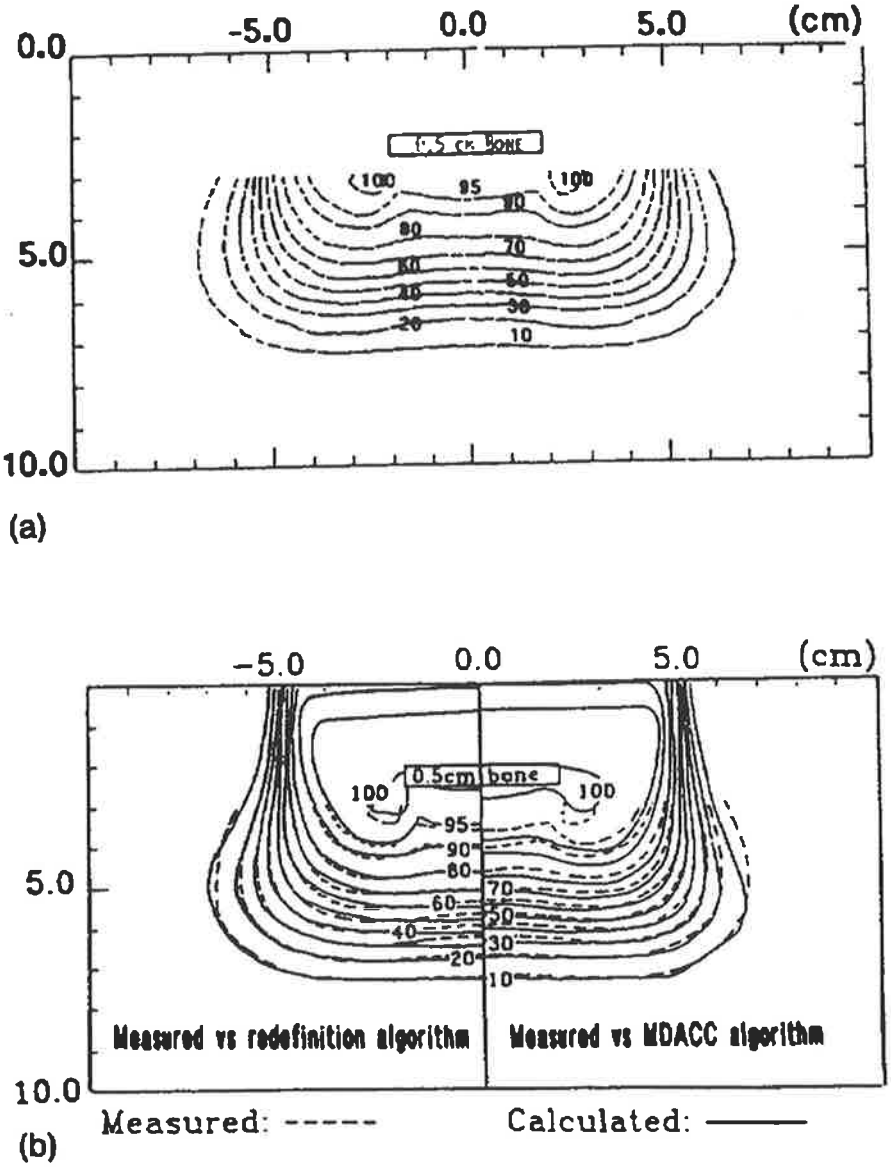

Figure 2.9: **The dose distribution beneath a 0.5 cm thick bone at 2.0 cm depth of water situated in the centre of a 10×10 cm^2 field, 15 MeV electrons, 100 cm SSD; (a) measured data; (b) measured vs pencil beam redefinition calculated data (left) and measured vs MDACC pencil beam calculations (right). Figure from Shiu and Hogstrom.[122]**

Computation time

McLellan *et al.*[36] reported calculation times of 30 minutes on a DEC LSI for a 10×10 cm^2 10 MeV electron beam.

2.3.6 The Multi-ray model

Introduction

The pencil beam method can be improved by calculating the mean path of electrons of a single pencil beam from the surface to the calculation point, and then assuming that the different materials along the path are infinite in their lateral extent for the purposes of determining the dose from that pencil beam.[123, 124] However, the root-mean-square width of the pencil beam distributions is up to a few centimetres at depth in water, so that the anatomical approximation becomes less valid for inhomogeneities with lateral discontinuities and for those that are thick or substantially deep relative to the surface.[121] Furthermore, the computation time for calculating the mean free path of electrons for each pencil beam makes such an algorithm impractical for clinical use.[122]

Method

The multi-ray model[124] was designed to overcome the slab approximation of the pencil beam method. For each point in the medium the most probable (mean) electron path traversed by electrons reaching that point, and the mean deflection angle at that point from the origin of each pencil beam is derived using FE theory. The electrons entering each layer in the medium are considered as a collection of mini-pencils, whose mean path and deflection angle are calculated as above, and new pencil beams (with energy

loss along each path length accounted for) are initiated from each mini-pencil. Hence the Gaussian distribution (given by standard FE electron transport) at each layer becomes skewed because of the obliquity of the mini-pencils, resulting in a non-Gaussian distribution. The concept of mean paths was first introduced by Perry and Holt.[123]

Results

Figure 2.10 (from Yu *et al.*[124]) shows pencil beam planar fluence distributions for a water phantom containing an aluminium inhomogeneity on the pencil beam axis calculated by the multi-ray model and a Monte Carlo simulation. The multi-ray model provides better agreement with Monte Carlo simulations than would be possible using the conventional pencil beam approximation due to improved calculation of lateral scattering components and the inclusion of the effects of finite inhomogeneities in the calculation of dose.

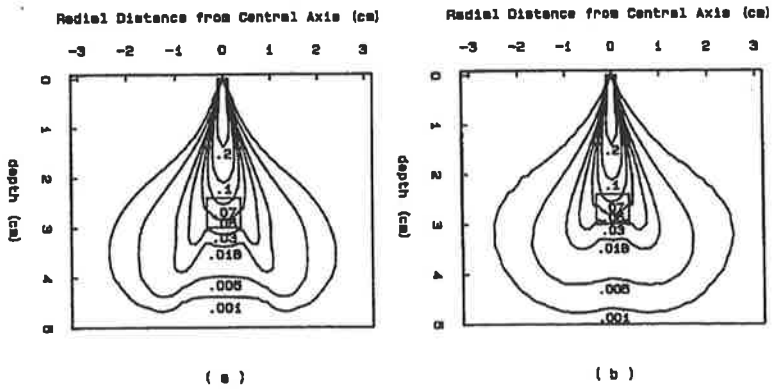

Figure 2.10: **Pencil beam planar fluence distributions for a water phantom containing an aluminium inhomogeneity on the pencil beam axis calculated by (a) the multi-ray model and (b) a modified Monte Carlo simulation which does not include δ-ray or bremsstrahlung production. Figure courtesy Yu *et al.*[124]**

The multi-ray model is more consistent with Monte Carlo (and more computationally expensive) than standard FE theory. However it still uses FE theory to calculate the mean paths, so intrinsically excludes large angle scattering. This exclusion results in

disagreement with Monte Carlo at shallow depths. Disagreement is also found at depth due to the neglect of energy straggling. The model does not account for the effects of δ-rays or bremsstrahlung photons.

Computation time

Yu *et al.*[124] give timings for a single pencil beam of 6 hours on a VAX 8600 for a three dimensional heterogeneous medium. Realistic broad beam geometries will take longer.

2.3.7 Perturbative theoretical methods

In a series of articles from 1983-1995[37, 125, 126, 127, 128, 129, 130, 131] David Jette has applied physically rigorous (and mathematically complex) analytical electron transport theory to the problem of electron beam dose calculation.

In references [125], [126] and [127], a second order multiple scattering term has been incorporated into the electron transport calculation based on a higher order solution to the Fermi-Eyges transport equation. This inclusion increases agreement with Monte Carlo angular distribution results.

In later papers, the limitation of the semi-infinite slab approximation[143] is overcome by solving the FE equation (only valid for horizontally layered media) for arbitrary variation in the composition of the material in the transverse directions by perturbation theory, allowing local inhomogeneities to be handled correctly.[129, 130] This perturbation series converges rapidly enough that only its first 2-3 terms need be considered for accurate dose calculations.

In Jette's most recent work,[131] large angle single scattering events have been added

to the method of dose calculation. These single scattering events complement the FE multiple scattering theory which does not include large angle scattering. The new theory shows less discrepancy with Monte Carlo data than the previous method.

Figure 2.11 (from Jette and Walker[130]) shows the relative primary dose at a depth of 1.75 cm below the edge of a bone slab as calculated by Monte Carlo, Jette theory and the Hogstrom algorithm. Jette theory is much better at predicting the hot and cold spots than the Hogstrom algorithm.

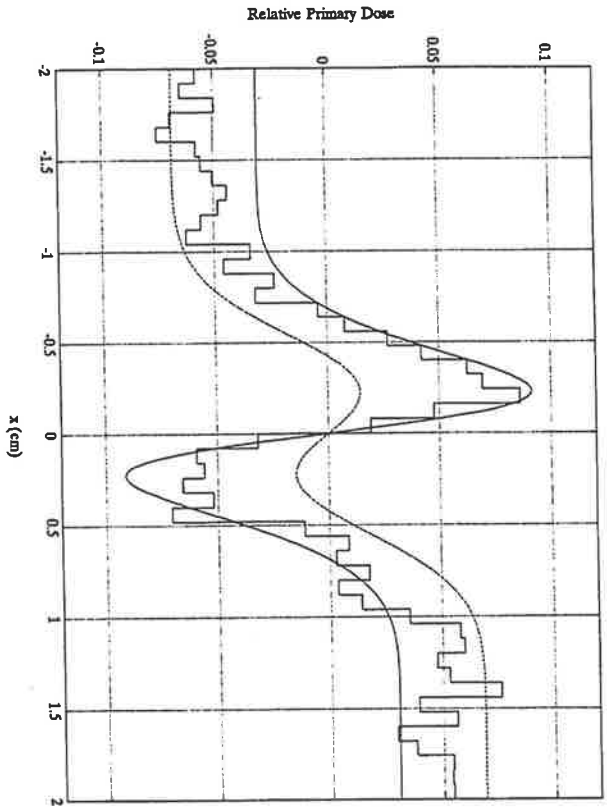

Figure 2.11: **The relative primary dose at a depth of 1.75 cm below a bone half slab as calculated by Monte Carlo (steps), Jette's perturbation theory (solid line) and the Hogstrom algorithm (dashed line). Figure courtesy Jette and Walker.[130]**

Future work will include the incorporation of range straggling and the redistribution of beam energy through δ-rays and bremsstrahlung photons.

No computation times are given for this work.

2.3.8 The Phase Space Evolution model

Introduction

The phase space of a beam consists of a six component array (x, y, z positions and momentum components, or alternatively x, y, z positions, polar and azimuthal angles and energy) of all of the particles of the beam.

The phase space evolution (PSE) model[132, 133, 134] is an extension of the phase space time evolution model of Cordaro and Zucker.[150] The dose distribution is calculated by a numerical transport method that utilises the interactions of radiation with matter. PSE is a full 3-D model for dose calculations in arbitrarily composed heterogeneous media irradiated with arbitrary electron beams. The model also yields energy and direction spectra of electrons at any position inside the irradiated medium.

The PSE model accounts for energy loss of primaries, secondary electron production, bremsstrahlung production, scattering, propagation in space and straggling. These processes are not independent, however partial grouping of interactions (as used in some Monte Carlo simulations) has been shown to yield good results.[146] The model assumes that motion, energy loss and scattering occur independently and successively within each of a series of time intervals, Δt, through which the model progresses.

Method

PSE models are used to simulate the evolution of the state of an object. In the case

of electron beam radiotherapy, the object is a phantom or patient, which is irradiated during a short period (eg 1 min) with a high energy electron beam. The resulting energy deposited in the absorbing medium is usually the desired information. The initial state of the phantom is defined by the positions, the kinetic energies and the directions (initial phase space) of all electrons applied in the treatment. Interactions between electrons and the patient alter this situation, and the initial condition of the phantom evolves via a sequence of non-empty states to the final empty state. The empty state indicates the end of the evolution, where all electrons propagating through the phantom have lost their kinetic energy (stopped) or exited the phantom.

The phase space is the form of a combination of discrete positions, energies and directions (P_i, E_j, Ω_k), called phase space elements (phasels). The content of each phasel is the number of electrons in each position-energy-direction node. The model simulates the transport of electrons that belong to the same phasel by redistribution of the content of that phasel over all other phasels. The redistribution of the contents of a number of phasels results in the evolution of the phase space to another state. The highest energy phasel is always redistributed so that phasel cannot be repopulated in subsequent steps. If a lower energy phasel was redistributed, it may be repopulated and the calculation for that phasel would have to be repeated.

The physics for the model are based on the physical processes of motion, energy loss and scattering. The distribution functions used for these processes are described in reference [132]. The phasel is redistributed according to the product of the three distribution functions of these processes.

The PSE method requires the phase space of the electron beam as input.

Results

Figure 2.12 (courtesy Korevaar *et al.*[53]) shows the dose distribution resulting from a 21 MeV beam normally incident on a heterogeneous water phantom, as calculated by the PSE method and Monte Carlo, showing close agreement between the two methods.

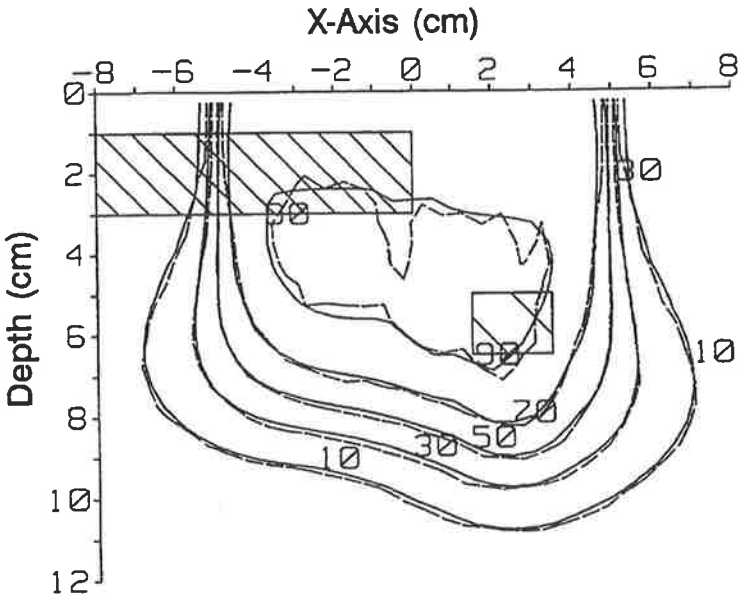

Figure 2.12: **The dose distribution resulting from a 21 MeV beam normally incident on a heterogeneous phantom, as calculated by the PSE method (solid lines) and Monte Carlo (dashed lines). The marked areas have densities of 1.5 and 0.4 g cm^{-3}. Figure courtesy Korevaar *et al.*[53]**

Computation time

The dose distribution for a 5×5 cm^2 20 MeV electron beam takes approximately 15 minutes to compute on a HP 9000/725/75 (6 hours on a VAX 11/780), a factor of 10 reduction over Monte Carlo calculation time.

2.3.9 The Monte Carlo method

The Monte Carlo method described for photon beams (refer section 2.2.4) can be similarly applied to electron beam dose calculation. Knowledge of the incident electron energy and angular spectra (and the spectra of contaminant photons) as well as the patient density is needed for the simulation. Monte Carlo is an excellent tool for testing other dose calculation algorithms due to its high accuracy, however the necessary computation time renders Monte Carlo impractical for routine clinical use.

2.3.10 The Superposition/Convolution method

Introduction

The superposition/convolution dose calculation method for electron beams[135, 136, 137] is similar to that for photon beams (as outlined in section 2.2.5). Monte Carlo-generated electron point beam energy deposition kernels are convolved with the relative fluence distribution (cf. terma in photon beam superposition) to obtain the dose distribution.

Method

If the incident energy and angular spectra of the electron beam at the patient plane is known then energy deposition kernels can be generated. These kernels can be calculated using analytical or Monte Carlo methods, though a Monte Carlo method is preferable as much better agreement with experiment is obtained, and the increased computation time required to generate the kernels is only needed once. The kernels are generated by initiating a point beam on the surface of a homogeneous media (generally water), and scoring the subsequently deposited energy throughout the volume. To account for

initial angular and energy spectra these distributions can be randomly sampled from the desired distribution. An isodose plot of a Monte Carlo generated 15 MeV electron kernel (point beam) in water is shown in figure 2.13.

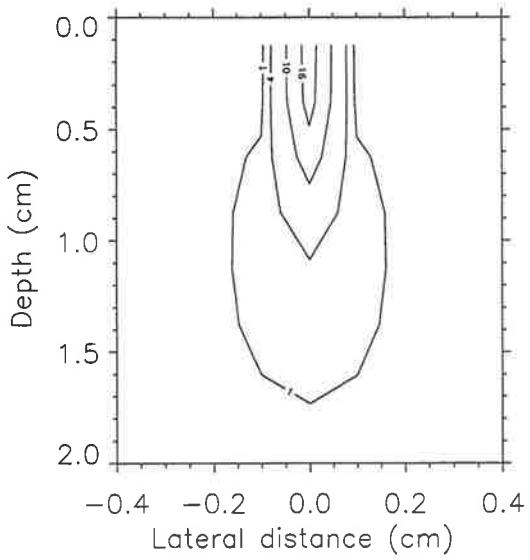

Figure 2.13: **An isodose plot of a Monte Carlo generated 15 MeV electron kernel (point beam) in water, in units of pGy MeV^{-1} cm^2. In electron superposition calculations, the kernels are convolved across the beam to obtain the dose distribution.**

If the energy and angular spectra are assumed constant across the beam [with varying beam weight $\phi(x', y')$], then the dose distribution $D(x, y, z)$ in the media is calculated by the convolution

$$D(x, y, z) = \int\int_{field} \phi(x', y') H(x - x', y - y', z, \rho_{ave}) / \rho_{ave} dy dx, \qquad (2.15)$$

where $H(x - x', y - y', z, \rho_{ave})$ is the energy deposition kernel value for a density ρ_{ave} [the average density between the surface position of the electron kernel (x', y') and the dose calculation point (x, y, z)].

The ρ_{ave} term in equation 2.15 is found by ray-tracing from the interaction site of the electrons to the dose deposition point. By only calculating an average density, this

density scaling method ignores the density distribution between these two points. Woo and Cunningham[95] showed that this density scaling (known as the rectilinear scaling) leads to an over-estimation in dose in a layer beyond a high to low density interface, and that there is a corresponding under-estimate beyond a low to high density interface. Using rectilinear density scaling for electron beam convolution introduces larger errors than when it is used for X-ray beam convolution[151] (refer section 2.2.5).

Results

Figure 2.14 (from Mackie[135]) shows a comparison between superposition depth dose calculations and Monte Carlo calculations for a cylindrical air cavity. The superposition calculation greatly underestimates the dose behind the cavity when the cavity is near the surface, and overestimates the dose when the cavity is located at deeper depths.

In its current form, Mackie[135] concluded that the convolution approach may be used as a tool to determine the energy and angular distribution of electrons incident on a phantom. However, as a dose calculation algorithm, the method does not account properly for the enhanced scatter into low density regions, or the decreased scatter out of these regions.

Computation time

Altschuler *et al.*[137] give a computation time for this method of 15 minutes on a VAX 11/780 for a 12 MeV 10×10 cm^2 field with 3 mm resolution.

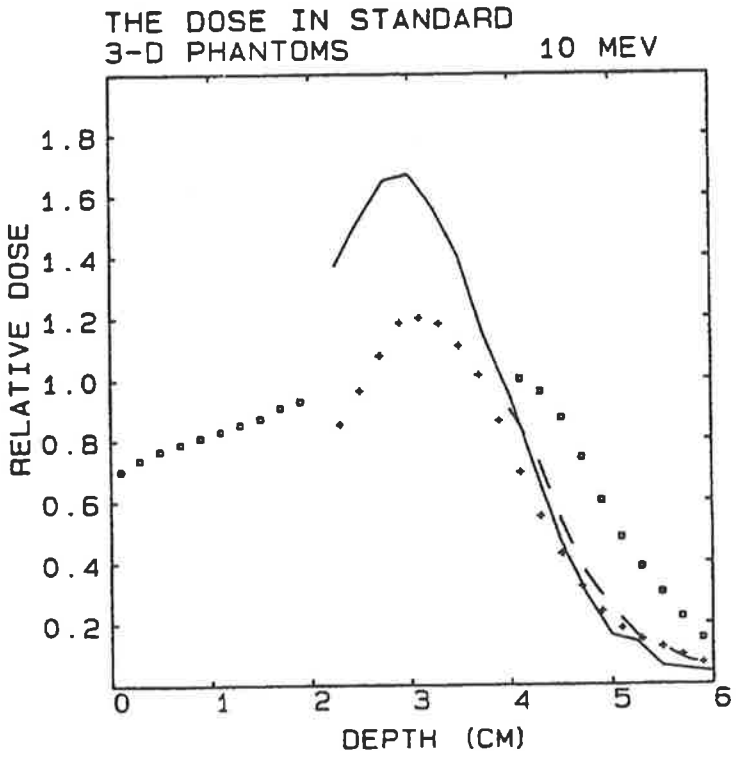

Figure 2.14: **Comparisons between superposition calculations and EGS Monte Carlo modelling for phantoms containing a 3-dimensional 1 cm diameter air cylinder. The solid line and the plusses are the Monte Carlo and the superposition doses respectively for the cylinder extending between 0.2 and 2.2 cm. The dashed line (Monte Carlo) and the box (superposition) are the calculations for the cylinder between 2.0 and 4.0 cm. Figure from Mackie.[135]**

2.3.11 The Macro-Monte Carlo algorithm

Introduction

The Macro Monte Carlo (MMC) code[138, 139] was developed to increase the speed of full Monte Carlo electron transport calculations without loss in accuracy. Originally proposed by Mackie and Battista[152] to simplify, condense and accelerate 'traditional' Monte Carlo calculations, instead of a detailed microscopic simulation of an electron track,[4] the electron is transported in large macroscopic steps through the absorbing medium. The transport parameters of each step are sampled from pre-calculated probability distributions. This simplification drastically reduces Monte Carlo calculation times after the initial 'once for all' probability distributions have been determined.

Method

Traditional Monte Carlo methods are used to simulate electron transport through spheres (kugels) of 0.05 to 0.3 cm radii composed of air, water, lung and bone analogue (LN4 and SB3 respectively[153]) for discrete incident electron energies between 0.2 and 20 MeV. The resulting distributions of position, direction and energy of the electrons serve as a database for the MMC calculations. MMC transport of one electron track is shown in figure 2.15 (from Neuenschwander and Born[138]), where the electron is transported in large scale steps through the absorber.

The pre-calculations were performed using EGS4 to simulate the transport of vertically incident electrons through the kugels. For each kugel size a complete set of parameters can thus be denoted by a pair of indices (j, k) where j represents the material index and k the incident energy T_i^k, of the primary electron. The eight quantities needed as a

[4] On a small scale EGS and ETRAN can be considered to be macroscopic as they group several electron interactions into one multiple scattering step.

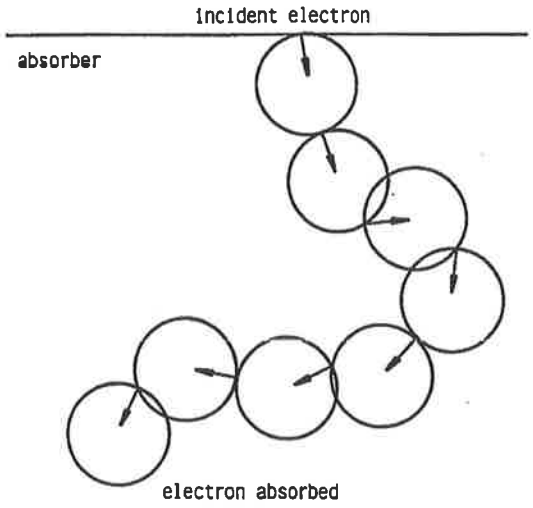

Figure 2.15: **Schematic illustration of the MMC algorithm. Arrows indicate the direction of motion of the electron incident on the MMC kugels. Figure courtesy Neuenschwander and Born.[138]**

database for subsequent MMC electron transport are:

(i) a cumulative density function of the scattering angle θ_f and angle α of emergent primary electrons [refer figure 2.16 (from Neuenschwander and Born[138])],

(ii) a cumulative density function of the energy T_f of emerging primary electrons.

(iii) a probability of absorption of the primary electron,

(iv) the relative amounts of energy deposited in the kugel, or released as secondary electron and bremsstrahlung energy leaving the kugel,

(v) a cumulative density function of continuous slowing down approximation ranges of emergent secondary electrons, based on CSDA ranges tabulated in ICRU 35,[25] for $T_i = 10$ MeV only,

(vi) the scaling factors for the above 10 MeV distribution which can be used as an approximation for the distribution for other incident energies,

(vii) the mean energy absorption coefficients of emerging photons, based on data tabulated by Johns and Cunningham,[11] and

(viii) the CSDA ranges of incident electrons, taken from ICRU 35.[25]

Using the above distributions and knowledge of the incident energy, direction and po-

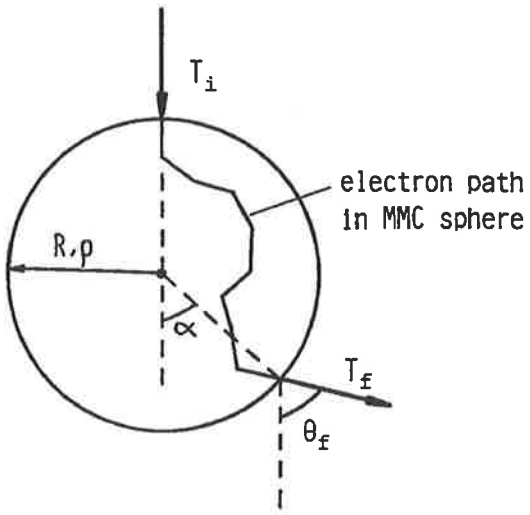

Figure 2.16: **Geometry for the preliminary calculations in MMC. Figure courtesy Neuenschwander and Born.[138]**

sition parameters T_i, θ_i, ϕ_i and $\mathbf{r_i}$ respectively, each electron is transported through a kugel. Hence the exit energy, scattering angle, azimuthal angle and emergent angle parameters T_f, θ_f, ϕ_f and α respectively are calculated (refer figure 2.16), from which the position $\mathbf{r_{out}}$ and direction $\mathbf{\Omega_{out}}$ of the primary particle is determined. The energy deposited by the primary electron and any secondary electrons or bremsstrahlung photons is scored in the dose matrix (the total energy transferred in each step is $T_i - T_f$).

Secondary electrons, and photons produced in a sphere are both transported in the direction $\mathbf{\Omega_{out}}$. The energy of the secondary electron is deposited over its CSDA range. The energy of the bremsstrahlung photon is all deposited at the photon interaction site, at a distance from the kugel calculated by sampling the mean free path function. Positrons are transported as electrons.

Results

Figure 2.17 (from Neuenschwander *et al.*[139]) shows the central axis depth dose curve for a 10 MeV 5×3 cm^2 electron beam incident on a 'head' phantom, as calculated by MMC and EGS4. Good agreement is shown between the MMC and EGS4 dose distributions in this complex geometry.

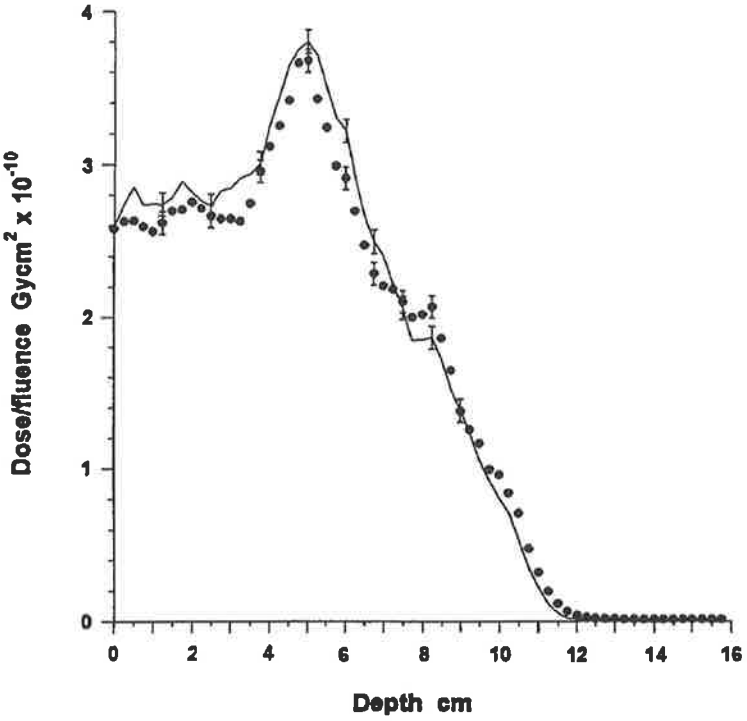

Figure 2.17: **The central axis depth dose curve for a 10 MeV 5×3 cm^2 electron beam incident on a 'head' phantom, as calculated by MMC (dots) and EGS4 (solid line). Figure courtesy Neuenschwander *et al.*[139]**

The original MMC code had fixed kugel sizes, which performed relatively poorly at high-low density interfaces. However, the new version uses kugels of varying size, enabling accurate transport across interfaces using small kugels, and large electron steps away from interfaces, thus reducing calculation time. Other changes include explicit boundary crossing: a new electron step is originated at each interface which reduces boundary crossing artefacts.

Computation time

To calculate a 10×10 cm^2 dose distribution with 0.25 cm^3 voxels in a bone slab phantom, 33 minutes are required on a DECstation 500/200.

2.3.12 The Voxel-based Monte Carlo method

The Voxel-based Monte Carlo method[110, 154, 155] (VMC) calculates dose from electron beams using a Monte Carlo method which makes several approximations and simplifications in the description of electron transport processes compared to more rigorous Monte Carlo methods such as EGS4 (refer section 2.2.4).

Some of the simplifications used in VMC are:

(i) the multiple scattering angle is calculated from an analytical distribution,

(ii) the total number of electron steps per electron history is significantly reduced as compared to conventional Monte Carlo methods,

(iii) δ-ray production is described by a simplified Møller cross-section,

(iv) energy loss due to radiative collisions is calculated using a simplified differential bremsstrahlung cross-section,

(v) the photons created in radiative collisions are not explicitly transported,

(vi) a lateral and longitudinal correlation algorithm is used for small electron step transport instead of PRESTA, and

(vii) the same electron can be transported more than once from different entrance positions in the medium.

The simplifications described above increase the computational speed of VMC up to 35 times that of EGS4, without significant loss in accuracy. Dose distributions in a variety of heterogeneous phantoms show close agreement between VMC and EGS4, where a 2-D pencil beam algorithm has produced underpredications in dose of up to 40%.

2.4 Summary

In this chapter a variety of both electron and photon dose calculation algorithms were presented. These methods are based on varying physical principles and assumptions. The calculation times for the various techniques vary markedly, and are roughly proportional to the accuracy of the dose calculation algorithm. The most accurate dose calculation method, Monte Carlo (refer section 2.2.4), is still too computationally intensive to use as a routine clinical planning tool, and hence further algorithms need developing which are capable of calculating dose distributions with near Monte Carlo accuracy, but are significantly less computationally intensive. Attempts at designing such algorithms are outlined in the following chapters.

Chapter 3

Superposition Incorporating Fermi-Eyges Theory

3.1 Introduction

This chapter describes a method which accounts for the effects of the density distribution, and not just the average density, between the primary photon interaction and dose deposition sites in a superposition calculation. The aim of this work was to reduce the difference between the dose predicted using the superposition method, and the dose predicted in Monte Carlo simulations by incorporating electron scattering theory into the primary dose calculation of the superposition method.

The photon-electron cascade model of Yu *et al.*[156] is also discussed in this chapter. Like the Fermi-Eyges scaling superposition algorithm presented in this chapter, the cascade method uses Fermi-Eyges calculations for the primary dose calculation, and standard

superposition for the scatter dose calculation.

3.1.1 Fermi-Eyges electron scattering theory

In order to account for electron transport between the photon interaction and energy deposition sites, electron scattering theory was used. The scattering theory used in this calculation is Fermi-Eyges (FE) multiple Coulomb scattering theory[10] (refer section 1.4.3). A limitation of FE theory is that it only accounts for small-angle multiple Coulomb scattering, and hence large angle scattering is ignored (the assumption $\tan\theta = \theta$ is made when solving equation 1.27). However, use of a more rigorous electron transport method, such as Molière or Goudsmit-Saunderson theory, would render the convolution calculation prohibitively time consuming.

3.1.2 The Photon-Electron Cascade model

Similar to FE scaling convolution is the photon-electron cascade model, proposed by Yu *et al.*[156] The cascade method was also designed to overcome the limitations of the superposition algorithm at interfaces of different density, and in different atomic number materials. In the cascade model, the primary photon beam is considered as a source of many electron pencil beams. Each pencil beam is transported through the absorbing medium from the photon interaction site using FE theory. Electrons in each pencil beam are grouped according to their kinetic energy. Each energy component is transported as a separate monoenergetic beam.

The four-stage process to calculate dose involves (i) determining the primary photon fluence incident to every layer of the medium, (ii) calculating the electron distribution exiting the given layer from the photon fluence, (iii) transporting the electrons to the

downstream layers to obtain the planar fluence distribution which is converted to dose, and (iv) summing the dose contributions from each pencil beam to obtain the primary dose component (the scatter dose array is calculated using a standard superposition procedure).

Because the electrons set in motion at the interaction site have an initial angular distribution, the initial scattering moments of each pencil beam need to be calculated. These scattering moments were obtained from Monte Carlo generated distributions. Electron backscatter is accounted for by using an analytic function.

FE theory can be used to transport electrons through an absorbing medium of arbitrary components, as long as the scattering power of each component is known. Hence the cascade model can account for an absorbing medium of arbitrary density and composition. Cascade model dose distributions show close agreement with Monte Carlo generated results (and improvement over the superposition method) for a phantom containing an aluminium heterogeneity.

A limitation of this technique is the required computation time: 12 hours on a VAX 8650 for a 10×10 cm^2 field with 12 energy bins and 0.1×0.1×0.25 cm^3 voxel resolution.

3.2 Method

3.2.1 The Fermi-Eyges theory scaling method

From the *interaction point of view*[86] and in a Cartesian system, equation 2.8 can be rewritten as the dose deposited in voxel i, j, k due to interactions in voxel i', j', k',

$$D(i,j,k;i',j',k') = \Sigma_{k'}\Sigma_{j'}\Sigma_{i'}\frac{T_{i',j',k'}\rho_{i',j',k'}H(\rho_{ave}, i-i', j-j', k-k')}{\rho_{ave}}. \qquad (3.1)$$

In superposition with rectilinear scaling, ρ_{ave} is the average density between interaction and deposition sites, which in the case of the infinite slab medium[1] is the average density between the centre of layers k and k'. The approach used in this work was to modify ρ_{ave} by the calculated lateral standard deviation of a pencil beam of electrons after travelling from i',j',k' to i',j',k, to obtain a kernel value $\hat{H}(\widehat{\rho_{ave}}, i-i', j-j', \widehat{k-k'})$, where the lateral standard deviation is calculated for the actual density distribution, and also for a homogeneous medium of density ρ_{ave}.

In finding the energy deposited in a layer k due to interactions in voxel i',j',k', the lateral electron standard deviation, $\sigma_{x,inhom}$, (that for the density *distribution* between i',j',k' and i',j',k) is needed. Also needed is the energy loss for the effective distance $(k-k')\Delta z\rho_{ave}$. There is a standard deviation, $\sigma_{x,hom}$, in layer k, which is $k-k'$ layers [distance $(k-k')\Delta z$] from the interaction site in a kernel of density ρ_{ave}. By O'Connors theorem,[57] the standard deviation will be $\sigma_{x,inhom}$ at a distance $(k-k')\Delta z\sigma_{x,inhom}/\sigma_{x,hom}$ from the interaction site in a kernel of density $\rho_{ave}\sigma_{x,hom}/\sigma_{x,inhom}$. Note that the effective distance is still $(k-k')\Delta z\rho_{ave}$, so the total energy deposited in layer k will be the same, however the distribution of energy deposition in this layer will change.

For each voxel layer in the z-direction from the interaction site, the standard deviation of the lateral spread of the electrons, $\sigma_{x,hom}$, is calculated using FE theory by assuming a homogeneous density distribution between the interaction and deposition site (as in rectilinear scaling). The standard deviation is then recalculated using FE theory by taking account of the density distribution between the interaction and deposition site, to obtain $\sigma_{x,inhom}$, (note in this implementation, the density is traced in the z-direction

[1] A medium of slab inhomogeneities with interfaces only perpendicular to the incident beam direction, such as the lung phantom of figure 3.6.

only). The ratio, R, of $\sigma_{x,hom}$ to $\sigma_{x,inhom}$ is then calculated. The subsequent kernel value for each layer is taken from a kernel of density equal to the average density multiplied by R, with a z-value equal to the original z-value divided by R. This technique is shown schematically in figure 3.1.

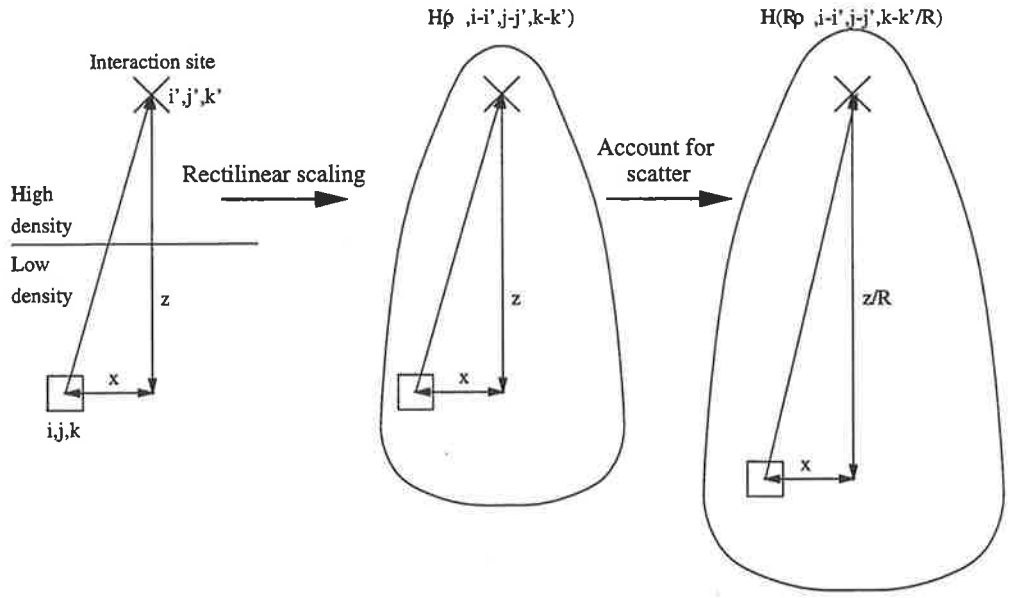

Figure 3.1: **Schematic diagram showing the kernel scaling method where electron scattering is accounted for.**

Using FE scaling, the energy deposition at the layer of equal radiological depth in figure 2.6 would give a narrower distribution for the low to high density case, and a wider distribution for the high to low density case (with the same total dose deposition in that layer in both phantoms). Note that standard superposition would give the same dose distribution in this layer for both cases.

Thus the energy deposited at a physical depth z and lateral distance x from the site is changed, but the total dose deposited at this layer is the same as that of rectilinear scaling. Mathematically, $k\widehat{-}k'$ and $\widehat{\rho_{ave}}$ for the new kernel value $\hat{H}\left(i-i', j-j', k\widehat{-}k', \widehat{\rho_{ave}}\right)$ is found from

$$k\widehat{-}k' = (k-k') \times \frac{\sigma_{x,inhom}}{\sigma_{x,hom}} = \frac{k-k'}{R} \tag{3.2}$$

and

$$\widehat{\rho_{ave}} = \rho_{ave} \times \frac{\sigma_{x,hom}}{\sigma_{x,inhom}} = \rho_{ave} \times R. \tag{3.3}$$

In order to minimise computation time, the electron scattering power in the FE theory calculations was assumed to be constant with energy. Also, in the FE theory there is assumed to be no initial angular electron spread at the interaction site. The two plots of figure 2.6 show that the ejected electrons are predominantly forward directed for 5 MeV incident photons in water. Any systematic error due to these assumptions will be minimised, as the ratio of the resulting homogeneous and inhomogeneous lateral standard deviation values is taken.

In rectilinear scaling, the kernel value is interpolated between two different densities at the same voxel layer. In FE theory scaling, the kernel value is found by an interpolation between kernel densities, and also between layers. If there is a large gradient of fractional energies between voxels in the kernel array, this could lead to sampling error. For this reason it was necessary to reduce the kernel density spacing from 0.2 g cm^{-3} (0.2,0.4,... density kernels) to 0.1 g cm^{-3} (0.2,0.3,0.4,... density kernels) to obtain smooth dose distributions.

The subject of this work was the scaling of the primary dose. To avoid any errors due to kernel tilting,[91] non-divergent fields were investigated.

A more detailed description of the code used for FE scaling calculations is found in appendix A.

3.2.2 Superposition calculations

Polyenergetic primary and scatter energy deposition kernels were generated using the EGS4 Monte Carlo code[8] for densities from 0.2 g cm^{-3} to 1.9 g cm^{-3}, in increments of 0.1 g cm^{-3} for both primary and scatter dose at 6 MV, 10 MV and 18 MV photon beam energies. In forming the kernels 5×10^6 photons were forced to interact at a point 2.25 cm deep in a Cartesian array ($0.5\times0.5\times0.5$ cm^3 voxels). Energy imparted and deposited due to each incident photon was weighted by the attenuation coefficient of that photon.[44] The spectra of the 6 MV and 18 MV beams were found from Ahnesjö *et al.*,[82] and the 10 MV spectrum from Mohan *et al.*[43]

3.2.3 Monte Carlo calculations

The EGS4 Monte Carlo code[8] was used with PRESTA.[157] AE was set to 0.521 MeV, AP to 0.01 MeV, ECUT to 0.561 MeV and PCUT to 0.05 MeV. Incident photons of energies 6 MV, 10 MV and 18 MV were transported through the kernel geometries and the water-lung-water phantom described below. The subsequent energy deposited was recorded in a Cartesian array of $0.5\times0.5\times0.5$ cm^3 voxels. At least 10^8 incident photons were used for each broad beam simulation, and the 4-fold symmetry of the phantom was used to reduce the statistical variance by 4.

3.2.4 Phantoms

The dose distribution of monodirectional (infinite SSD) incident photons of energies 6 MV, 10 MV and 18 MV were calculated using the superposition technique employing both rectilinear scaling and FE scaling, and also by Monte Carlo, for single interaction sites in slab phantoms with both high to low density and low to high density interfaces

as shown in figure 3.2. These algorithms were also tested using broad beams in a water-lung-water slab phantom consisting of 4 cm of water, 8 cm of density 0.3 g cm^{-3} lung (of water equivalent material) and 8 cm of water, shown in figure 3.3.

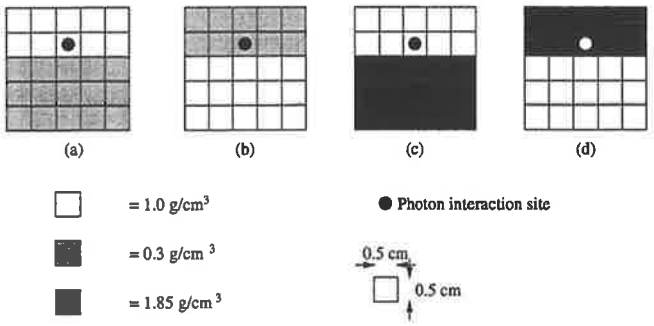

Figure 3.2: **A schematic diagram of the phantoms used to test the FE scaling superposition algorithm for photons forced to interact at a point.**

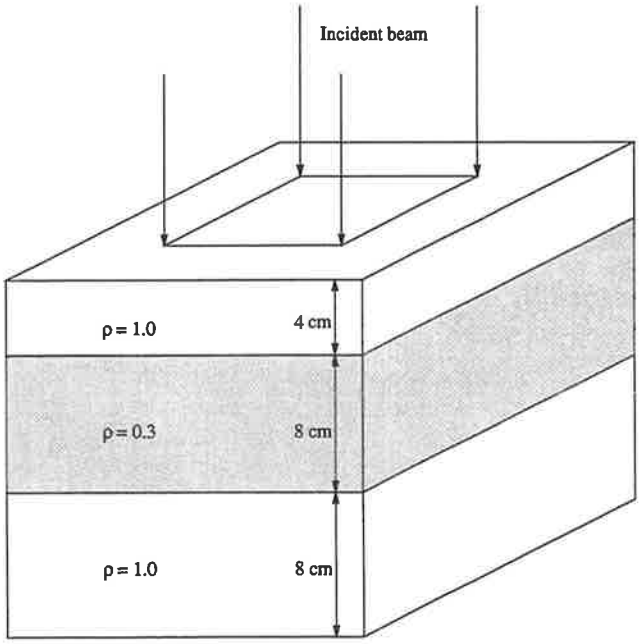

Figure 3.3: **A schematic diagram of the phantom used to test the FE scaling superposition algorithm for broad beams.**

3.3 Results

3.3.1 Single interaction site results

Before testing the FE scaling method in a full convolution calculation, primary energy deposition kernels were generated in a variety of heterogeneous slab geometries consisting of layers of water-equivalent material of different density (as shown in figure 3.2) by convolving energy deposition kernels at a single photon interaction site. Both FE scaling and rectilinear scaling convolution methods were used. This method is similar to that described by Mackie,[85] where dose spread arrays generated in heterogeneous phantoms from the Monte Carlo method were compared to the calculated dose spread arrays for the same heterogeneous phantoms. The method is equivalent to calculating a dose distribution where there is only one voxel with non-zero terma.

The energy deposition kernels calculated by both FE scaling and standard superposition methods were compared to kernels generated directly in the same heterogeneous geometries using Monte Carlo. This comparison was performed for 6 MV and 18 MV beams. The sum of the mean square energy difference in every voxel between the two scaling methods and Monte Carlo, is shown in table 3.1.

Table 3.1 shows that the FE scaling method gives kernels which have smaller mean square differences between Monte Carlo generated kernels in heterogeneous media than do rectilinearly scaled kernels. The FE method shows relatively better agreement with Monte Carlo as the incident beam energy is increased. This is due to the increased pathlength of electrons crossing the interface at high energies. Also, at higher energies the assumption that the electrons ejected at the interaction site have no angular spread becomes increasingly valid.

Figure 3.4 shows an absolute difference map between FE scaling and Monte Carlo, and

Table 3.1: **Normalised mean square energy deposition differences between FE scaled kernels and Monte Carlo kernels, and rectilinear scaled kernels and Monte Carlo kernels in media with slab inhomogeneities, summed over every voxel in the energy deposition arrays.**

Energy	Σ(FE - EGS4)^2	Σ(Rect. - EGS4)^2
6 MV	1.0	1.4
18 MV	1.0	2.6

rectilinear scaling and Monte Carlo, for an 18 MV primary energy deposition kernel generated in a high density (1.0 g cm^{-3}) to low density (0.3 g cm^{-3}) slab geometry. The interaction site is 0.75 cm above the high/low density interface. The FE scaled energy deposition kernel shows better agreement with Monte Carlo in both the lateral and longitudinal directions than the rectilinearly scaled kernel.

3.3.2 Depth dose results

The 10 MV and 18 MV depth dose curves in a water-lung-water phantom for 5×5 cm^2 and 10×10 cm^2 fields are shown in figure 3.5 and figure 3.6 respectively. These figures show that FE scaling superposition improves agreement with Monte Carlo at 10 MV and 18 MV for the 5×5 cm^2 fields where lateral electronic equilibrium does not exist at the central axis. For the 18 MV, 5×5 cm^2 field, the maximum error in the depth dose curves between convolution and Monte Carlo is reduced from 5% to 2.5% if FE scaling is used, with a factor of 5 reduction in the mean square error over the whole curve. For the 10×10 cm^2 fields however, where lateral electronic disequilibrium is small, there is only a small difference between the two kernel scaling methods, except at the secondary build-up region in the second water region, which FE scaling predicts the dose better than rectilinear scaling. Negligible difference was observed for 5×5 cm^2 or 10×10 cm^2 field sizes for the 6 MV beam. For figures 3.5 and 3.6 the uncertainty in the Monte Carlo data was 1% for the 5×5 cm^2 field, and 2% for the 10×10 cm^2 field. All three methods used voxel sizes of 0.5×0.5×0.5 cm^3.

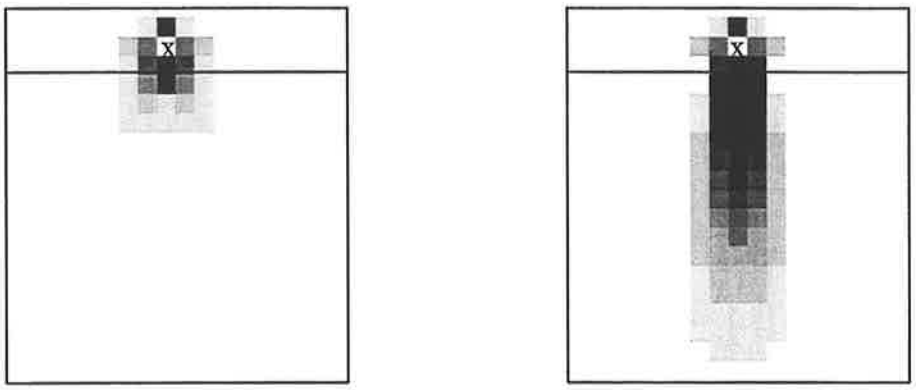

Figure 3.4: **Absolute difference map between FE scaled energy deposition kernels and Monte Carlo energy deposition kernels (left), and rectilinear scaled kernels and Monte Carlo (right). The solid line is the high (1.0 g cm^{-3}) to low (0.3 g cm^{-3}) density interface, and 'x' indicates the interaction voxel. The darker the colour, the larger the difference between the superposition and Monte Carlo results.**

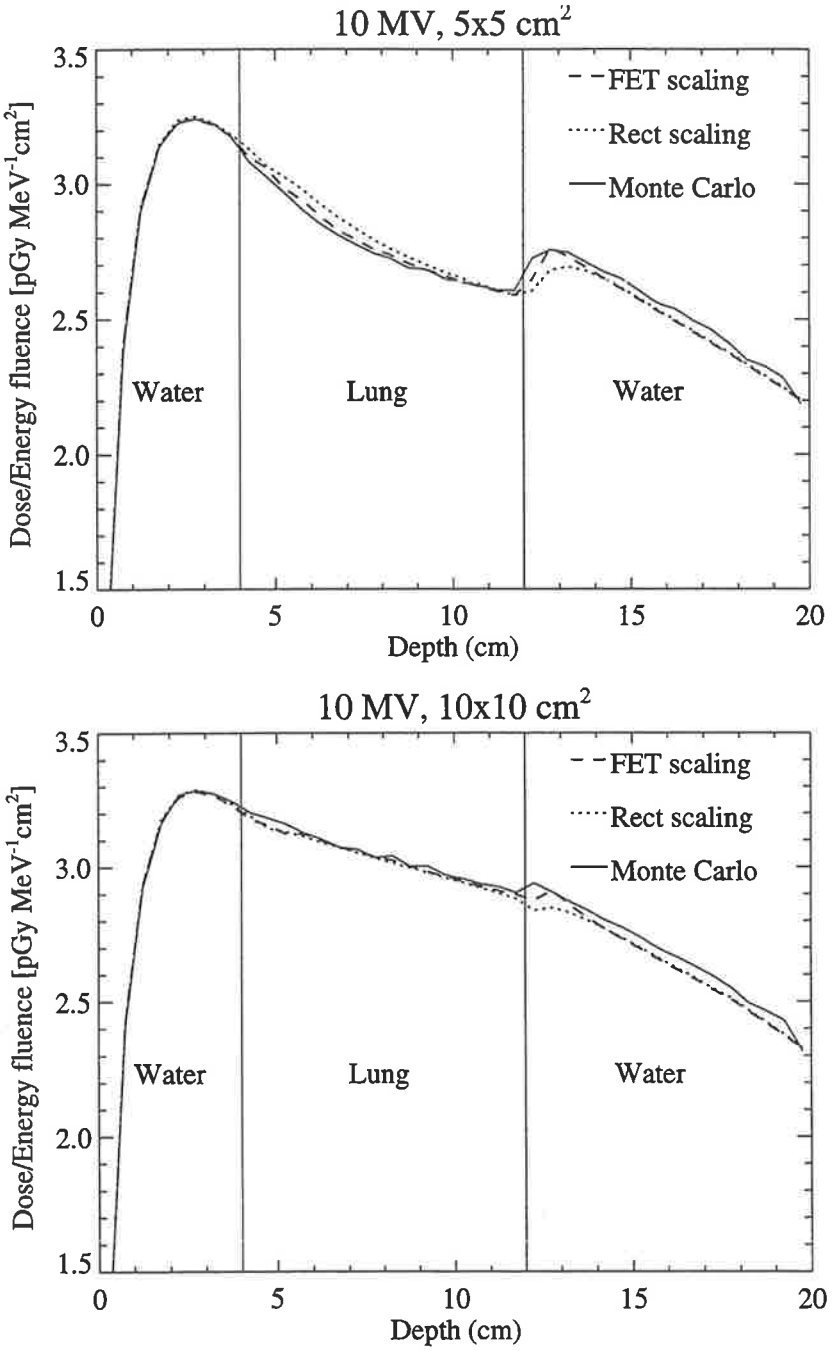

Figure 3.5: **Depth dose curves for a 5×5 cm², 10 MV beam (top), and a 10×10 cm², 10 MV beam (bottom). Results of Monte Carlo (solid line), rectilinear scaling convolution (dotted lines) and FE scaling convolution (dashed lines) are shown.**

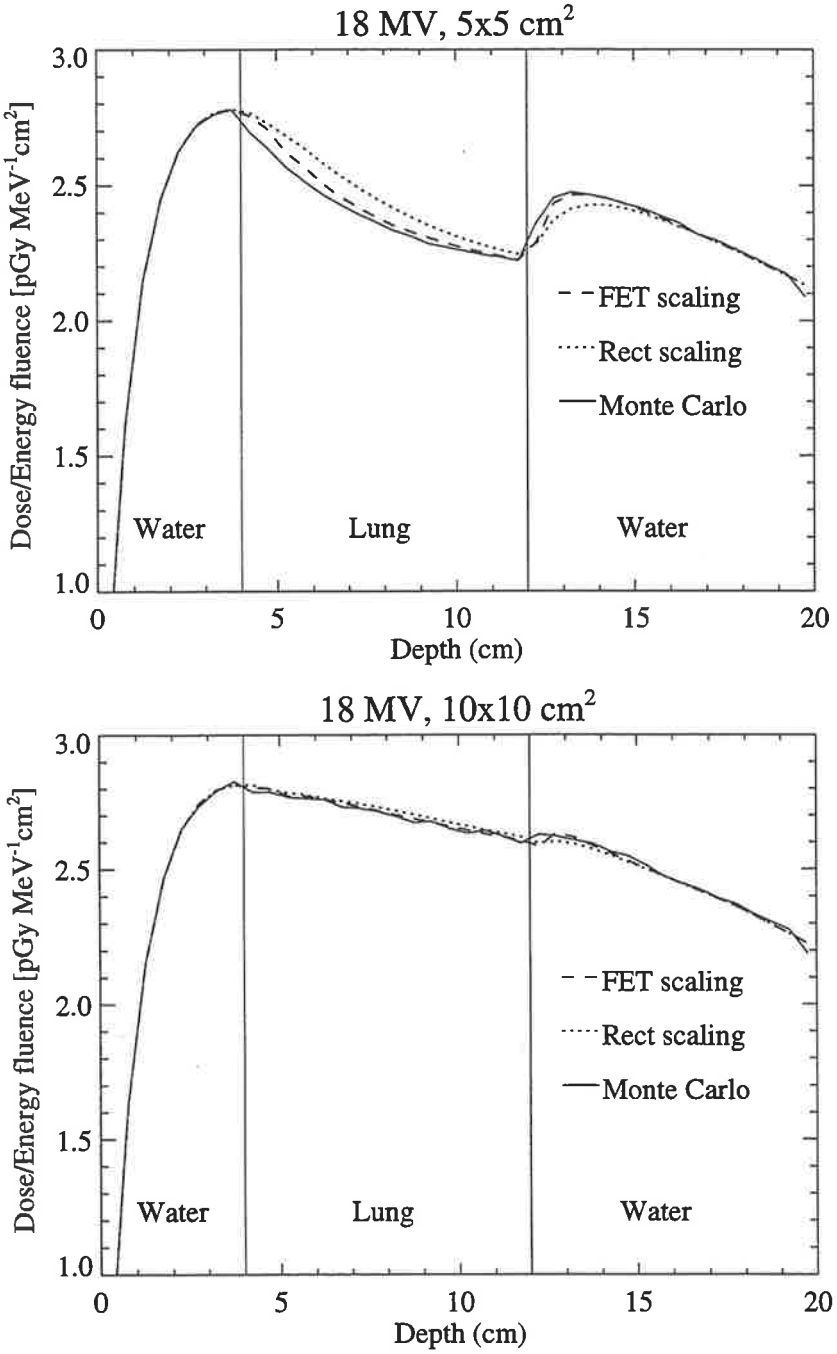

Figure 3.6: **Depth dose curves for a 5×5 cm², 18 MV beam (top), and a 10×10 cm², 18 MV beam (bottom). Results of Monte Carlo (solid line), rectilinear scaling convolution (dotted lines) and FE scaling convolution (dashed lines) are shown.**

3.3.3 Dose profile results

An 18 MV dose profile at mid-lung (8 cm deep) for the lung phantom of figure 3.3 is shown in figure 3.7, where the results of Monte Carlo and the two scaling methods are compared. The penumbra predicted by rectilinear scaling is sharper than that obtained in the Monte Carlo simulation, whereas better agreement is obtained with FE scaling. As shown previously, the central axis dose is in better agreement using FE scaling. The broadening of the penumbra, and lower central axis dose obtained by FE scaling (as opposed to rectilinear scaling), is due to the increased lateral spread of energy predicted for electrons ejected from interaction sites above the water-lung interface.

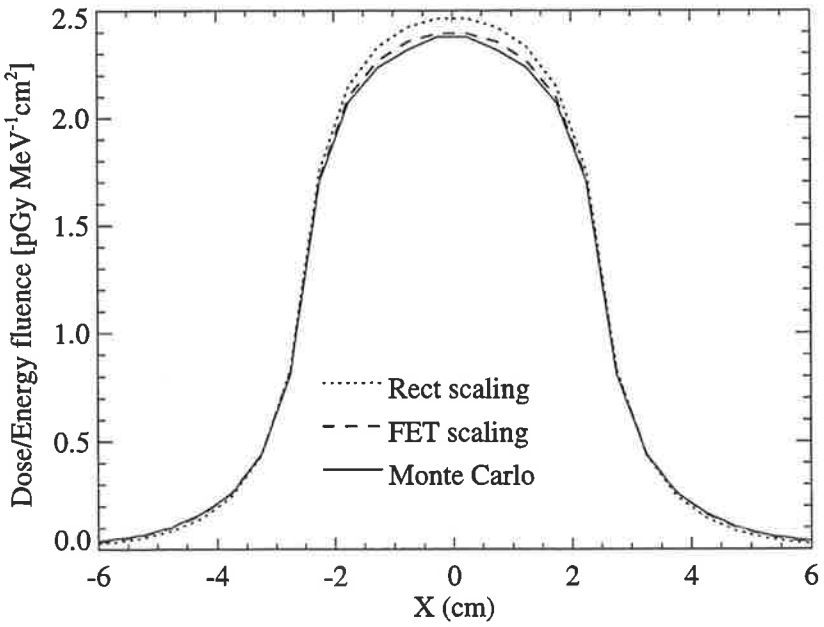

Figure 3.7: **Dose profile curves for a 5×5 cm^2 18 MV beam at 8 cm deep in a lung phantom (mid-lung). Results of Monte Carlo (solid line), rectilinear scaling convolution (dotted line) and FE scaling convolution (dashed line) are compared.**

3.3.4 Computation time

For the 5×5 cm^2 10 MV beam the time taken for the primary dose calculation using rectilinear scaling was 25 seconds on a DECalpha platform, while that for FE scaling was 75 seconds. The scatter dose in both cases took 150 seconds. The use of FE scaling to obtain the primary dose distribution takes approximately 3 times longer to compute than that of rectilinear scaling.

3.4 Conclusion

A method of calculating the primary dose component in a convolution calculation by invoking FE electron scattering theory along with rectilinear scaling has been described. Energy deposition kernels generated in slab geometries of varying density using FE scaling show closer agreement with Monte Carlo calculated energy deposition kernels than those generated using rectilinear scaling only.

Depth dose curves in a lung phantom (a geometry with a slab inhomogeneity of density 0.3 g cm^{-3}) produced using FE scaling superposition are more consistent with Monte Carlo generated depth dose curves than the curves produced using rectilinear scaling superposition for 5×5 cm^2 and 10×10 cm^2 fields at 10 MV and 18 MV beam energies. For a 5×5 cm^2 18 MV field, the maximum dose difference on central axis between FE scaling and convolution is 2.5%, whereas that for rectilinear scaling is 5%. For a 10×10 cm^2 field at 10 and 18 MV, and for 5×5 and 10×10 cm^2 fields at 6 MV, the difference between FE scaling and rectilinear scaling was smaller due to the decreased amount of electronic disequilibrium at the central axis.

The dose profile for a 5×5 cm^2, 18 MV beam calculated by FE scaling superposition shows better agreement with a Monte Carlo dose profile than that generated by rectilin-

ear scaling superposition, in both the central axis dose, and the penumbral shape.

The FE scaling method increases the calculation time for the primary dose by a factor of 3 in the geometries examined.

The FE scaling method assumes that there is no angular distribution of electrons set in motion about the beam axis. Use of non-zero initial scattering moments in FE theory as used by Yu *et al.*[156] may improve agreement with Monte Carlo.

Another limitation of the FE scaling method is that it only improves superposition with rectilinear scaling in the beam axis direction. A logical extension is to include FE scaling into a collapsed cone convolution method (refer section 2.2.6), where the energy in a cone can be redistributed between cones depending on the geometry of the medium the cones are passing through. The complexity of the algorithm as well as the calculation time will significantly increase for the more general case.

FE scaling superposition could also be extended to account for materials of non-waterlike composition.

Chapter 4

Super-Monte Carlo for X-ray Beam Planning

4.1 Introduction

The most accurate radiotherapy dose calculation methods currently available are Monte Carlo based techniques.[8, 9] However, these techniques are too computationally intensive to use in planning systems for routine clinical use with currently available hardware. The next most physically rigorous X-ray dose calculation technique is the superposition/convolution method.[83, 86, 90, 16] Superposition accounts for the range of electrons ejected by interactions of primary photons via the primary kernel, and attempts to correct for the effects of density variations by scaling the primary kernel. The problem with normal kernel scaling (known as rectilinear scaling) is that straight-line electron tracks are assumed, and these tracks are simply scaled by the density. No account is taken of the perturbation in the electron fluence which occurs due to changes in the lateral de-

flection caused by scattering.[88, 95] The error due to this limitation increases with X-ray energy as a result of increased electronic disequilibrium.[158]

A method for overcoming the density interface problem of superposition has been proposed in chapter 3 which extends the rectilinear density scaling method used in superposition calculations to include a factor based on the Fermi-Eyges calculated lateral planar fluence distribution. However, this method currently improves superposition calculations in the direction of the beam axis only.

With knowledge of the incident photon spectra, the density of primary photon interactions (and hence the terma) can be quickly and exactly calculated. Monte Carlo electron track histories (the electrons being set in motion by the interaction of primary photons) can be initiated at each voxel with non-zero terma to calculate the primary dose. Using Monte Carlo to calculate the primary dose component rigorously accounts for the effect of inhomogeneities on scattering, as each step of each electron track is explicitly transported as the electron travels through the medium. Hence the density distribution between the interaction and deposition sites is accounted for, not the just average density between these points.

This chapter proposes an X-ray beam dose calculation method which uses explicit transport of pre-generated Monte Carlo particle track data to calculate the primary dose, and superposition to calculate the scatter dose. Only waterlike materials (of varying density) have been used as the absorbing media in this investigation. The effect of varying atomic number on photon dose distributions is currently not accounted for, but rather the problem of changing scattering conditions at interfaces are addressed.

The concept of using superposition to calculate the scatter dose, and explicit electron transport for the primary dose was recently published by Yu *et al.*[156] In this work, Fermi-Eyges electron scattering theory was used to transport the electrons ejected at the primary photon interaction site from which the dose deposited was subsequently calculated.

The concept of using pre-generated Monte Carlo electron tracks is related to the Macro-Monte Carlo method[138, 139] (for electron beam dose calculations) in which pre-generated Monte Carlo data is used to construct probability distributions for the electron transport (in the method described here, the pre-generated electron tracks themselves are transported).

4.2 The Super-Monte Carlo photon beam dose calculation method

4.2.1 Calculation of the primary dose using pre-generated electron track data

Electron track data generation

The EGS4 Monte Carlo code[8] (user code RTPCART[77]) was used with PRESTA[157] turned off to simulate incident photons forced to interact at a point in a unit density water equivalent media. The secondary electrons (and positrons) ejected by the incident photons were transported in discrete steps. The (x,y,z) position, as well as the energy deposited, E_{dep}, of each step of each electron track was written to a file, together with a flag marking whether or not the electron was a δ-ray (knock-on). 5000 incident photons with 6 MV, 10 MV and 18 MV energy spectra were simulated in this way. The spectra of the 6 MV and the 18 MV beams were found from Ahnesjö *et al.*,[82] and the 10 MV spectrum from Mohan *et al.*[43] The electron track data resulting from 5000 incident 10 MV photons uses 11.7 Mb of storage space. Only one Super-Monte Carlo 'kernel' is needed for each beam energy (the effect of beam hardening on secondary electron energy is not accounted for). The EGS4 cut-off parameters were AE = 0.521, AP = 0.010,

ECUT = 0.561 and PCUT = 0.050 MeV. Electron track kernels for 10 and 50 incident 18 MV photons forced to interact at a point in a water phantom are shown in figure 4.1. As the number of incident photons increases, the dose distribution found using this kernel becomes more accurate, however increasing the number of electrons in the kernel increases the calculation time.

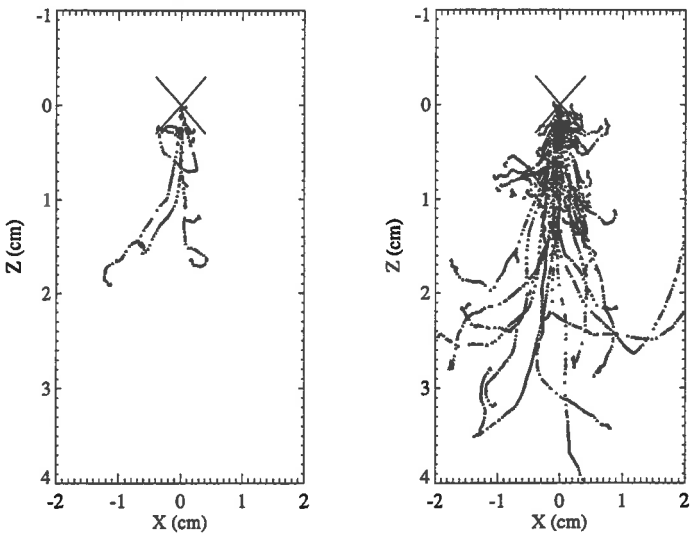

Figure 4.1: **Dotplots of electron track kernels for an 18 MV beam as calculated by Monte Carlo, with (left) 10 incident photons and (right) 50 incident photons. The photons were forced to interact at X.**

The advantage of using *pre-generated* electron track data over a full Monte Carlo simulation is that the computationally intensive Molière, Bhahba and Møller scattering and annihilation and bremsstrahlung particle production routines have already been performed, as well as all the random sampling from probability distributions to determine the type of interaction and angle of scatter. Furthermore, the uncertainty inherent in the random interaction of primary photons is eliminated, since terma is calculated analytically.

Transport of electron tracks

Density scaling of step lengths

The x,y, and z positions in each step of the electron transport are converted to Δx, Δy and Δz step lengths. When the electron track is transported in a unit density voxel the step size is Δx,Δy,Δz, with energy deposition E_{dep}. In a non-unit density voxel (density ρ), the stopping power is proportional to density (for water-like materials), and hence the step size is (Δx/ρ,Δy/ρ,Δz/ρ), while the energy deposition remains E_{dep}. The change in step size with density is shown in figure 4.2.

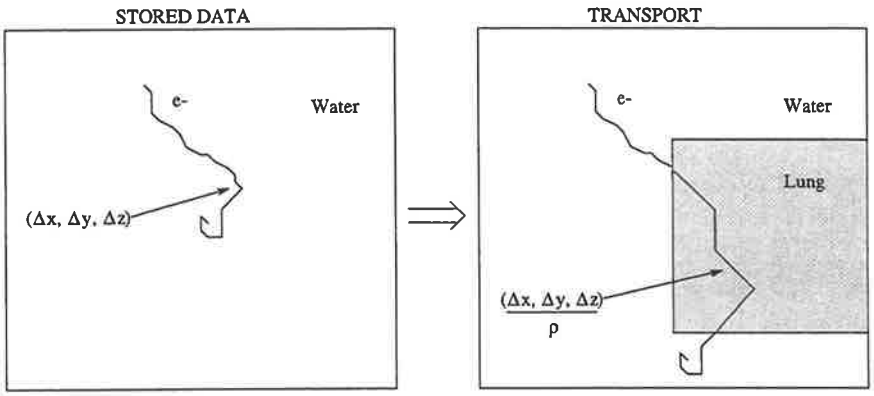

Figure 4.2: **The change in electron step size with density in the transport of the pre-generated Monte Carlo electron tracks in inhomogeneous media.**

Accounting for δ-rays

δ-ray electrons are accounted for by marking the position (x', y', z') where the δ-ray scattering event occurred. The δ-ray is then transported until it stops. The flag of the next electron step indicates the δ-ray has stopped, and therefore transport will resume from point x', y', z'. δ-ray transport is shown in figure 4.3.

Boundary crossing

An electron crossing an interface of density ρ_1 to ρ_2 in the z-direction say, will need its

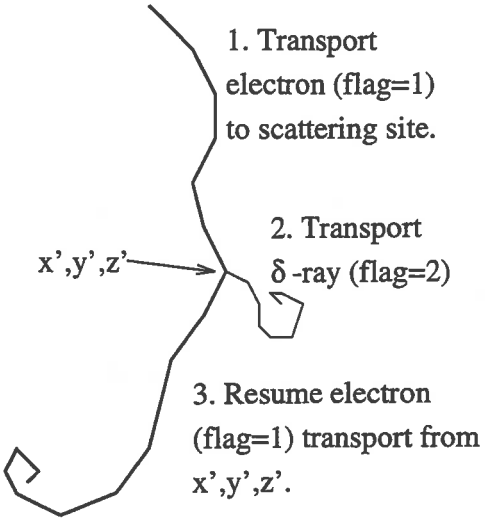

Figure 4.3: **δ-ray transport in the Super-Monte Carlo algorithm.**

step length changed to account for the difference in density. The new z-position becomes

$$z = z_b + \frac{(\Delta z - (z_b - z_{old})) \times \rho_1}{\rho_2} \tag{4.1}$$

where z_{old} and z_b are the previous z-position and z-boundary position respectively. The x and y electron step positions also need to be adjusted by the same ratio as that of the z step (ie. vary the step length without changing the electron direction),

$$\frac{x - x_{old}}{\Delta x} = \frac{z - z_{old}}{\Delta z} \tag{4.2}$$

hence

$$x = x_{old} + \Delta x \times \frac{z - z_{old}}{\Delta z} \tag{4.3}$$

and similarly for y. Thus the change in electron step length across a boundary is explicitly accounted for. The energy deposited in the step is divided between the two voxels either side of the interface depending on the radiological step length in each voxel.

A flowchart of the electron transport and dose calculation process is shown in figure 4.4.

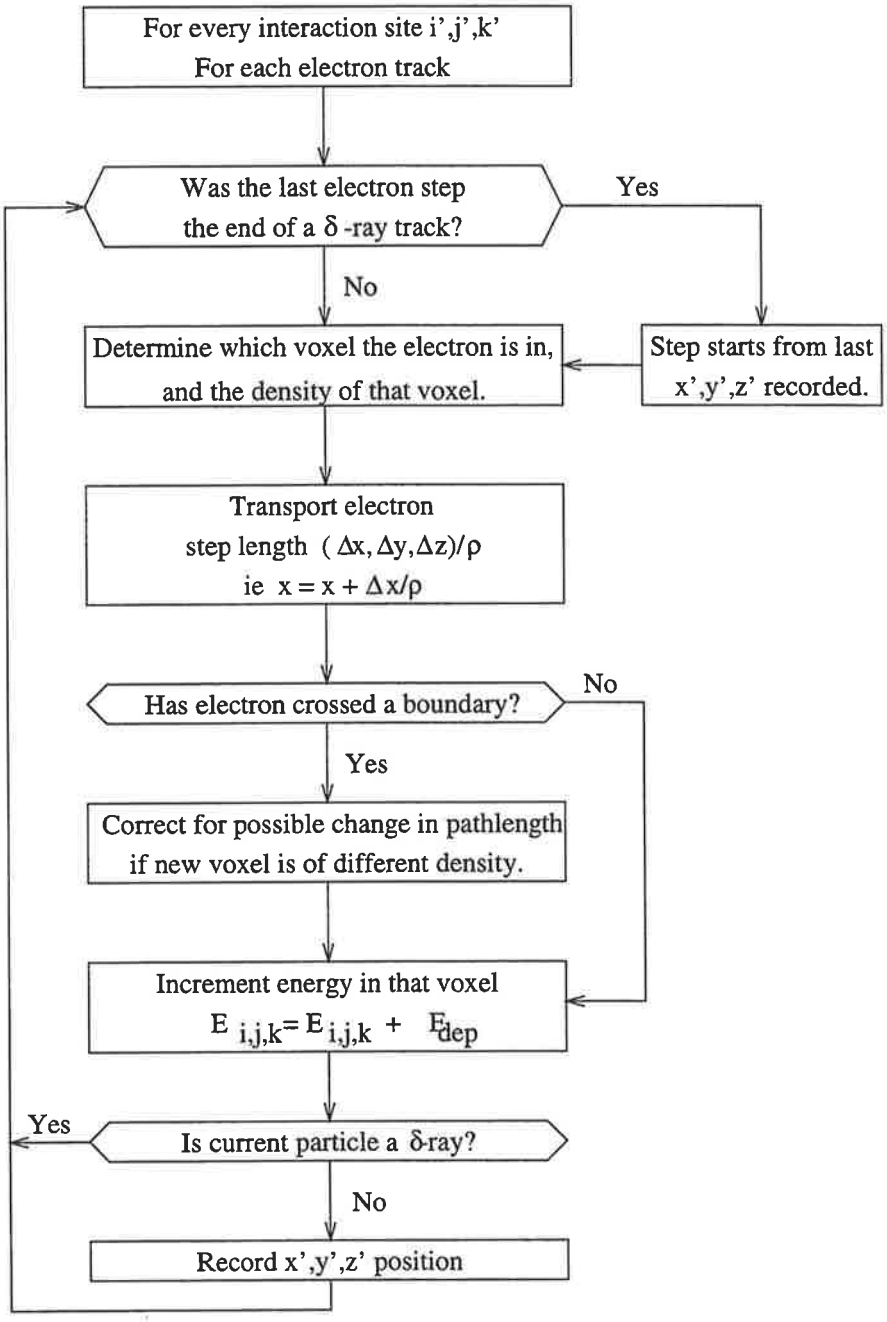

Figure 4.4: **The electron transport algorithm used to calculate the primary dose.**

Variance reduction

Since the primary electron is ejected with azimuthal symmetry, each electron track can be transported any number of times, with each electron track rotated by the appropriate amount. As a compromise between accuracy and calculation speed (a variance reduction technique) each electron track can be transported up to 4 times- once in each quadrant in the X-Y plane from each primary photon interaction site (voxel), as in figure 4.5. Using this symmetry is analogous to generating energy deposition kernels in standard superposition, where the geometrical symmetry is used to obtain energy deposition which is uniform with respect to azimuthal angle.

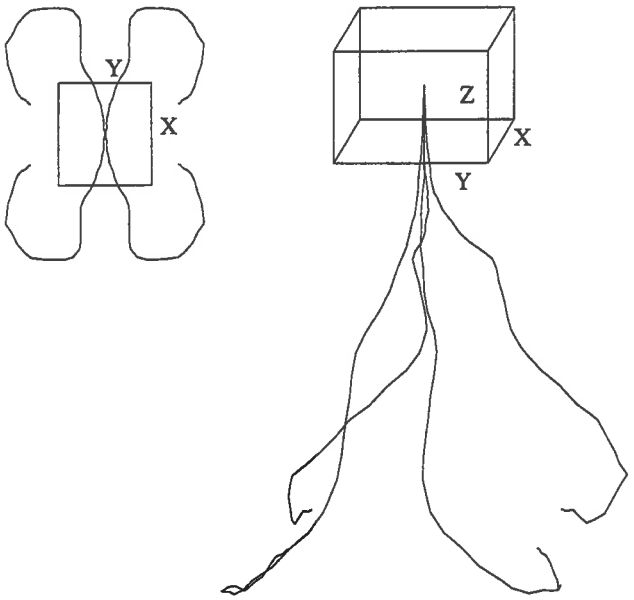

Figure 4.5: **Each electron is transported in each of the positive and negative x and y quadrants, shown in the x-y plane (left) and an oblique perspective (right).**

Calculating primary dose

The primary dose can be found by summing $E_{dep,m,l}(i-i', j-j', k-k')$, the energy deposited in voxel i, j, k from the steps n to n' of electron track m which fall in that voxel (normalised by the sum of the energy of all the tracks), weighted by the terma of

the interaction voxel, $T_{i',j',k'}$,

$$D_p(i,j,k) = \frac{1}{\rho_{i,j,k}} \sum_{i',j',k'} T_{i',j',k'} \rho_{i',j',k'} \sum_{m=0}^{M} \sum_{l=n}^{n'} E_{dep,m,l}(i-i', j-j', k-k'). \qquad (4.4)$$

The number of histories chosen (5000) was a compromise between better statistics and data storage size. This number of electrons, transported from each interaction voxel corresponds to a Monte Carlo simulation with least 30 million incident photons for a 5×5 cm^2 field. When comparing a SMC kernel generated in a unit density media to a 5×10^6 history Monte Carlo kernel (both scored in a 0.5×0.5×0.5 cm^3 voxel array), the maximum difference between any two voxels in the fractional dose distributions was less than 0.7% of the maximum dose for 6 MV, 10 MV and 18 MV beam energies.

A more detailed description of the code used for SMC for photon beam dose calculation is found in appendix A.

4.2.2 Calculation of the scatter dose by superposition

Polyenergetic energy deposition kernels[87] were generated using the EGS4 Monte Carlo code[8] for densities from 0.2 g cm^{-3} to 1.9 g cm^{-3}, in increments of 0.1 g cm^{-3} for the scatter dose at 6 MV, 10 MV and 18 MV photon beam energies. In forming the kernels 5×10^6 photons were forced to interact at a point 2.25 cm deep in a Cartesian array (0.5×0.5×0.5 cm^3 voxels). Energy imparted and deposited due to scatter photons, annihilation and bremsstrahlung photons subsequently produced from each incident photon, was weighted by the attenuation coefficient of the incident photon.[44]

The scatter dose, D_s, was obtained by convolving the polyenergetic scatter dose kernels,

$H_s(i-i', j-j', k-k', \rho_{ave})$, with the terma as in equation 2.8,

$$D_s(i,j,k) = \sum_{i',j',k'} T_{i',j',k'} \rho_{i',j',k'} H_s(i-i', j-j', k-k', \rho_{ave})/\rho_{ave}. \qquad (4.5)$$

The total SMC dose is the sum of equations 4.4 and 4.5. Note the similarity between these two equations.

To investigate the accuracy of the SMC method, dose distributions in all the phantoms tested were generated using both superposition alone, and Monte Carlo alone.

4.2.3 Superposition calculations

Polyenergetic primary *and* scatter energy deposition kernels were generated for densities from 0.2 g cm^{-3} to 1.9 g cm^{-3}, in increments of 0.1 g cm^{-3} at 6 MV, 10 MV and 18 MV photon beam energies. In forming the kernels 5×10^6 photons were forced to interact at a point 2.25 cm deep in a Cartesian array ($0.5\times0.5\times0.5$ cm^3 voxels).

The total superposition dose was obtained by summing the convolution of the primary and scatter energy deposition kernels with the terma,

$$D(i,j,k) = \sum_{i',j',k'} T_{i',j',k'} \rho_{i',j',k'} \left(H_p + H_s\right). \qquad (4.6)$$

4.2.4 Monte Carlo calculations

The EGS4 Monte Carlo code[8] was used, with PRESTA[157] to calculate dose distributions. Primary and scatter dose arrays were recorded separately. AE was set to 0.521 MeV, AP to 0.01 MeV, ECUT to 0.561 MeV and PCUT to 0.05 MeV. Monodirectional incident

photons of energies 6 MV, 10 MV and 18 MV were transported through the water-lung-water phantoms described below, and the subsequent energy deposited was recorded in a Cartesian array of $0.5\times0.5\times0.5$ cm^3 voxels. At least 5×10^7 incident photons were used for each simulation, and the 4-quadrant symmetry of the phantoms was used to reduce the statistical variance by 4.

4.2.5 Phantoms

If a kernel generated by a dose calculation algorithm in an arbitrary geometry gives a dose distribution very similar to that of a Monte Carlo kernel dose distribution, then the superposition of these kernels for a broad beam will give a distribution very similar to that for a Monte Carlo generated broad beam geometry. The phantoms used for comparing SMC and superposition calculated kernels with Monte Carlo generated kernels are shown in figure 4.6.

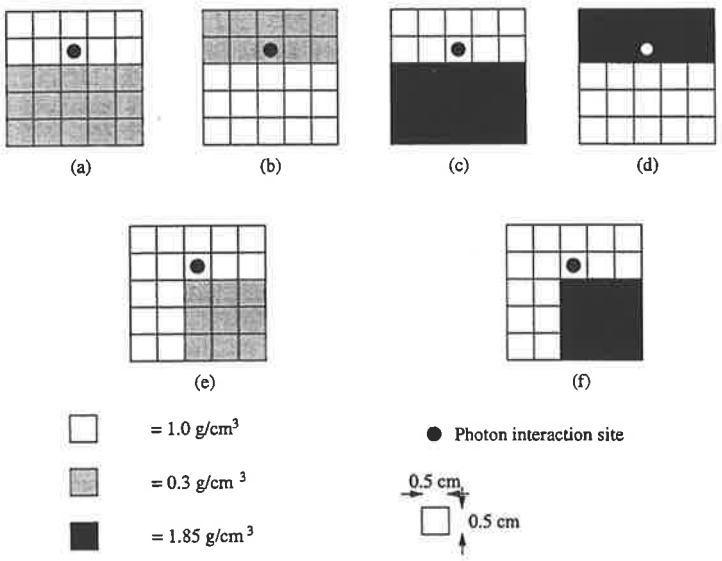

Figure 4.6: **A schematic diagram of the phantoms used to test the SMC algorithm for photons forced to interact at a point.**

The phantoms used to investigate the accuracy of SMC for broad beams were the water-lung-water phantom of Metcalfe *et al.*[6] (similar to that of Woo *et al.*[96]), and the two lung-block phantom of Ahnesjö.[81] The water-lung-water phantom is composed of a 4 cm slab of water, 8 cm slab of 0.3 g cm^{-3} density water to simulate lung, and a further 8 cm of water (see figure 3.3). The two lung-block phantom has lung-water interfaces both parallel and perpendicular to the incident beam direction, with the lung blocks starting at z = 5 cm to z = 25 cm, beginning 2.5 cm off axis in the x-direction, and extending through the phantom in the y-direction, as in figure 4.7.

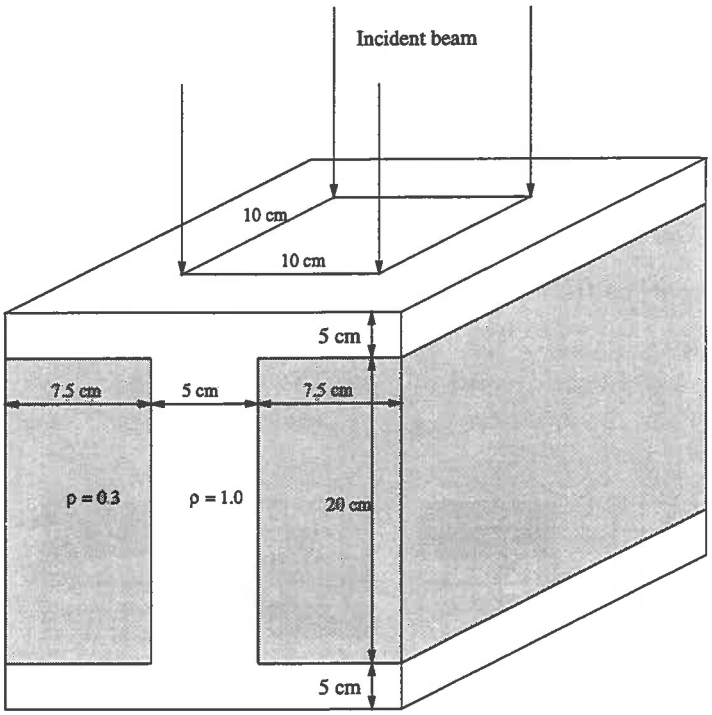

Figure 4.7: **A schematic diagram of the two lung-block phantom used to test the SMC algorithm for broad beams.**

Only water equivalent materials (of different density) have been used in this work. The effect of different atomic number materials has not been investigated. However Ahnesjö[81] showed that for 4 - 24 MV beam energies, $\overline{E_{ab}}/\overline{E}$ and $\overline{\mu}/\rho$ vary little between water and the ICRP muscle, bone, lung and adipose tissue phantoms,[159] so the water equivalence assumption should be valid for the terma calculation. The lower mass stop-

ping power of bone relative to water means that electron range is slightly longer than is predicted by treating bone as being water equivalent, and the increased effective atomic number means that electron scattering will be increased in bone.

4.3 Results

4.3.1 Single interaction site results

Primary energy deposition kernels for photons forced to interact at a point in the geometries shown in figure 4.6 were calculated using SMC, superposition and Monte Carlo. Table 4.1 shows the normalised mean square difference between Monte Carlo and superposition calculated energy deposition distributions, and Monte Carlo and SMC energy deposition distributions.

Table 4.1: **Normalised mean square energy deposition differences between SMC calculated kernels and Monte Carlo calculated kernels, and superposition kernels and Monte Carlo kernels in various media, summed over every voxel in the energy deposition arrays.**

Energy	Σ(SMC - EGS4)^2	Σ(Supn. - EGS4)^2
6 MV	1.0	6.9
18 MV	1.0	6.2

The results from table 4.1 show that SMC generated kernels are closer to Monte Carlo distributions than are superposition calculated kernels. Hence for a broad beam geometry SMC should give more realistic dose distributions than will superposition calculations.

The SMC generated kernels are also better at predicting energy deposition than the FE scaling superposition calculated kernels shown in chapter 3 by a factor of 3-4, and SMC has the advantage that it can account for arbitrary geometries, and not just slab inhomogeneities.

4.3.2 Depth dose curves in a water-lung-water phantom

The 5×5 cm^2 18 MV 100 cm SSD lung phantom experimental results of Metcalfe *et al.*[6] are compared to SMC, Monte Carlo and superposition calculated depth dose curves in figure 4.8 (the lung phantom is shown schematically in figure 3.3). This figure shows that superposition overestimates the dose at the beginning of the lung, and underestimates the dose in the secondary build-up region. The SMC dose agrees well with Monte Carlo and experimental results over the whole range of the curve. The slight discrepancy between Monte Carlo and experiment in this figure is probably due to the spectrum used in the Monte Carlo simulation not quite matching the actual spectrum of the beam.

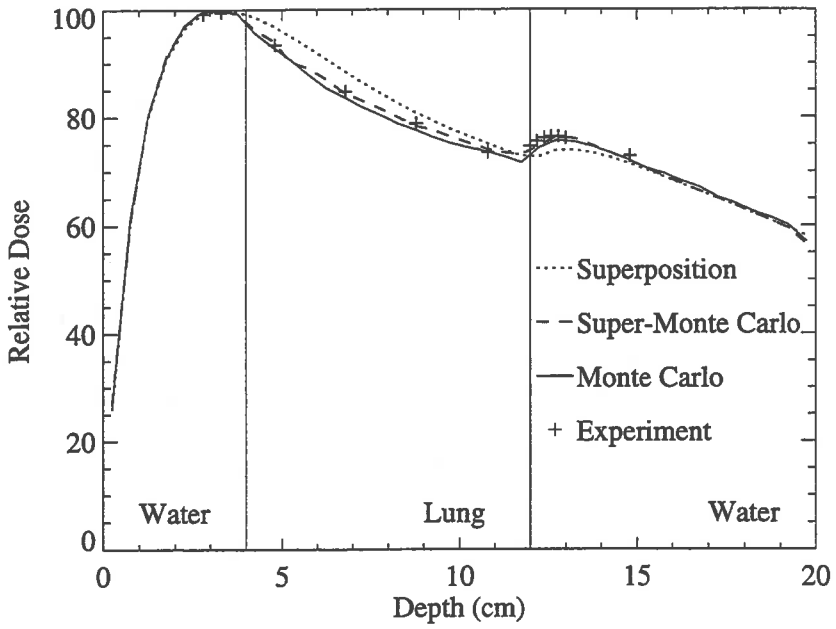

Figure 4.8: **Total dose central axis depth dose curves for a 5×5 cm^2 100 cm SSD 18 MV photon beam.**

6 MV, 10 MV and 18 MV primary and scatter depth dose curves in the water-lung-water phantom for 5×5 cm^2 and 10×10 cm^2 infinite SSD fields calculated by SMC, Monte Carlo and superposition are shown in figures 4.9, 4.10 and 4.11 respectively. These figures show that the SMC primary depth dose curve shows closer agreement with the Monte

Carlo depth dose curve than the superposition curve. For the 18 MV 5×5 cm^2 field, the maximum difference in the depth dose curve between superposition and Monte Carlo is approximately 5%, whereas that of SMC and Monte Carlo is less than 1.5%. With increasing field size, and decreasing energy, the discrepancy between SMC, superposition and Monte Carlo decreases. The scatter dose component from both SMC and superposition in all of the fields is in good agreement with the Monte Carlo scatter dose. Note that the scatter dose component of SMC and superposition is identical as the same method (superposition) of dose calculation was used.

The SMC calculated distributions are closer to Monte Carlo than the FE scaling calculated dose distributions of chapter 3 (but they take longer to compute).

4.3.3 Profile curves at mid-lung in a water-lung-water phantom

To investigate the penumbral prediction of SMC, dose profiles at mid-lung were taken at 8.25 cm deep in the water-lung-water phantom for a 5×5 cm^2 18 MV beam using SMC, Monte Carlo and superposition. The results are shown in figure 4.12. This figure shows that SMC is very close to Monte Carlo in both absolute dose and penumbral shape.

4.3.4 Isodose curves in a two lung-block phantom

To investigate the situation where inhomogeneous interfaces exist both parallel and perpendicular to the incident beam direction, dose distributions for a 10×10 cm^2 monodirectional 10 MV beam in the two lung-block phantom ($\rho_{lung} = 0.30$ g cm^{-3}) were calculated using SMC, Monte Carlo and superposition. The resulting curves are shown in figures 4.13 and 4.14. The isodose curves generated with SMC show greater general consistency with

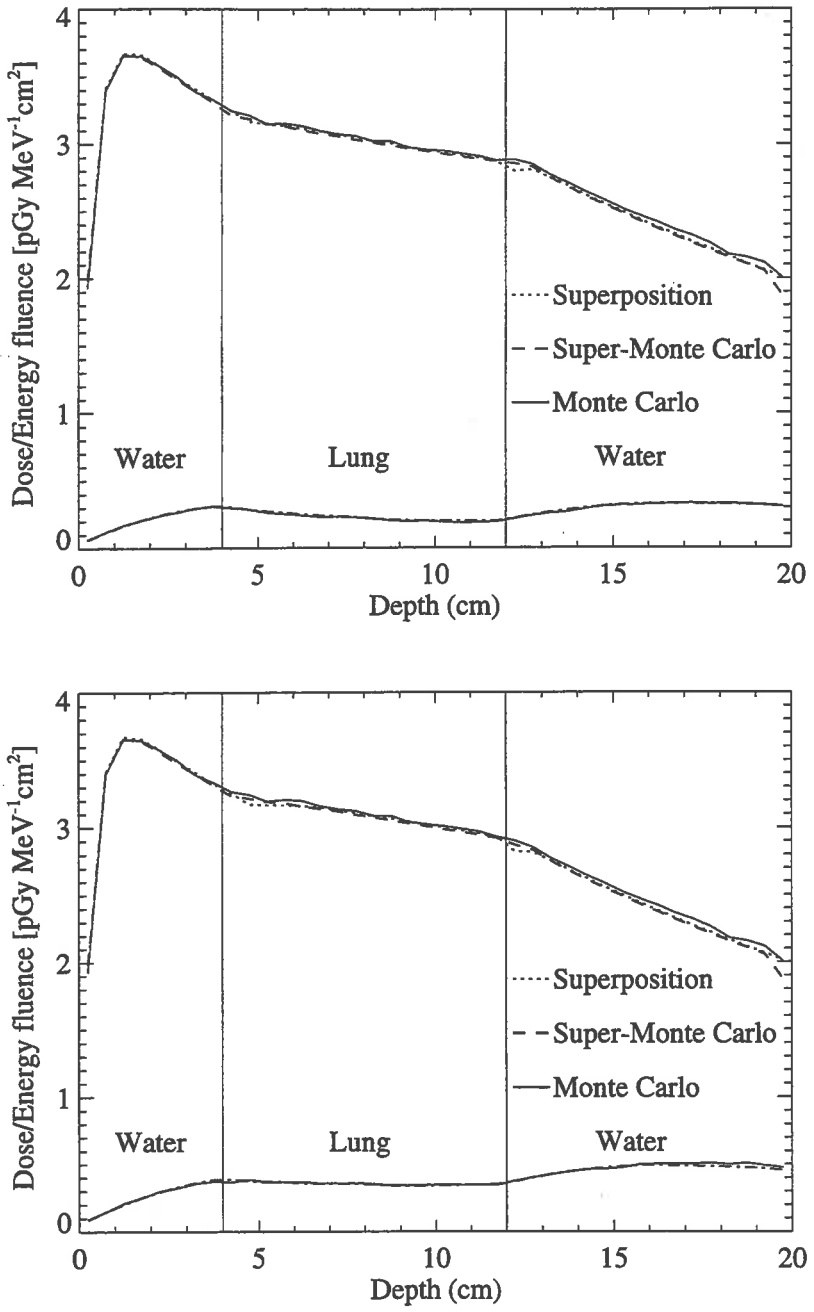

Figure 4.9: **Primary and scatter central axis depth dose curves for a 6 MV parallel photon beam with field size 5×5 cm^2 (top) and 10×10 cm^2 (bottom).**

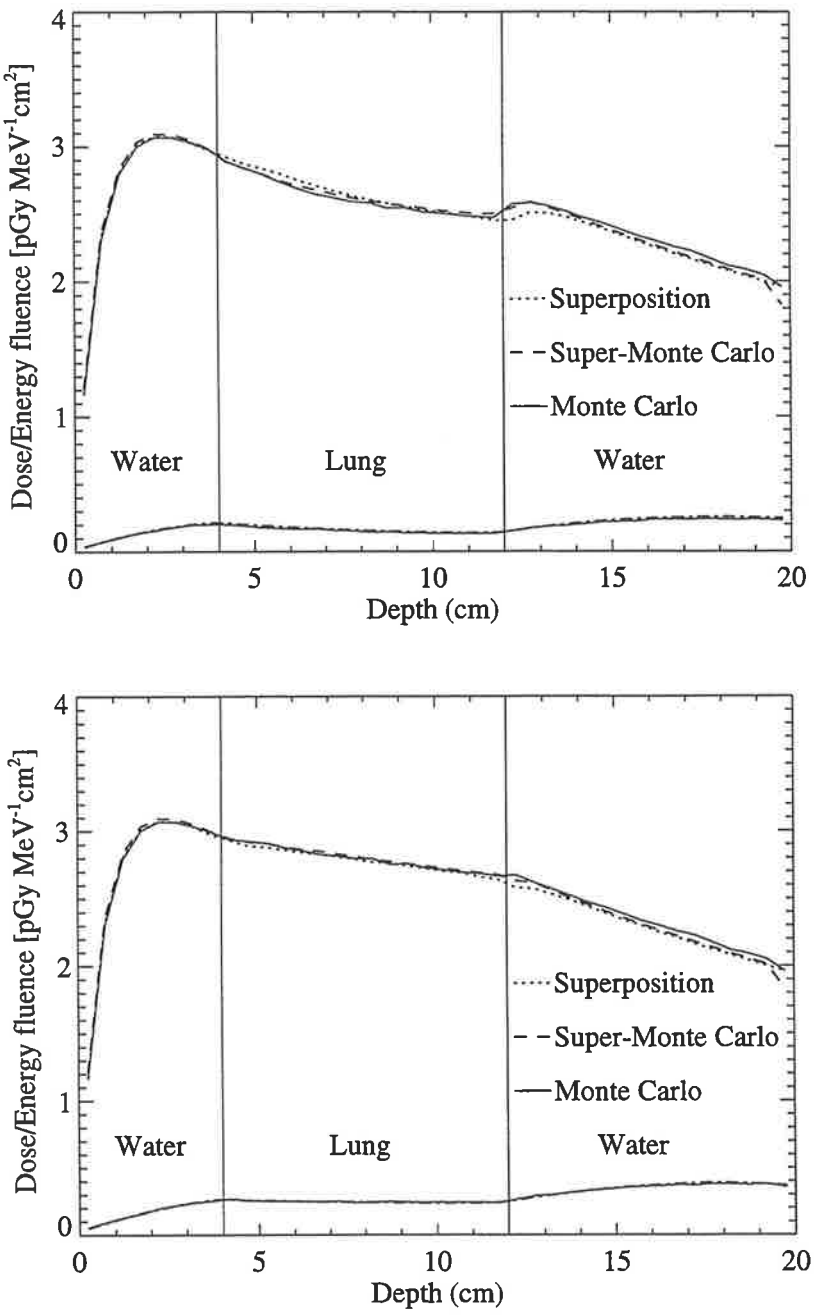

Figure 4.10: **Primary and scatter central axis depth dose curves for a 10 MV parallel photon beam with field size 5×5 cm^2 (top) and 10×10 cm^2 (bottom).**

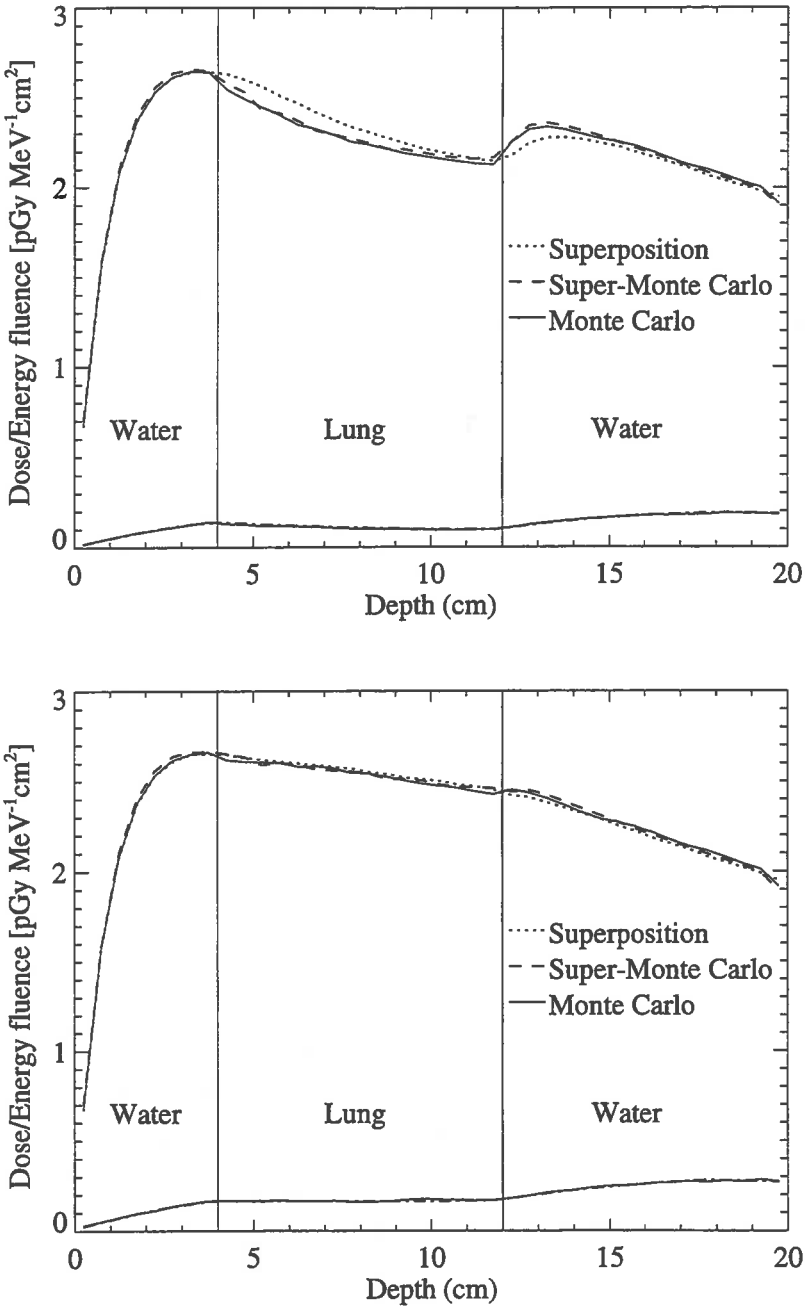

Figure 4.11: **Primary and scatter central axis depth dose curves for an 18 MV parallel photon beam with field size 5×5 cm^2 (top) and 10×10 cm^2 (bottom).**

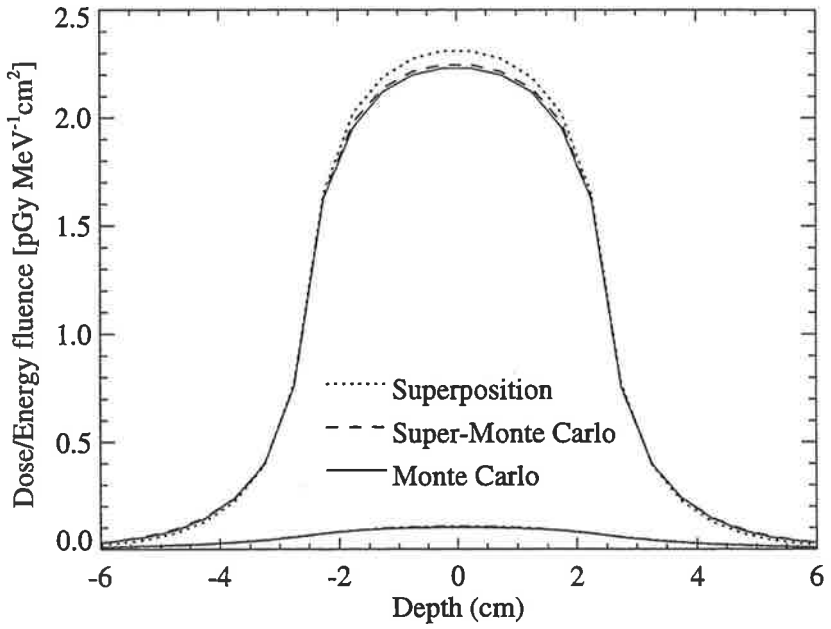

Figure 4.12: **Primary and scatter dose profile curve at 8.25 cm deep in a water-lung-water phantom for an 18 MV 5×5 cm^2 beam calculated using Super-Monte Carlo, Monte Carlo and superposition.**

Monte Carlo generated curves than do isodoses generated using superposition. Note especially the 2.5 pGy MeV^{-1} cm^2 isodose line, where the SMC curve follows Monte Carlo at the lung/water interface more closely than does superposition.

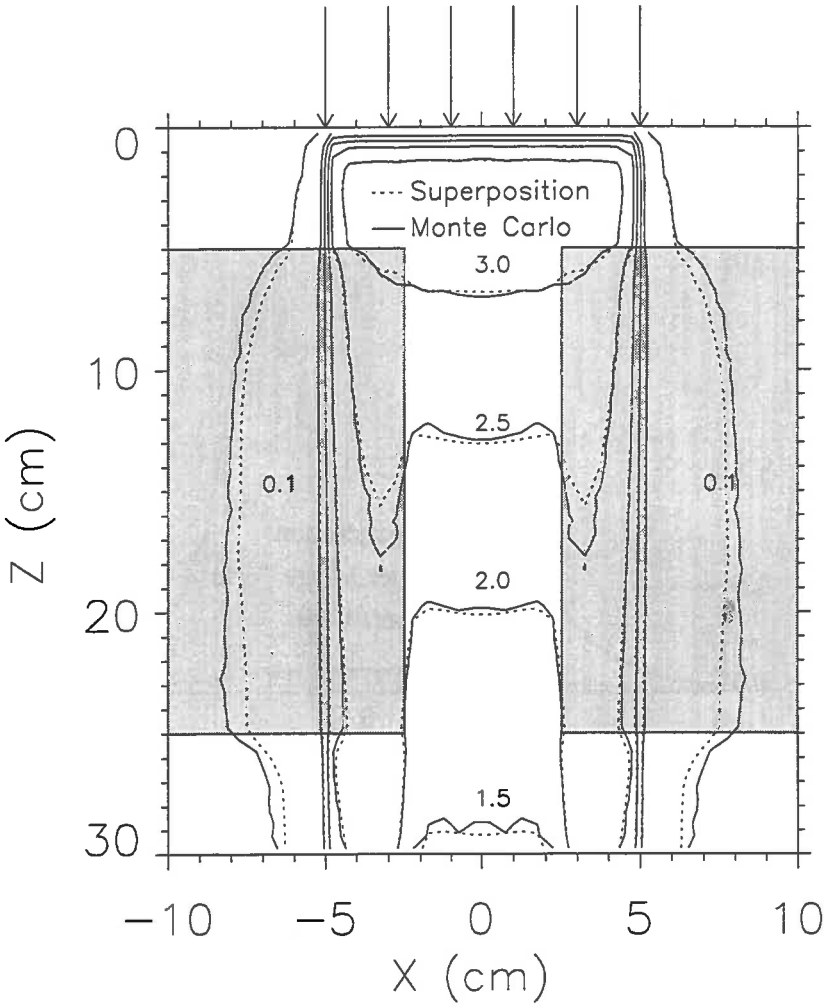

Figure 4.13: **Isodose curves resulting from a 10×10 cm^2 parallel 10 MV beam incident on a two block-lung phantom The solid line is Monte Carlo, and the dashed line is superposition. The isodose numbers refer to dose/energy fluence (pGy MeV^{-1} cm^2).**

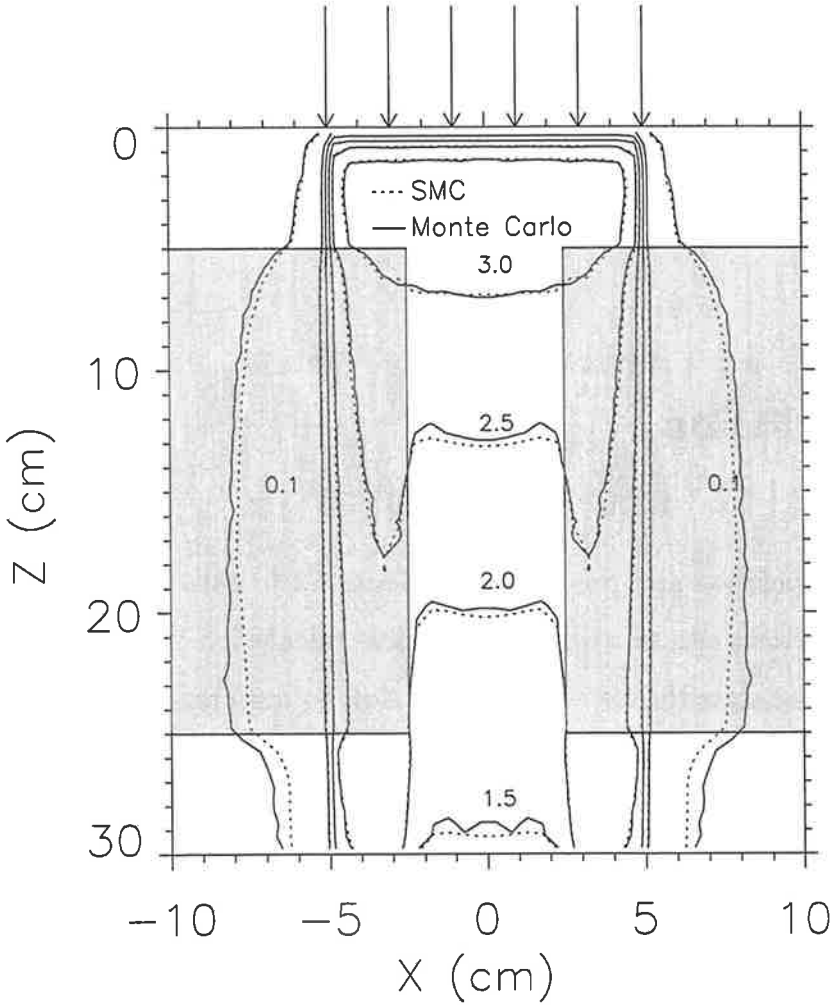

Figure 4.14: **Isodose curves resulting from a 10×10 cm^2 parallel 10 MV beam incident on a two block-lung phantom The solid line is Monte Carlo, and the dashed line is Super-Monte Carlo. The isodose numbers refer to dose/energy fluence (pGy MeV^{-1} cm^2).**

4.3.5 Computation time

To calculate the dose distribution for a 5×5 cm^2 10 MV beam using SMC takes approximately 2 hours of CPU time on a DECalpha 3600 175 MHz platform. For the same geometry, superposition takes approximately 4 minutes, while Monte Carlo takes 30 hours. SMC is currently too slow for clinical use, though, with algorithm optimisation, and on a more powerful platform, SMC would be particularly advantageous for planning when significant inhomogeneities are present, such as in the neck and thorax.

4.4 Conclusion

Combining superposition and pre-generated Monte Carlo data has yielded a dose calculation tool that is accurate to within 1.5% in dose calculation for the geometries investigated. Though the algorithm is currently too slow to use clinically, it is envisaged that with optimisation (of both the algorithm itself and variables such as ECUT and AE), and on a powerful platform SMC could be a realistic dose calculation option. The advantage of SMC over superposition is significant for small fields and high energies at interfaces of different density. The interface problem of the rectilinear scaling method in the primary dose superposition calculation is eliminated in SMC.

The scatter dose calculated by superposition (and hence SMC) agrees well with Monte Carlo for all the energies and field sizes investigated.

External photon beam SMC does not yet account for different atomic number materials in the absorbing medium, nor does it account for the hardening in the spectrum of the secondary electrons with depth.[44] To account for atomic number effects, a similar method to that used in chapter 5 could be incorporated. Inclusion of such a method is likely to produce good results, at the expense of computation time. Such a method

may need to account for the different initial angular distribution of electrons ejected at a photon interaction site in different atomic number materials (however the ejected electrons become increasingly forward directed as energy increases).

The hardening of the spectrum of the secondary electrons with depth could be accounted for by changing the weights of the electrons assigned to monoenergetic electron track kernels with depth.

For X-ray dose calculation, the method of using pre-generated Monte Carlo particle track data could be used to calculate both primary and scatter dose, if both photon and electron track data are recorded. This technique would require large data storage space, and would involve longer calculation time, however, it is still likely to be considerably faster than a full Monte Carlo simulation, and is potentially as accurate.

Chapter 5

Super-Monte Carlo for Electron Beam Planning

5.1 Introduction

This chapter investigates a new method of electron beam dose calculation, the Super-Monte Carlo (SMC) method, based on the SMC method used for X-ray beams (see chapter 4), with modifications included to account for the change in electron scattering, energy loss and bremsstrahlung production in different density and atomic number materials.

Most planning systems use a pencil beam algorithm to calculate electron dose (described in section 2.3.3). The limitations of the pencil beam algorithm are also discussed in that section. Electron beam superposition has been proposed as a dose calculation algorithm (refer section 2.3.10), however this approach is limited by the rectilinear density scaling approximation.[151] SMC uses a superposition of electron track kernels (as opposed

to energy deposition kernels in standard superposition calculations) to calculate dose, eliminating the rectilinear scaling approximation. The limitations of the pencil beam algorithm are also overcome by SMC.

Only pure electron beams (no photon contamination) have been used in this investigation.

To accurately transport charged particles through a heterogeneous absorbing medium, knowledge of the scattering power, stopping power and radiation yield of the different components in the medium is required. These quantities are outlined in chapter 1.

5.1.1 The problems with electron beam superposition

As with X-ray beam superposition, electron beam superposition uses rectilinear density scaling to calculate the average density between the surface point of the energy deposition kernel, and the dose calculation point. Woo and Cunningham[151] state that the underlying reason for the inaccuracy of the convolution method as applied to electron beams[135, 136, 137] is the rectilinear density scaling method. They state that this discrepancy is much more severe for electron beams than for photon beams. They describe this concept by considering the dose delivery to a point P located at d cm below an air gap t cm thick, embedded in a water phantom at a small distance x below the surface, as shown in figure 5.1. Consider only the dose contribution from primary electrons, which is the dominant component under the lack of electronic equilibrium conditions. The dose contribution to P can be divided into two parts, D_1, from electrons originating above the gap, and D_2, from electrons originating below the gap. D_2 can be very accurately determined using the convolution method, since electrons originating below the gap arise and travel in a homogeneous water medium. D_1, however, is approximated using rectilinear density scaling and may involve an error.

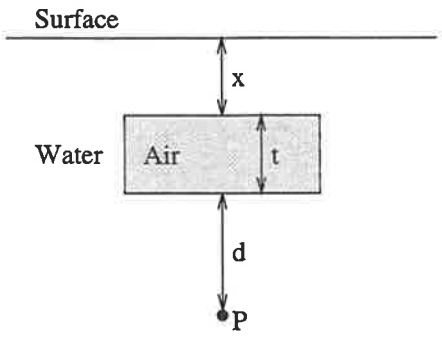

Figure 5.1: **An illustration of the geometry used to highlight the limitation of electron beam superposition.**

For photon beams, a large percentage of the dose contribution comes from the immediate vicinity of P_1, so in general D_2 is significant except for points very close to the gap. As a result the error becomes a small fraction of the total dose.

For electron beams all the primary electrons originate at the surface of the phantom. The dose contribution from primary electrons originating above the air gap, D_1, will involve a similar error to the value of D_1 calculated for the photon case. However, the dose contribution from primary electrons originating below the air gap, D_2 will be zero. Hence the error incurred is no longer a fraction of the sum of D_1 and D_2, but of D_1 alone,[151] and therefore the total error is higher in the electron beam case.

As with photon beam superposition, electron beam superposition also does not account for different atomic number absorbing materials.

5.2 The Super-Monte Carlo electron beam dose calculation method

5.2.1 Electron track data generation

The EGS4 Monte Carlo code[8] was used with PRESTA[157] turned off to simulate incident electrons initiated at a point in a unit density water equivalent media. The electrons were transported in discrete steps. The (x,y,z) position (as scored in the AUSGAB routine of the EGS4 user code RTPCART[77]), the energy deposited, E_{dep}, and the kinetic energy of the electron, E, of each step for every electron track was written to a file. A δ-ray electron was marked with a different flag to the incident electron. To limit the maximum allowable electron step size the input variable SMAX was set to 0.05 cm. 3000 incident electron tracks at 6 MeV and 15 MeV were generated in this way, thus making an electron track kernel for each energy. The EGS4 cut-off parameters were AE = 0.521, AP = 0.010, ECUT = 0.611 and PCUT = 0.050 MeV. The low AE and AP values mean that energy loss events (both Møller and bremsstrahlung) above 10 keV are modelled explicitly, thereby giving accurate transport of the primary electrons. δ-rays above 100 keV are transported. Energy deposition by bremsstrahlung photons generated in the absorbing medium is ignored, so the choice of PCUT is arbitrary.

The (x, y, z) position of each step was converted into spherical co-ordinates $(\Delta r, \Delta\phi, \Delta\theta)$ for that step. A 15 MeV electron track kernel (50 incident electrons) is shown in figure 5.2.

The advantage of using *pre-generated* electron track data is that the computationally intensive Molière and Møller scattering, and bremsstrahlung photon production routines have already been performed, as well as the random sampling from probability distributions to determine the type of interaction and angle of scatter.

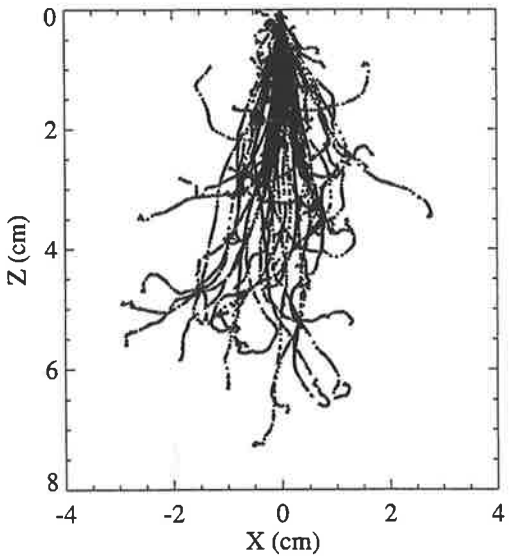

Figure 5.2: **A Monte Carlo calculated dotplot of 50 incident 15 MeV electrons making up an electron track kernel.**

5.2.2 Stopping power, scattering power and radiation yield ratios

Since the electron tracks are generated in water, in the transport of these tracks through a non-unit density material, each step length must be multiplied by the inverse of the local density (an application of O'Connor's theorem[57]) to account for the density change. If a different atomic number material is used, the change in scattering, collisional energy losses and differences in bremsstrahlung production also need to be accounted for. These variables are energy dependent (see chapter 1), however the *ratios* of these variables to those of water are less energy dependent. These ratios are outlined below.

Stopping power ratio

The mass stopping power ratios of water/aluminium, water/bone and water/lucite are shown in figure 5.3. The water/aluminium ratio changes by approximately 7% over the range of the graph, however the ratios of bone and lucite are more constant. A second order polynomial fit was used to include the energy dependence of the mass stopping power ratios of water to aluminium, water to bone and water to lucite.

Scattering power ratio

Figure 5.4 shows the ratios of the mass scattering powers of aluminium to water, ICRP bone[159] to water, and lucite to water. These ratios differ by less than 3% between 0.5 and 20 MeV. From this graph, a constant value of the mass scattering power ratio was taken for each of aluminium/water, bone/water and lucite/water.

Energy deposition ratio

The ratios of the proportion of energy deposited by electrons (the amount of kinetic energy not given to radiation) for aluminium/water, bone/water and lucite/water are shown in figure 5.5. These ratios show a near linear variation from 0.5 to 20 MeV. A linear function was used to approximate the ratios of the proportion of energy deposited by electrons.

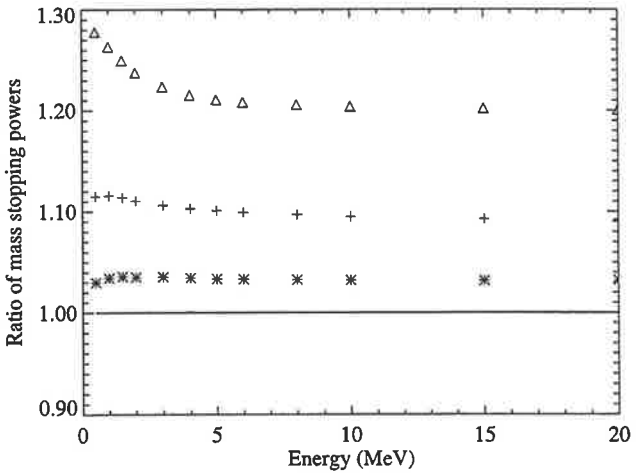

Figure 5.3: **Ratios of mass collisional stopping powers, water to aluminium (△), water to bone (+) and water to lucite (*). Data taken from tables in ICRU 35.**[25]

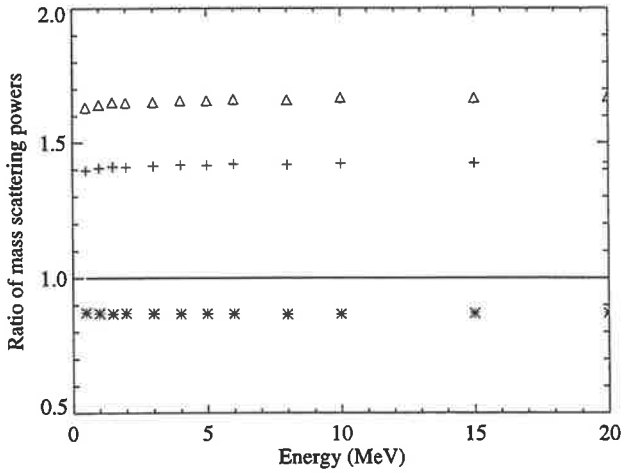

Figure 5.4: **Ratios of mass scattering powers, aluminium to water (△), bone to water (+) and lucite to water (*). Data taken from tables in ICRU 35.**[25]

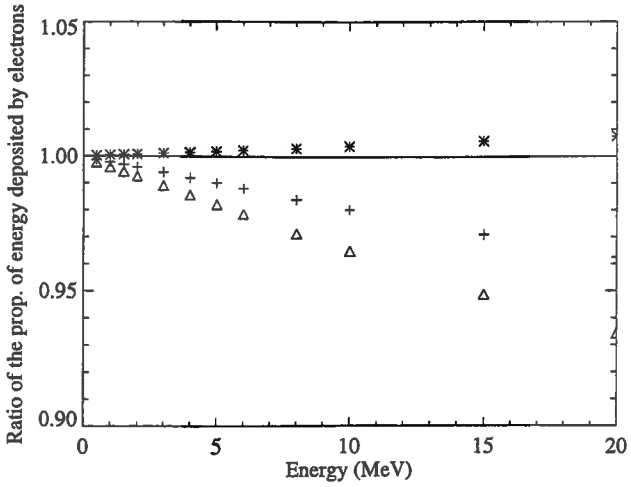

Figure 5.5: **Ratios of the proportion of electron kinetic energy not given to bremsstrahlung radiation, $(1-Y_x)/(1-Y_w)$, aluminium to water ($\triangle$), bone to water (+) and lucite to water (*). Data taken from tables in ICRU 37.**[26]

5.2.3 Transport of electron tracks

Using the ratios outlined above, each electron step of each track is explicitly transported through a material with density ρ_k, of arbitrary composition by altering the following quantities.

Step length

The step length Δr_w in water will become

$$\Delta r_k = \Delta r_w \times S_{col}(E)_k^w \tag{5.1}$$

in medium k, where $S_{col}(E)_k^w$ is the ratio of the collisional stopping power in water to that in material k at energy E. (The use of the collisional stopping power is further discussed in appendix B.)

Scattering angle between steps

The polar scattering angle in water between successive steps, θ_w, becomes in material k (as shown in figure 5.6)

$$\theta_k = \theta_w \times \sqrt{(T)^k_w \, (S_{col}(E))^w_k}, \tag{5.2}$$

where $(T)^k_w$ is ratio of the scattering power of material k to that of water (the azimuthal angle, ϕ_k is randomly chosen in EGS4,[8] so no scaling need be performed in SMC, hence $\phi_k = \phi_w$). The $\sqrt{(S_{col}(E))^w_k}$ term is used because the electron steps themselves have been altered by the stopping power ratio. (A more detailed description of accounting for the change in scattering angle, θ_k, is given appendix C.)

Energy deposited in each step

The energy deposition of each step, $E_{dep,w}$ is altered by the proportion of energy not given to bremsstrahlung (ie. the energy deposited locally) in medium k by the equation

$$E_{dep,k} = E_{dep,w} \times \frac{1 - Y_k(E)}{1 - Y_w(E)}, \tag{5.3}$$

where $Y_k(E)$ and $Y_w(E)$ are the radiation yield in medium k and water respectively. Equation 5.3 assumes that the total energy lost in a step ($E_{tot} = E_{dep} + E_{rad}$, where E_{rad} is the energy radiated away) will be the same in water as it is in medium k, ie. $E_{tot,w} = E_{tot,k}$. Strictly it is the energy deposited in each step that should be the same in water and k, ie. $E_{dep,w} = E_{dep,k}$, with the energy of the electron reduced by a different amount at the end of each step depending on the radiation yield. This would mean that a track in a high atomic number material would have less steps than in water (or more steps in a lower atomic number material!), making the calculation difficult. The assumption $E_{tot,w} = E_{tot,k}$ is justified as $E_{rad} \ll E_{dep}$.

An electron track generated in water (from the kernel track data set), and the same

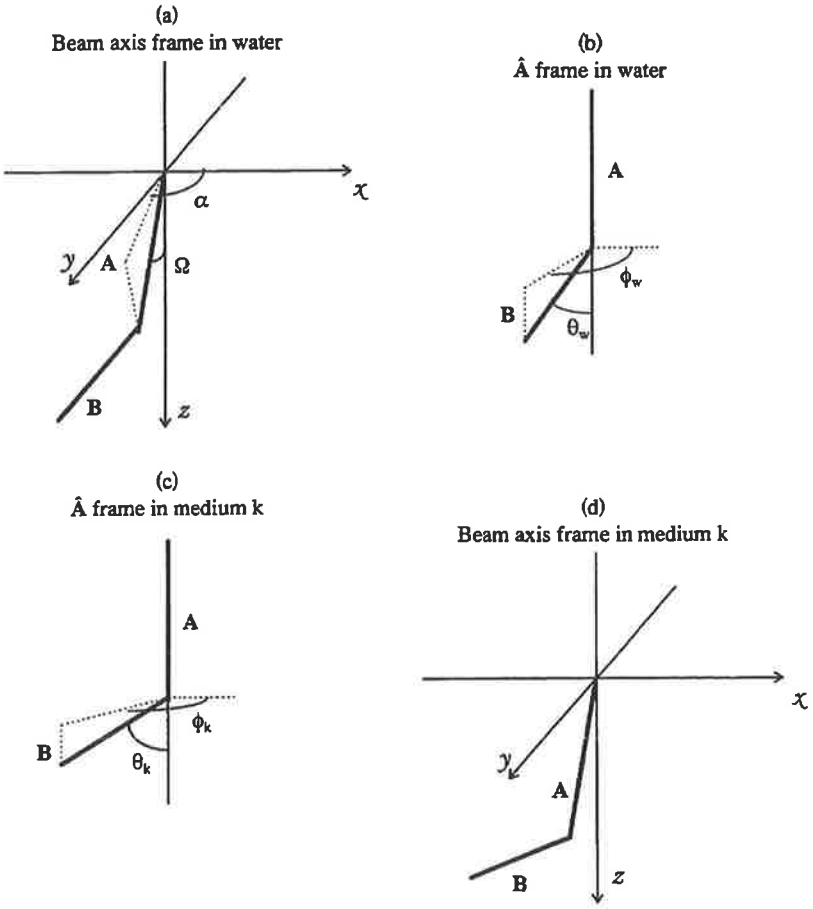

Figure 5.6: **Accounting for the change in step direction in a medium of different scattering power, k. (a) The azimuthal and polar angles, α and Ω respectively, are determined in the beam axis frame in order to transform into the $\hat{\mathbf{A}}$ frame. (b) θ_w and ϕ_w are then determined in water, in the frame of $\hat{\mathbf{A}}$. (c) θ_k is calculated in the $\hat{\mathbf{A}}$ frame in medium k. (d) To determine the new direction of vector B in medium k, the coordinates are transformed back into the beam axis frame. Further discussion of this figure is found in appendix C.**

track transported in an aluminium phantom using SMC are shown in figure 5.7 (δ-rays are not shown). The aluminium track is shorter due to the increased stopping power, and the track shows a larger lateral deviation for its length as it is scattered more with each step. However, the overall shape of the track transported in aluminium is similar to the shape of the track generated in water.

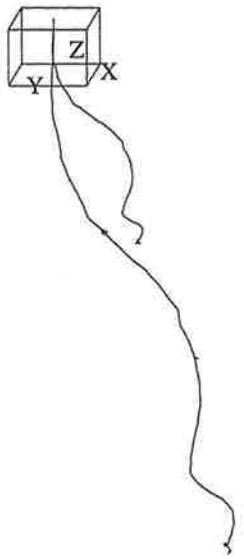

Figure 5.7: **An electron track generated in water (longer track), and the same track transported in a homogeneous aluminium phantom with scattering and stopping power differences accounted for (shorter track). δ-rays are not shown.**

Each electron track is transported as outlined in chapter 4 (however, only from each voxel on the surface of the absorbing medium in the electron beam case). Also, each electron can be transported in 1-4 directions as a variance reduction technique as described in chapter 4. The SMC electron transport and energy deposition process is shown in figure 5.8.

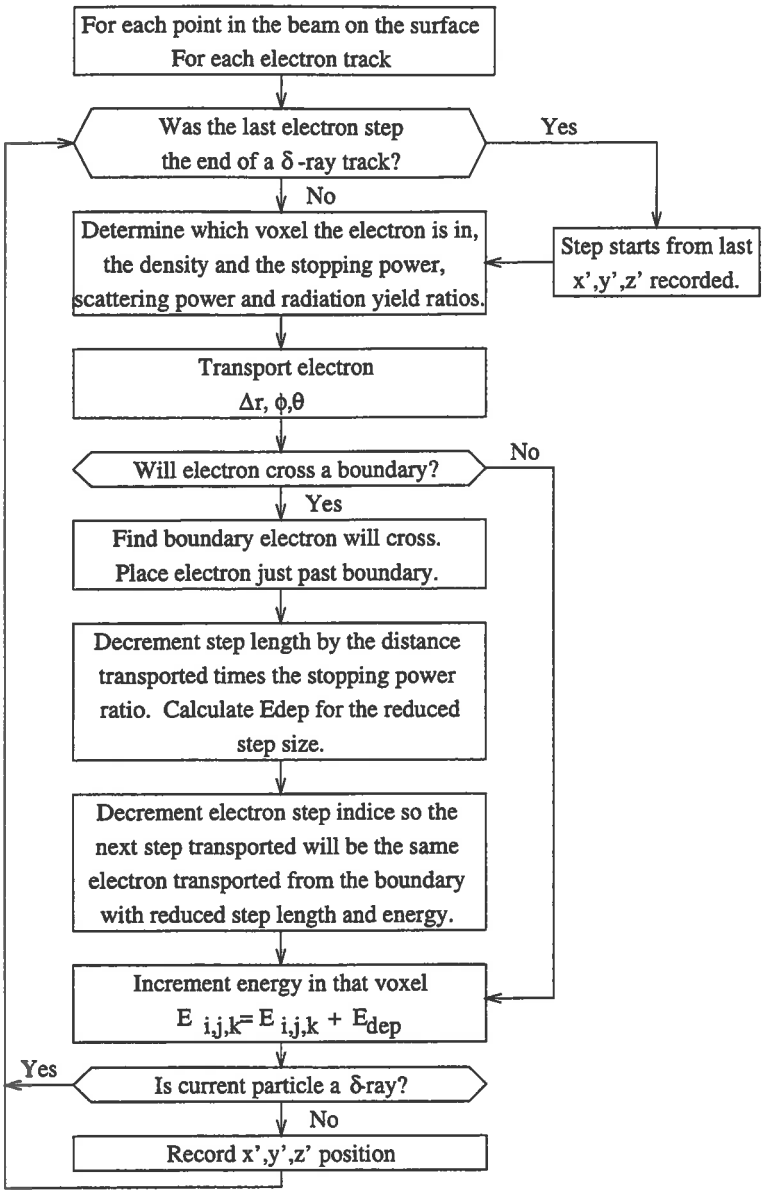

Figure 5.8: **The SMC electron transport algorithm used in the electron dose calculation.**

Boundary crossing

If the electron step is sufficiently long, or near enough to a boundary to cross into a different voxel, the SMC algorithm calculates which of the six voxel boundaries the electron will cross (or which boundary will be crossed first if the step is long enough to cross more than one boundary), and where on the boundary the electron will cross. The electron is then placed a small distance (eg. 10^{-6} cm) past the boundary crossing point and into the new voxel. The step length, Δr, and the energy deposited in that step, E_{dep}, are decremented by the ratio of the path length in the original voxel divided by Δr. The value of the energy decremented is deposited in the energy array for the original voxel. The same electron step is then transported as a new electron step, originating just past the boundary, with the same direction as previously, but a slightly smaller Δr and E_{dep}.

Bremsstrahlung radiation

Bremsstrahlung radiation produced in the tissue equivalent absorbing media (unlike that produced in the scattering foils) contributes a negligible amount to the total dose.[160] Therefore this radiation is not explicitly modeled in SMC, however if a superposition method (or another method) was used to calculate the incident photon contamination dose component, then bremsstrahlung produced in the absorbing medium could be also accounted for.

Dose equation

The electron dose is found by summing the energy deposited in voxel i, j, k from the steps q to q' of electron track m which fall in voxel i, j, k, from all of the tracks transported

from the surface in field XY,

$$D(i,j,k) = \frac{1}{\rho_{i,j,k}} \sum_{XY} \left(\sum_{m=0}^{M} \sum_{l=q}^{q'} \Delta E_{dep,m,l} \right) . \tag{5.4}$$

A description of the code used for electron beam SMC is found in appendix A.

Another way to calculate the dose distribution using SMC would be to pre-generate electron tracks for non-waterlike media such as bone, and if a track crosses a water-bone interface then switch from transporting an electron track generated in water, to that generated in bone at the appropriate energy (the angle of the track would need to be aligned as well). This method would result in more data generation and storage, and would not be flexible to use for any absorbing medium.

The SMC electron beam dose calculation algorithm can also be used to calculate dose by only taking account of the density of the irradiated medium, and not the composition. This option is performed by transporting the electron step by its original length divided by the density of the irradiated medium, as is the case with photon beam SMC. Such a method would save computation time, and be useful when a waterlike-composition medium (eg. soft tissue) is irradiated.

5.2.4 Monte Carlo

For comparison with SMC calculated dose distributions, Monte Carlo dose distributions were generated. The EGS4 Monte Carlo code[8] was used, with the PRESTA algorithm[157] turned on. AE was set to 0.521 MeV, AP to 0.010 MeV, ECUT to 0.611 MeV and PCUT to 0.050 MeV. Monodirectional incident electrons of energies 6 MeV and 15 MeV were transported through the various phantoms described below, and the subsequent energy deposited was recorded in a Cartesian array. At least 1×10^6 incident electrons were used

for each Monte Carlo simulation.

5.2.5 Phantoms

To test the agreement between SMC and Monte Carlo for a variety of geometries, several different phantoms were used. The materials used in the phantoms for the dose calculations were water, aluminium, lucite ($C_5H_8O_2$), lung analogue (water of density 0.30 gcm^{-3}) and ICRP bone.[159] Homogeneous water, aluminium and bone phantoms were used to determine the accuracy of the SMC technique. Also, heterogeneous phantoms composed of (i) a 4.0×12.0×0.5 cm^3 block of bone inserted at 2 cm depth in a water phantom (similar to that used by Shiu and Hogstrom[122]), (ii) a 2.0×2.0×1.0 cm^3 air cavity placed at 1 cm depth in a water phantom, and (iii) 1 cm of lucite above adjacent 1 cm slabs of lung and bone, below which is water (similar to the phantom used by Neuenschwander and Born[138]), were used to investigate the ability of SMC to predict dose in more complex geometries. All of the phantoms used were semi-infinite in extent.

5.3 Results

The EGS4 Monte Carlo code[8] has shown excellent agreement with experiment in a wide variety of physical situations.[60] Hence, to determine the accuracy of SMC calculated dose distributions, they are compared to EGS4 generated dose distributions. All of the results in this section pertain to absolute dose, given in dose per incident fluence (pGy cm^2), as calculated by Monte Carlo and SMC.

5.3.1 Pencil beam dose distributions in homogeneous phantoms

Isodose curves for a 15 MeV pencil beam were calculated using SMC and Monte Carlo in a water phantom with $0.1 \times 0.1 \times 0.1$ cm^3 voxels. The results are shown in Fig. 5.9. Good agreement is obtained between the SMC and Monte Carlo dose distributions, as expected, because the electron track kernel is generated in water. Figure 5.9 shows that 3000 electrons give a smooth dose distribution for all but the lowest isodose level, and hence that the neglect of bremsstrahlung transport in the SMC calculation is valid. The maximum difference found between the dose in any two corresponding voxels in the dose distribution was 5% of the maximum dose in the distributions.

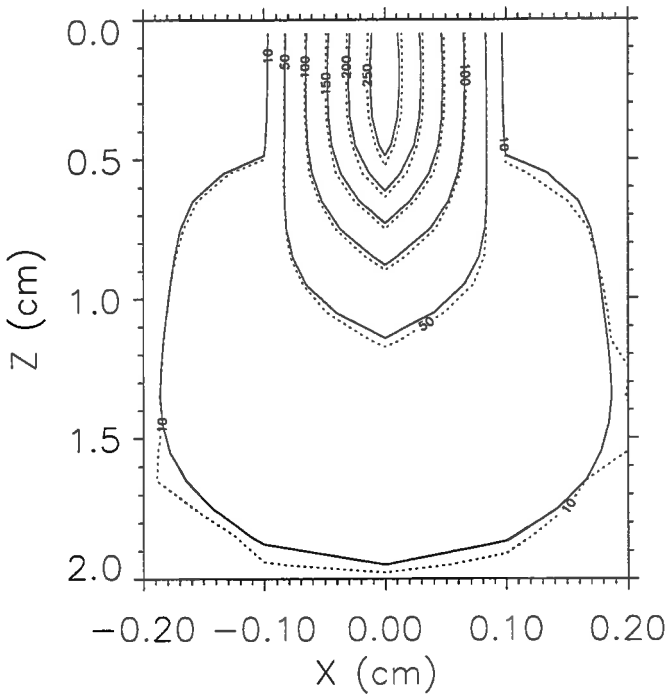

Figure 5.9: The dose distributions resulting from a 15 MeV pencil beam incident on a water phantom calculated using Monte Carlo (——) and SMC (- - -). The numbers on the isodose curves represent dose per incident fluence (pGy cm^2).

To test SMC in non-waterlike homogeneous phantoms, 15 MeV pencil beam dose distri-

butions ($0.1\times0.1\times0.1$ cm^3 voxels) were calculated using SMC and Monte Carlo in homogeneous bone and aluminium phantoms. The resultant isodose curves are shown in Fig. 5.10. Excellent agreement is shown between the SMC and Monte Carlo curves in this figure. The maximum difference found between the dose in any two corresponding voxels in the dose distributions were 2% and 1% of the maximum dose in the bone and aluminium phantoms respectively. Surprisingly, the differences between SMC and Monte Carlo in bone and aluminium were less than those found in water. However, the increased density in the bone and aluminium phantoms means that there are more electron steps within a voxel, and hence the statistics are improved.

To highlight the need to account for the different scattering power, stopping power and radiation yield in non-waterlike materials, an isodose plot of a 15 MeV pencil beam in aluminium is shown in Fig. 5.11, where the SMC curves were generated with the electron step lengths scaled by density alone, ie. no account was taken of the perturbation of the non-waterlike material. The SMC isodose curves show large discrepancies with the Monte Carlo generated isodose curves. The maximum difference found between the dose in any two corresponding voxels in the dose distribution was 28% of the maximum dose in the distributions (c.f. 1% when the scattering power, stopping power and radiation yield of the aluminium was taken account of).

To investigate SMC for a different electron energy, Monte Carlo and SMC isodose curves in bone and aluminium phantoms for a 6 MeV pencil beam were calculated using a $0.05\times0.05\times0.05$ cm^3 voxel size for the dose calculation array. The results are shown in Fig. 5.12. As with the 15 MeV distributions, good agreement was found between the SMC and Monte Carlo curves.

SMC electron transport is non-waterlike media makes assumptions about the relationship between the scattering, stopping and radiation yield characteristics of the non-waterlike media and water. Dose profiles in aluminium at 0.275 cm depth for the 6 MeV incident energy, and 0.75 cm depth for the 15 MeV incident energy, were generated using SMC and Monte Carlo. The depths were chosen as the widest points of the 10 pGy cm^2 isodose

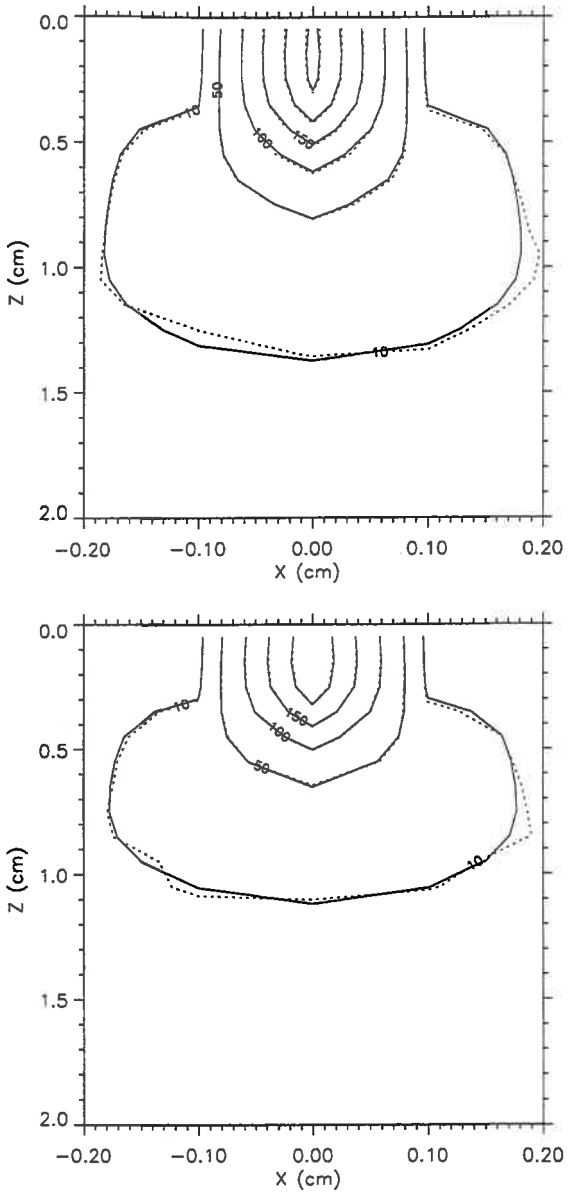

Figure 5.10: The dose distributions resulting from a 15 MeV pencil beam incident on a homogeneous bone phantom (top) and an aluminium phantom (bottom) calculated using Monte Carlo (——) and SMC (- - -).

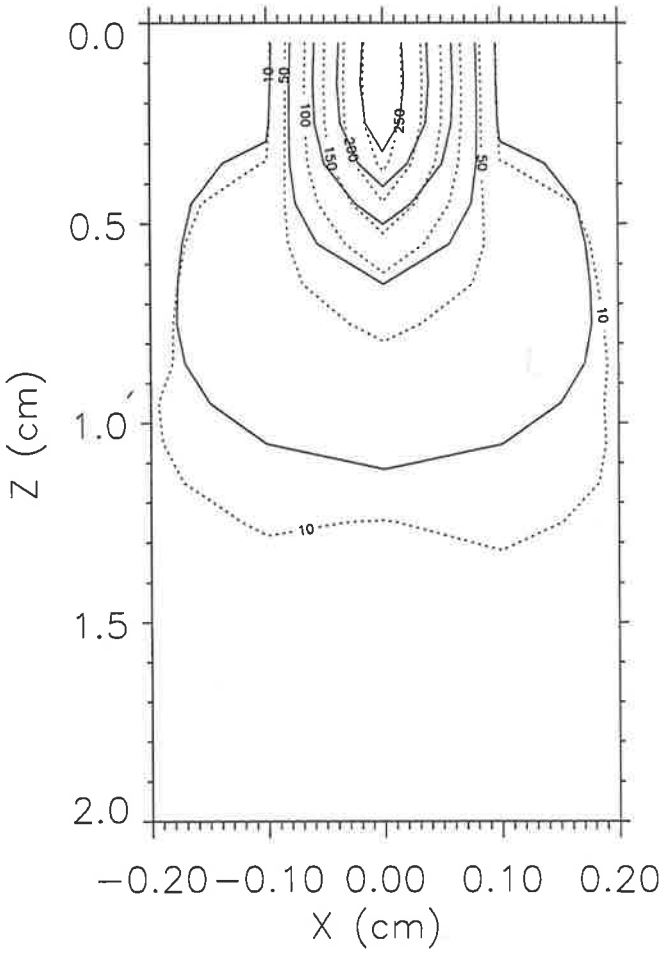

Figure 5.11: The dose distributions resulting from a 15 MeV pencil beam incident on an aluminium phantom calculated using Monte Carlo (——) and SMC scaled by density but employing the mass scattering power, stopping power and radiation yield values of water instead of aluminium (- - -).

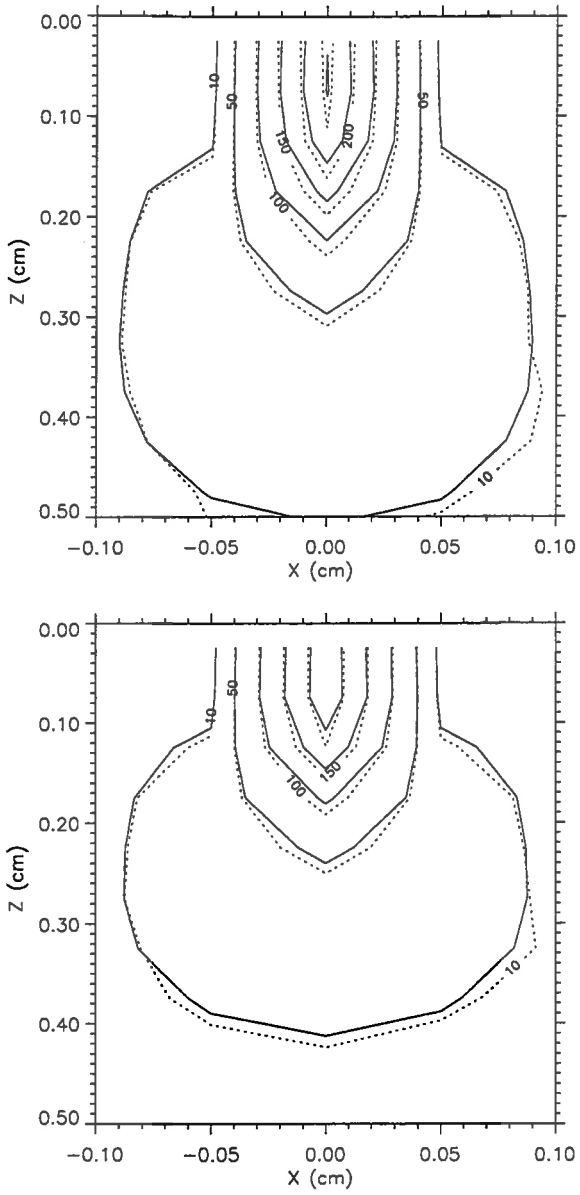

Figure 5.12: The dose distributions resulting from a 6 MeV pencil beam incident on a homogeneous bone phantom (top) and an aluminium phantom (bottom) calculated using Monte Carlo (——) and SMC (- - -).

curves in Figs. 5.12 and 5.10 respectively. These profiles are shown in Fig. 5.13 (the 15 MeV curve has been offset for clarity). The similarity in shape between the SMC and Monte Carlo profile curves indicates the ability of SMC to reproduce the large angle scattering in higher atomic number media.

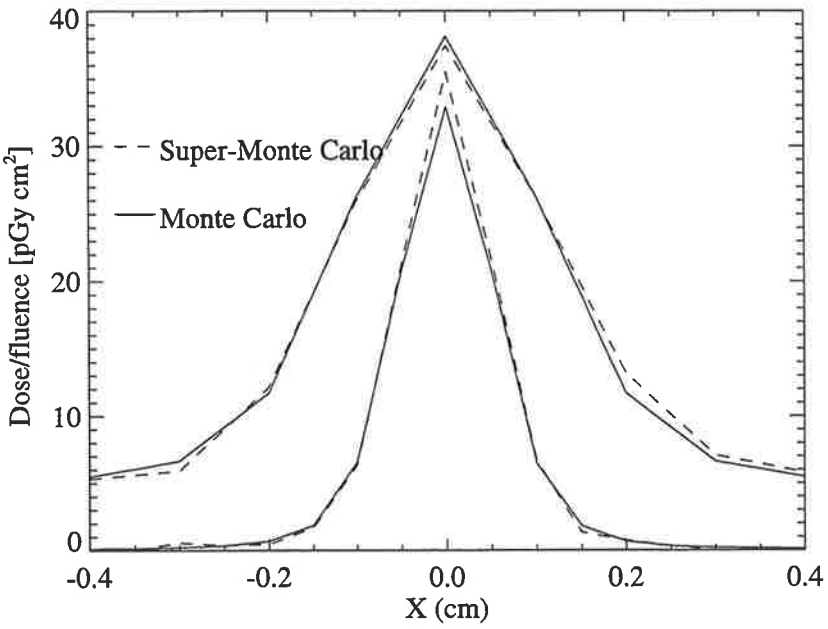

Figure 5.13: Profile curves in aluminium at 0.175 cm depth in aluminium for a 6 MeV pencil beam (narrow curves) and at 1.05 cm depth for a 15 MeV pencil beam (wider curves) calculated using Monte Carlo (——) and SMC (- - -). The 15 MeV dose profile curve has been offset for clarity.

5.3.2 Broad beam dose distributions in water

The first requirement of a dose calculation algorithm is the ability to accurately predict the dose to water for an incident broad beam. In SMC the dose contribution from the electron track kernel at each surface voxel is summed to give a broad beam dose distribution.

SMC and Monte Carlo curves for a 6×6 cm^2 field at both 6 MeV and 15 MeV beam energies with a 0.5×0.5×0.25 cm^3 dose scoring array are shown in Fig. 5.14. These curves show that SMC can accurately reproduce a dose distribution in a water phantom.

5.3.3 Broad beam dose distributions in heterogeneous phantoms

To investigate the ability of SMC to predict dose in phantoms containing inhomogeneities which perturb the dose distribution, three different phantoms were used.

a. Bone block phantom. Isodose distributions (15 MeV, 10×10 cm^2 field, 0.5×0.5×0.25 cm^3 scoring array) calculated using SMC and Monte Carlo in a water phantom with a bone block inserted at 2 cm depth are shown in Fig. 5.15. The SMC isodose curves show good general consistency with the Monte Carlo curves, including the prediction of the increase in dose downstream of the bone block. The maximum difference between dose in any two corresponding voxels in the Monte Carlo and SMC distributions is 6% of the maximum dose.

A depth dose curve at central axis, and a dose profile curve at 2.9 cm depth in the bone block phantom (Fig. 5.16), show that SMC accounts for the perturbation of the dose distribution due to the bone block, however there is a slight (5%) underprediction of the dose within the bone block, and just beneath the bone block.

b. Air cavity phantom. As electron beams are often applied in head and neck treatments, the dose calculation algorithm must be capable of calculating dose accurately near air cavities. SMC and Monte Carlo were used to transport electrons through an air cavity phantom. The results for a 6×6 cm^2 field for both 6 and 15 MeV incident electron energies for a 0.5×0.5×0.25 cm^3 scoring array are shown in Fig. 5.17. The maximum difference between dose in any two corresponding voxels (ignoring the dose differences

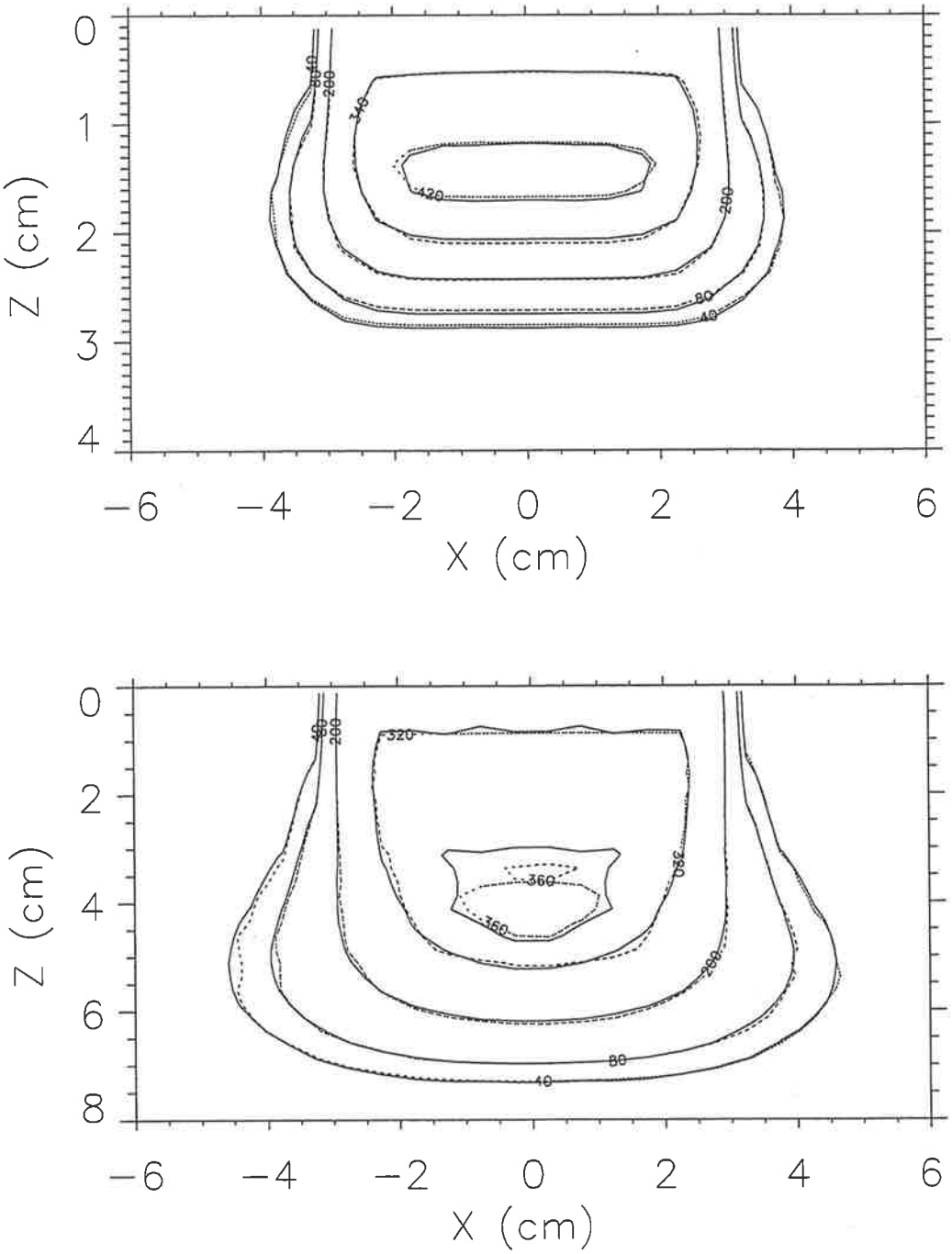

Figure 5.14: Isodose curves in water for a 6×6 cm^2 electron beam, for 6 MeV electrons (top) and 15 MeV electrons (bottom). Monte Carlo (——) and SMC (- - -) distributions are shown.

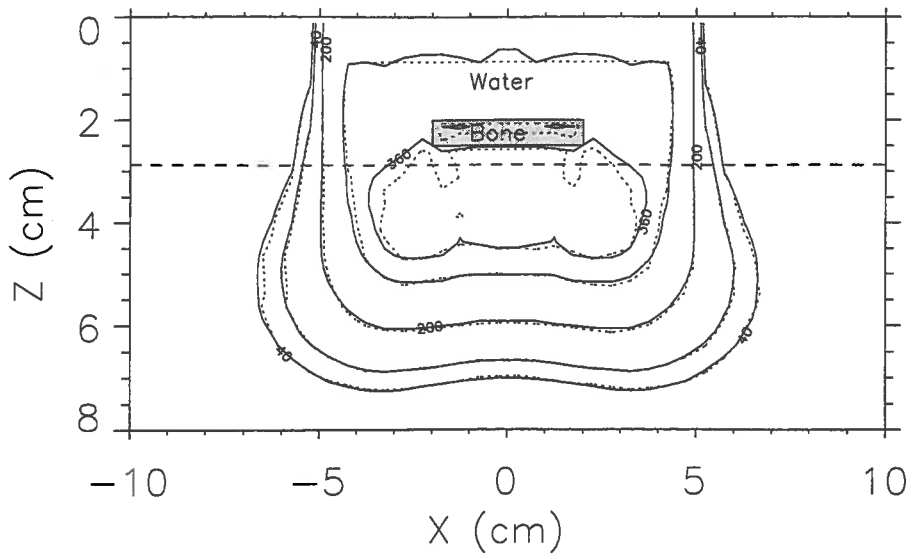

Figure 5.15: Isodose curves in a water phantom with a bone block for a 10×10 cm^2, 15 MeV parallel electron beam calculated using Monte Carlo (——) and SMC (- - -). The dashed lines at 2.9 cm depth indicates the depth of the following dose profile curve.

in the air cavity itself) in the Monte Carlo and SMC distributions is 5% of the maximum dose for the 6 MeV energy, and 5% of the maximum dose for the 15 MeV energy.

Depth dose and dose profile curves in the air cavity phantom for both 6 and 15 MeV energies were calculated using both SMC and Monte Carlo. These curves are displayed in Fig. 5.18 (the 15 MeV profile has been offset for clarity).

c. Multiblock phantom. Four different material types were used to construct a multiblock phantom, in which the dose distribution from a 15 MeV 6×6 cm^2 field (0.5×0.5×0.25 cm^3 scoring array) was calculated using both SMC and Monte Carlo. These isodose curves are shown in Fig. 5.19. The agreement between isodose curves in the lucite-lung-bone-water phantom of Fig. 5.19 highlights the ability of SMC to accurately calculate dose in complex geometries. The increase in dose on the lung side of the figure due to the increased scatter from the bone is predicted well by SMC. The maximum difference between dose in any two corresponding voxels in the Monte Carlo and SMC distributions is 5% of the maximum

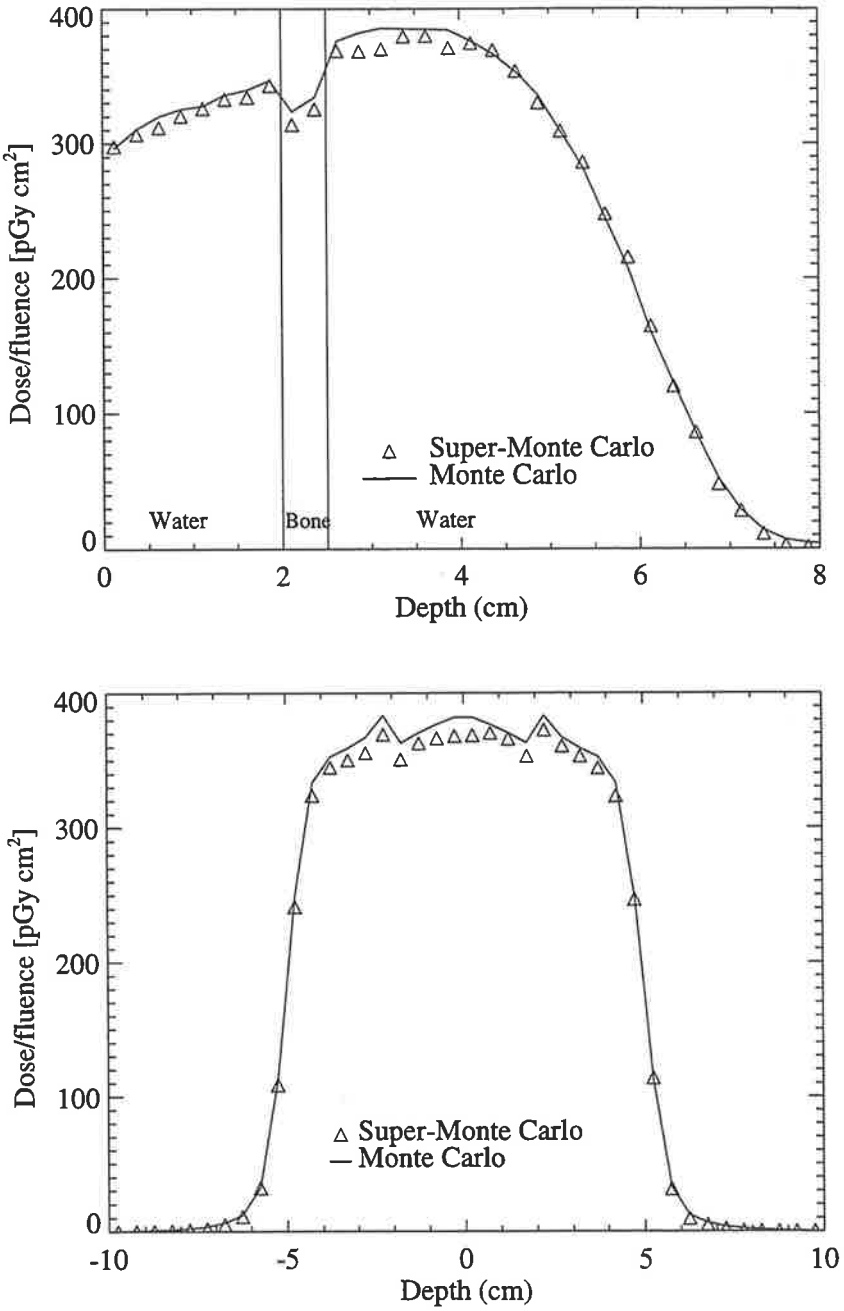

Figure 5.16: Central axis depth dose curves (top) and dose profile curves at 2.9 cm depth (bottom) in a bone block/water phantom for a 10×10 cm^2, 15 MeV parallel electron beam calculated using Monte Carlo (——) and SMC (△). The SMC statistical uncertainty is ±1%.

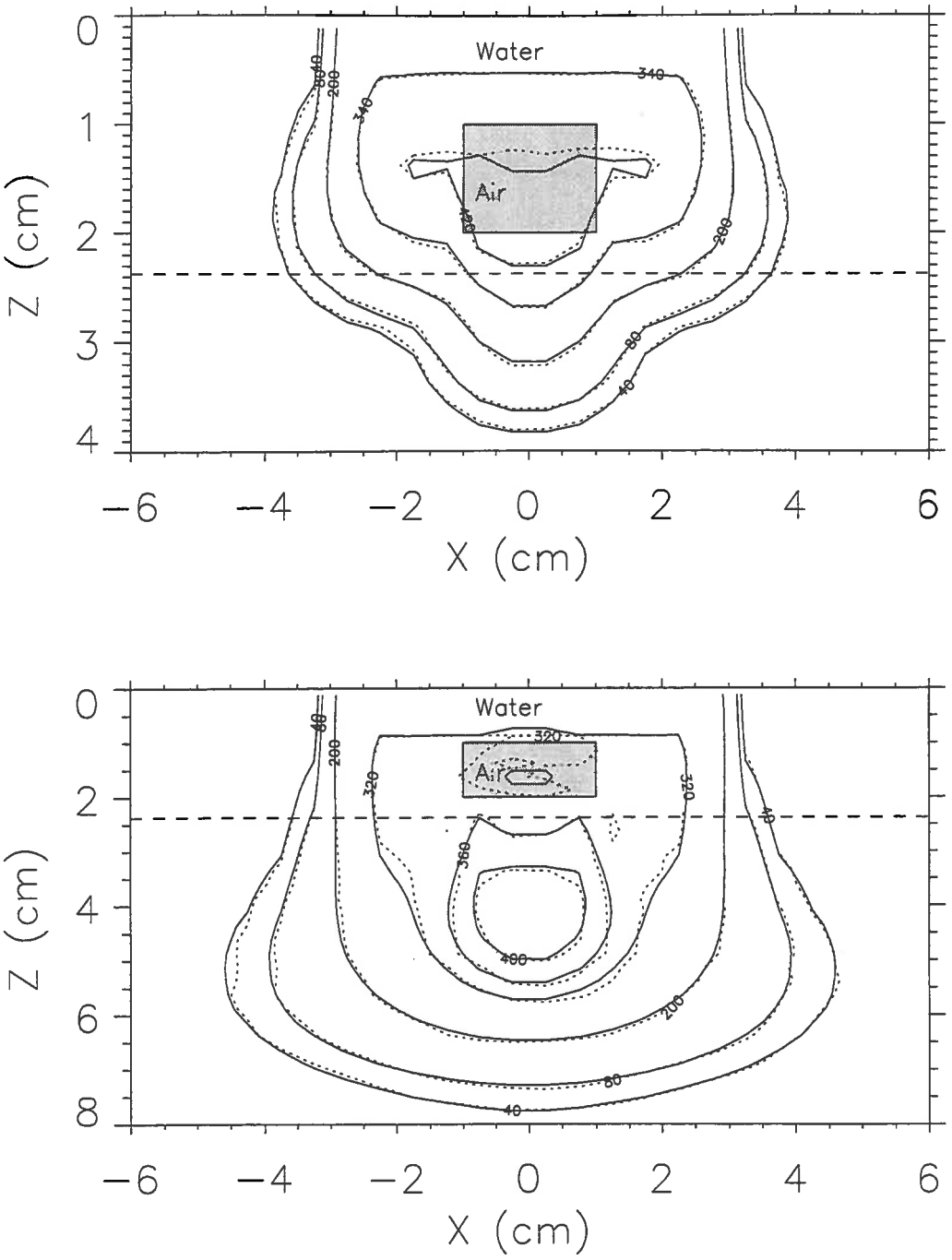

Figure 5.17: Isodose curves in an air cavity phantom for a 6×6 cm^2 electron beam, for 6 MeV electrons (top) and 15 MeV electrons (bottom). Monte Carlo (——) and SMC (- - -) distributions are shown. The dashed line indicates the depth of the following dose profile curve.

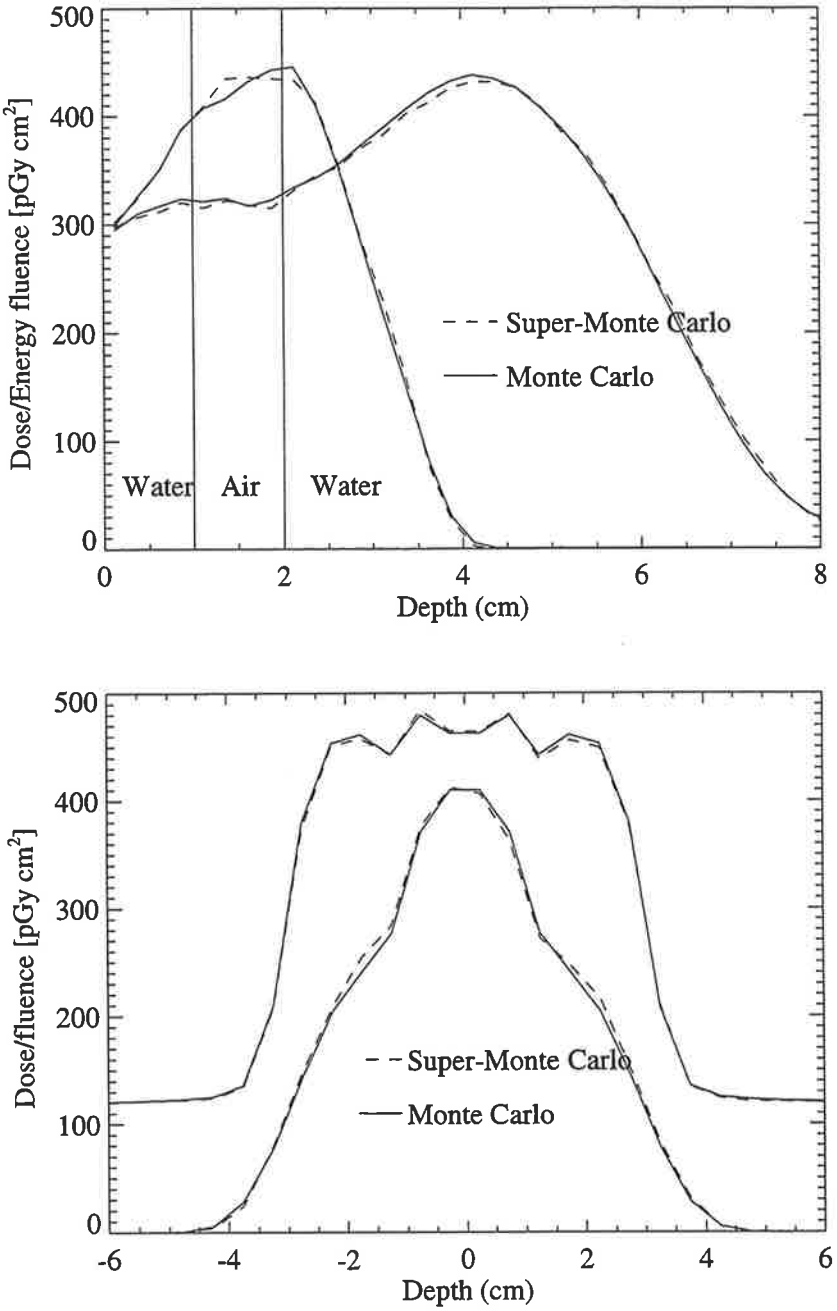

Figure 5.18: Central axis depth dose curves (top) and dose profile curves at 2.375 cm depth (bottom) in an air cavity phantom for 6×6 cm^2, 6 and 15 MeV parallel electron beams calculated using Monte Carlo (——) and SMC (- - -). The 15 MeV dose profile curve has been offset for clarity. The SMC statistical uncertainty is ±1%.

dose.

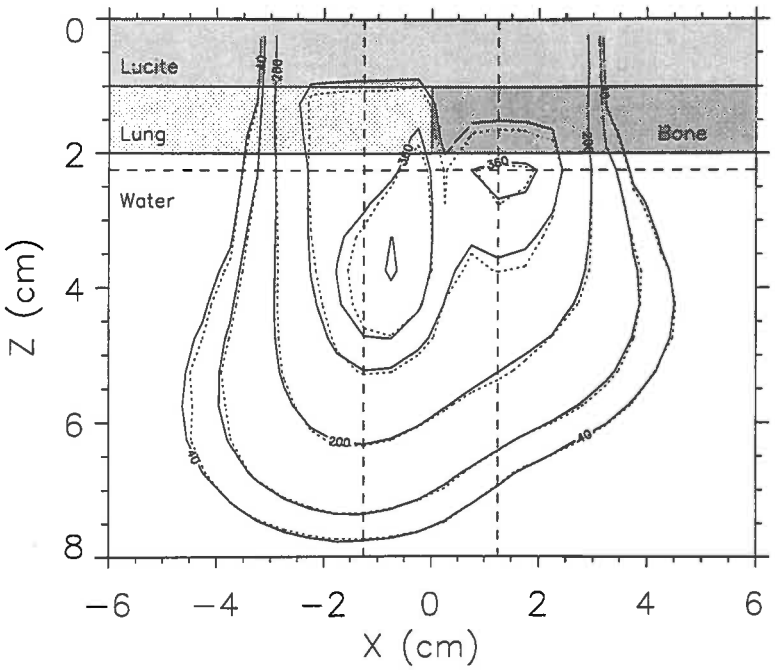

Figure 5.19: Isodose curves in a heterogeneous phantom composed of lucite, lung, bone and water for a 6×6 cm^2, 15 MeV parallel electron beam calculated using Monte Carlo (——) and SMC (- - -). The dashed lines at ± 1.25 cm off axis, and at 2.25 cm depth, indicates the position of the following depth dose and dose profile curves respectively.

Depth dose curves on both sides of the central axis (at ± 1.25 cm), and profile curves at 2.25 cm depth are shown in Fig. 5.20. SMC calculates the increase in dose immediately beneath the bone. The dose profile curves show the disequilibrium at the bone/lung interface due to electrons scattered laterally from underneath the bone not being replaced by electrons scattering laterally from beneath the lung.

5.3.4 Statistics and computation time

In EGS4, the standard deviation between corresponding voxels in the N (N=5) different batchs is calculated to obtain the statistical uncertainty of the sum of the batches, σ_{sum},

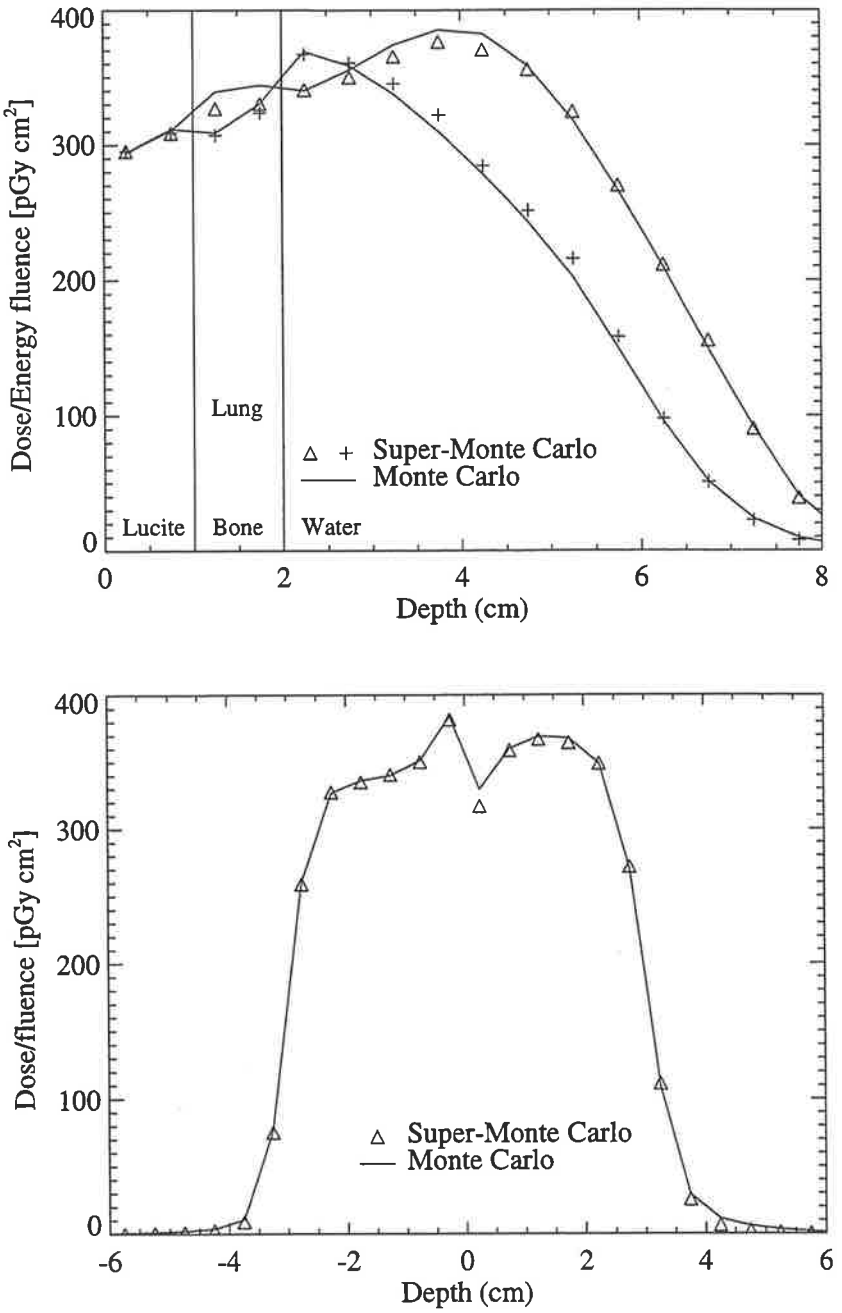

Figure 5.20: Off axis depth dose curves (top) and dose profile curves at 2.25 cm depth (bottom) in a phantom composed of lucite, lung analogue, bone analogue and water for a 6×6 cm^2, 15 MeV parallel electron beam calculated using Monte Carlo (——) and SMC ($\triangle$ at x = -1.25 cm), (+ at x = +1.25 cm for the depth dose curves, and + for the dose profile curve). The SMC statistical uncertainty is ±1%.

ie.

$$\sigma_{sum} = \frac{1}{\sqrt{N}}\sqrt{\frac{\sum_{i=1}^{N}(x_i - \overline{x})}{N-1}}. \tag{5.5}$$

The same calculation was performed to obtain the SMC statistical uncertainty, by calculating dose distributions using different electron track kernels, each containing 3000/N electrons. The statistical analysis was performed for both pencil and broad 15 MeV beams incident on a water phantom.

All the computation times given below were obtained using a DECalpha 3600 175 MHz workstation.

a. Pencil beam distributions. Using a 0.1×0.1×0.1 cm^2 dose scoring array for the pencil beam dose distribution, the calculated uncertainty in the voxels containing the highest doses for a SMC kernel containing 3000 electrons was 0.6%. As expected, a Monte Carlo dose distribution using 3000 incident electrons yielded a similar uncertainty (0.7%).

The calculation time for the SMC pencil beam distribution (90s) was slower than that for the Monte Carlo distribution (40s). The increased computation time for the SMC distribution is probably because large arrays (>10 Mb) are initialised, but used only once.

b. Broad beam distributions. For a 0.5×0.5×0.25 cm^3 dose scoring array for a 6×6 cm^2 broad beam, the calculated uncertainty (using SMC) in the voxels containing the highest doses was 0.9%. The number of incident electrons transported to obtain this uncertainty was 3000 × the number of voxels within the field = 0.43 million. To obtain the same uncertainty using Monte Carlo required 1.8 million incident electrons. The difference in the number of electrons needed to obtain the same uncertainty is because of the systematic transport of the same number of electrons in the same way from each voxel in SMC, eliminating the uncertainty in interaction position.

The computation time for the SMC broad beam calculation (49 minutes) was over nine

times less than that required to obtain the same level of uncertainty in the Monte Carlo simulation (450 minutes). The difference in the relative speeds of the two algorithms between the pencil beam and broad beam cases can be explained by the multiple use of the large arrays in the SMC broad beam simulation (which are only used once for the SMC pencil beam calculation), and that SMC doesn't need to use as many electrons as a full Monte Carlo simulation to obtain the same uncertainty in the broad beam case. By optimising the electron track kernel, the speed difference between SMC and Monte Carlo is likely to significantly increase.

5.4 Conclusion

The SMC method of dose calculation agrees well with Monte Carlo dose calculation results in a variety phantoms for 6 and 15 MeV electron beam energies.

SMC has several advantages over pencil beam methods: (i) scattering is not approximated by a Gaussian lateral distribution, (ii) the 'semi-infinite slab' approximation[143] is not used (the medium is not treated as slabs by each incident beam element), (iii) the atomic number variation of the absorbing medium is accounted for, (iv) the dose calculation is three dimensional and (v) the absolute dose is calculated.

A 15 MeV, 6×6 cm^2 field requires approximately 50 minutes of CPU time on a DECalpha platform, which is a 9-fold increase in speed over a full Monte Carlo simulation (to obtain the same statistical accuracy). The SMC method is not as fast as the Voxel-based Monte Carlo method[110] which calculates dose up to 35 times the speed of a full Monte Carlo simulation, however SMC has the potential for a large speed increase. Optimisation of the number of the electron tracks in the kernel, the track generation parameters AE, AP and ECUT, and pre-processing of the electron track kernel to join smaller steps together to form larger steps will significantly reduce the necessary computation time.

The SMC method has been applied to x-ray beams in chapter 4 and hence SMC is a unified 3-D electron/photon beam dose calculation algorithm.

Further development of the SMC algorithm, such as the inclusion of an accurate description of the treatment beam, is needed before this method could be used clinically. However, it is envisaged that with algorithm optimisation, and on a more powerful platform, SMC could be a clinically realistic dose calculation tool.

Chapter 6

Conclusions, Discussion and Future Research

6.1 Conclusions

The aim of this research was to produce a dose calculation algorithm which agrees with experimentally measured dose distributions to within 2% in arbitrary geometries, and is computationally viable in a clinical situation.

A method of calculating the X-ray primary dose component in a superposition calculation by invoking Fermi-Eyges electron scattering theory (FE scaling superposition) has been proposed. This method achieves an accuracy of better than 2.5% in the geometries tested, with a 3-fold increase in computation time over a standard superposition algorithm. FE scaling superposition nearly achieves the required accuracy for dose calculation (in the geometries tested), with only a small increase in the computation time for the total dose

compared to a standard superposition calculation.

Limitations of the FE scaling method are that it only improves standard superposition in the direction of the beam axis, uses zero initial scattering moments at the interaction site, and does not account for different atomic number materials.

Combining superposition with pre-generated Monte Carlo electron track kernels has yielded an X-ray dose calculation tool, Super-Monte Carlo (SMC), that is accurate to within 1.5% in dose calculation for the geometries investigated. The advantage of SMC over superposition is significant for small fields and high energies at interfaces of different density (where lateral electronic disequilibrium exists), as the interface problem of the rectilinear scaling method in the primary dose superposition calculation is eliminated. X-ray SMC achieves the required accuracy in a dose calculation algorithm, however in its present form it is too computationally intensive to use clinically (SMC is approximately 20 times faster than Monte Carlo, but 15 times slower than superposition).

X-ray SMC does not yet account for different atomic number materials in the absorbing medium, nor does it account for the hardening in the spectrum of the secondary electrons with depth (the hardening of the primary photon beam is accounted for as in standard superposition).

When applied to electron beam dose calculation, the SMC algorithm yields results consistent with Monte Carlo for a variety of heterogeneous phantoms of water and non-waterlike composition. SMC has several advantages over pencil beam methods: (i) scattering is not approximated by a Gaussian lateral distribution, (ii) the semi-infinite slab approximation is not used (the medium is not treated as slabs by each incident beam element), (iii) the atomic number variation of the absorbing medium is accounted for, (iv) the calculation is three dimensional and (v) the absolute dose is calculated. A 15 MeV, 6×6 cm^2 field requires approximately 50 minutes of CPU time on a DECalpha platform.

Woo and Cunningham[151] state that the concept of a unified electron/photon algorithm

is both logical and useful, as the mechanism of dose delivery is essentially the same, i.e. via electron energy deposition. The emphasis on the similarity between the two methods is becoming more necessary, since in high-energy photon beams the accurate transport of long-range secondary electrons becomes important. The lack of electronic equilibrium thus becomes more acute, and detailed electron transport has to be considered. The SMC method outlined in this thesis is a unified photon/electron dose calculation algorithm, and could also be extended to other incident particles such as protons and neutrons.

Algorithms of near-Monte Carlo accuracy but much faster computation time will be advantageous even when computer hardware is at a point where full Monte Carlo dose calculations are possible, as the increase in speed with the faster algorithm means that more rigorous optimisation and inverse planning methods can be used for the same calculation time as a basic Monte Carlo calculation.

6.2 Extension of the current research

Further development of the FE scaling superposition and SMC algorithms, such as the inclusion of an accurate description of the clinical beam (the same information required as input to commercially available superposition algorithms[101, 102]), is needed before these methods could be used clinically. However, it is envisaged that with algorithm optimisation, and on a more powerful platform, FE scaling superposition and SMC could be clinically realistic dose calculation tools.

A logical extension of the FE scaling algorithm is to incorporate this technique into a collapsed cone convolution method, where energy in each cone can be redistributed between cones depending on the composition of the media the cones are passing through, thus applying FE scaling to full 3-D kernel scaling. FE scaling could also be further developed to include the effects of different atomic number materials in the absorbing

medium, include non-zero initial electron angular distributions at the interaction site, and use an energy dependent scattering power.

To account for atomic number effects in photon SMC, a similar method to that used for electron SMC could be incorporated. Inclusion of such a method is likely to produce good results, at the expense of computation time. The hardening of the secondary electron spectrum with depth could be accounted for normalising the total energy in the steps to collision kerma, and using the collision kerma instead of terma in the superposition calculation.[44, 99]

To optimise photon and electron SMC the electron track kernels need to be examined for maximum efficiency. Increased efficiency could be achieved by condensing a number of small steps into a few bigger steps, determining the optimal number of electron track histories for each kernel, and by joining tracks (or parts of tracks) which are spatially similar into one track with increased weight.

6.3 Application of the current research

Apart from the benefits of increased accuracy in the dose calculation for treatment planning today, accurate dose calculation algorithms such as those presented in this thesis will be essential for maximising the benefits of the technology of tomorrow (a method which is currently too slow computationally is sure to be sufficiently fast in the future). There has been much research published about the use of treatment optimisation and conformal therapy to obtain maximal tumour dose coverage with minimal normal tissue dose.[161, 162, 163, 49, 164, 165, 166] Once there is confidence that the dose delivered during a radiotherapy treatment is what was planned, then patient survival data can be used to obtain accurate in-vivo radiobiological cell responses. Hence radiobiological models[167, 168, 169, 170, 171, 40] can be used to provide meaningful input to both the

optimisation procedure and to predict treatment outcomes.

6.4 Epilogue

Future clinically used radiation therapy beam planning algorithms are likely to calculate dose to such an accuracy that any errors will be much smaller in magnitude than those brought about by other uncertainties introduced in the treatment, such as the calibration of the treatment machine, characterisation of the radiotherapy beams, day-to-day positioning of the patient and the constancy of the patient's geometry.[4] It is hoped that with continual improvement in linear accelerator design and other technology, as well as ongoing oncologist, radiation therapist and physicist staff training, that these errors will also be reduced.

These developments will (statistically) lead to increased local tumour control and decreased normal tissue complications for improved levels of patient care and treatment success. A challenge for us all!

Appendix A

Users Manual for the Fermi-Eyges Scaling Convolution and Super-Monte Carlo Suite of Software C_CONVOLUTION

Paul J. Keall — Department of Medical Physics, Royal Adelaide Hospital
North Terrace, Adelaide, SA 5000
Australia

and — Department of Physics and Mathematical Physics
University of Adelaide, Adelaide, SA 5005
Australia

Ph: +61 8 222 5658 Fax: +61 8 222 5937
Email: pkeall@physics.adelaide.edu.au

March 1996

Based on the s_superposition software written by David C. Murray and Peter W. Hoban.

A.1 Introduction

The motivation for producing this code was to improve the convolution technique of dose calculation at interfaces of different density where electron scattering is not explicitly accounted for. A balance has been struck between accuracy and computation time. The code is written in the C programming language, and resides in /remote/mortis/pkeall/c_conv.

In its current form, this code can calculate photon beam dose distributions in a Cartesian array using convolution, Fermi-Eyges (FE) scaling convolution and Super-Monte Carlo (SMC). Electron beam dose distributions can be calculated using SMC.

Monte Carlo generated data is needed for both the FE scaling and standard superposition methods and the SMC method of dose calculation. Monte Carlo generated kernels for 6 MV, 10 MV and 18 MV beam energies are found in directories pkeall/EGS4/poly, /EGS4/10MV and /EGS4/new18 respectively. Monte Carlo generated electron track histories are found in the directory pkeall/REDUCE. The format of these data sets are discussed in sections A.1.1 and A.1.2 if the user wishes to make energy deposition kernels or electron track kernels for different beam energies.

Anyone looking closely at this set of programs will notice that I am a physicist and not a computer programmer. However, I have included this documentation, and comments within the code for anyone wanting to use this system. Suggestions, improvements, comments or queries about any part of this code are very welcome.

As stated earlier, this code is based on the s_superposition software written by David C. Murray and Peter W. Hoban at the University of Waikato. The convolution method is a polyenergetic method (and not ideal as making kernels from monoenergetic components gives the user much more flexibility). For an understanding of the standard superposition/convolution method used in this package see:

P. W. Hoban, D. C. Murray, P. E. Metcalfe and W. H. Round 'Superposition dose calculation in lung for 10 MV photons', *Aust. Phys. Eng. Sci. Med.* **13**(2) 81-92, 1990.

P. W. Hoban *Lateral Electron Disequilibrium in Radiotherapy Treatment Planning*, Ph.D. Thesis, University of Waikato, 1991.

D. C. Murray *The Application of Parallel Processing to Radiotherapy Dose Computation*, Ph.D. Thesis, University of Waikato, 1991.

P. W. Hoban, D. C. Murray and W. H. Round 'Photon beam convolution using polyenergetic energy deposition kernels', *Phys. Med. Biol.* **39** 669-685, 1994.

A.1.1 Fermi-Eyges scaling convolution

The FE convolution method of dose calculation improves standard convolution in the direction of the beam axis by incorporating FE electron scattering theory into the rectilinear density scaling routine, thus accounting for the density distribution between the interaction and deposition sites, not just the average density. The main programming difference between FE and rectilinear scaling is found in the subprogram *s_fe_trace* of program *c_calc_dose.c*. Further work using a collapsed cone approach needs to be done to make this a full 3-D scaling method. Anyone interested?

Format of convolution kernel data files

The convolution kernel data files for 6, 10 and 18 MV beam energies are found in directories pkeall/EGS4/poly, /EGS4/10MV and /EGS4/new18 respectively. For users wishing to create their own data files the current format (all ascii) is:

x-voxel number, y-voxel number, z-voxel number

x-voxel width (cm), y-voxel width, z-voxel width

z-voxel depth of interaction

kernel values (fractional energy deposition)

:

:

The kernel values are arranged such that the x-values are output for every y-value, then for every z-value.

A new *kernel_data_file* containing spectra and kernel file names will need to be created for each new spectrum. The kernel data files contain:

the number of spectral components

the upper energy limit of each energy bin

the relative weight of each spectral component (number fluence not energy fluence)

the attenuation coefficient for each spectral component (to calculate terma)

the energy absorption coefficient for each spectral component (to calculate kerma)

the number of different density kernels

the density that these kernels were created in (current kernels were all created in waterlike media)

the filename of the primary energy deposition kernels corresponding to each density

the filename of the scattered energy deposition kernels corresponding to each density

A.1.2 Super-Monte Carlo

The SMC method was originally developed as a photon code, however shows promise as an electron dose calculation algorithm, and routines have been included to account for varying atomic number in the absorbing medium (which can be applied to both photon and electron codes).

In SMC, the terma (or incident fluence in the electron beam case) is convolved with electron track kernels (cf. convolution where terma is convolved with energy deposition kernels). Each step of each electron track is explicitly transported through the medium.

Format of electron track data files

The electron track data files are found in the directory pkeall/REDUCE. These files take up a lot of memory and it is advisable to only store the kernel you are using at the current time (they only take a matter of minutes to create). For users wishing to create their own data files the current format (all ascii) is:

0.00 0.00 0.00 0.00 0.00 0	indicates a new track is to follow
E x y z E_{dep} Flag	format of each step of each electron track. E is the kinetic energy of the electron (or positron), x, y and z are the positions relative to the interaction point, E_{dep} is the energy deposited in the next electron step, and Flag indicates whether the current particle is a δ-ray or the primary electron eg. 0.003044 -0.000197 0.127237 0.7122E-01 1
99.99 99.99 99.99 99.99	indicates the end of the data set

Note: an understanding of the FE scaling and SMC physics behind this package can be found in:

P.J. Keall and P.W. Hoban 'Accounting for primary electron scatter in X-ray beam convolution calculations', *Med. Phys.* **22**(9) 1414-1418, 1995.

P.J. Keall and P.W. Hoban 'An X-ray dose calculation method combining superposition and explicit transport of pre-generated Monte Carlo electron track histories', *Med. Phys.* (In press) 1996.

P.J. Keall and P.W. Hoban 'Super-Monte Carlo: An accurate 3-D electron beam dose calculation algorithm', submitted to *Med. Phys.* 1995.

Copies of these papers (as well as the code) are available upon request.

A.2 Description of programs

A.2.1 c_input.h

c_input.h includes all the options that can be changed at run time. Beam size, electron option, path length correction option, dose calculation array size etc are all included in this file. *ahn.h, mmc.h, redef.h* and *one_block.h* are all examples. These options are listed below:

#define XBEAM_MIN 15	first x-voxel in field (grid indices start at 0)
#define XBEAM_MAX 25	first x-voxel out of field
#define YBEAM_MIN 15	first y-voxel in field
#define YBEAM_MAX 25	first x-voxel in field
#define NUM_ELEC 1	the number of times each electron is to be transported (1-4)
#define KERNEL FALSE	don't generate a dose distribution for a single interaction site
#define ELECTRON FALSE	photon beam
#define DIVERGING FALSE	parallel field
#define PATH_LENGTH_CORR TRUE	account for path length correction across voxel boundaries of different density

```
#define ACCOUNT_FOR_SCATTER FALSE      don't account for change in scattering angle in
                                       media of different scattering power
#define ACCOUNT_FOR_STOP FALSE         don't account for change in stopping power in
                                       media of different composition
#define ACCOUNT_FOR_RAD_YIELD FALSE    don't account for change in energy given to
                                       bremsstrahlung in media of different composi-
                                       tion
#define PRIMARY_CONV FALSE             don't use convolution calculation for primary dos
#define PRIMARY_TRACKS TRUE            use SMC calculation for primary dose
#define SCATTERED FALSE                don't include scattered dose
#define BEAM_HARD_CORR FALSE           don't account for beam hardening
#define SSD 100.0                      SSD (cm). Irrelevant for parallel field
#define GRID_X_NUMBER 40               number of x-voxels
#define GRID_Y_NUMBER 40               number of y-voxels
#define GRID_Z_NUMBER 40               number of z-voxels
#define X_SIZE 0.5                     size of voxels in x-direction (cm)
#define INV_X_SIZE 2.0                 1/size of voxels in x-direction (cm)
#define Y_SIZE 0.5                     size of voxels in y-direction (cm)
#define INV_Y_SIZE 2.0                 1/size of voxels in y-direction (cm)
#define Z_SIZE 0.5                     size of voxels in z-direction (cm)
#define INV_Z_SIZE 2.0                 1/size of voxels in z-direction (cm)
#define BASE_DENSITY 1.0               density of phantom
#define BASE_MATERIAL WATER            phantom material. Other options are LN4,
                                       BONE, ALUMINIUM and LUCITE
#define BLOCK_1 TRUE                   include a block
#define BLOCK_1_MATERIAL WATER         block material
#define BLOCK_DENSITY_1 0.30           block density
#define BLOCK_XSTART_1 0               first block voxel in x-direction
#define BLOCK_XTHICK_1 40              number of block voxels in x-direction
#define BLOCK_YSTART_1 0               first block voxel in y-direction
#define BLOCK_YTHICK_1 40              number of block voxels in y-direction
#define BLOCK_ZSTART_1 8               first block voxel in z-direction
#define BLOCK_ZTHICK_1 16              number of block voxels in z-direction
#define BLOCK_2 FALSE                  don't include a second block
#define BLOCK_3 FALSE                  don't include a third block
#define TRACK_DATA_FILE "track_6.dat"  file with electron track data
#define KERNEL_DATA_FILE "kernel_data_6mv.dat"
                                       file with attenuation coefficients, beam spectra
                                       and positions of convolution kernels
#define TOTALMEV 489.3072              total primary energy (MeV) in electron track dat
#define MAX_NO_TRACKS 6000             maximum number of electron tracks to be trans-
                                       ported from each voxel
#define MAX_TRACK_LENGTH 600           maximum length of electron tracks
#define X_INT_SITES 1                  number of particle interaction sites in each voxel
                                       in the x-direction
#define Y_INT_SITES 1                  number of particle interaction sites in each voxel
                                       in the y-direction
#define Z_INT_SITES 1                  number of particle interaction sites in each voxel
                                       in the z-direction
```

#define SCALING_TYPE Z_SCALING	type of scaling to use for the convolution calculation. Other options are NO_SCALING, FE_SCALING and RAY_TRACE

If the header (.h) or c files (.c) are altered then the code needs to be compiled before running. Compilation is achieved by entering make. To run the code enter c_conv.

A.2.2 c_convolution.h

c_convolution.h includes the structures TRACK, POINT, GRID etc., and other information such as stopping power ratios and scattering power ratios required to run the code.

A.2.3 c_main.c

c_main.c initiates GRIDs and other structures, and controls the algorithm. All other programs are called from, and return to *c_main.c*.

A.2.4 c_input_kernels.c

c_input_kernels.c reads in the appropriate kernel information necessary for the terma calculation such as spectra energy and weight components, and attenuation coefficient values from the *kernel_data_file* to structure kernel. Also the kernels for each density are read into structure EDKS.

A.2.5 c_elec_dens_grid.c

c_elec_dens_grid.c assigns density values to GRID elec_density and inv_elec_density, as well as assigning material types in GRID block and material values in structure DATA. The phantom geometry and composition are defined by the user in *c_input.h*.

A.2.6 c_calc_terma.c

c_calc_terma.c calculates the radiological depth, terma and kerma grids for both parallel and divergent fields. The calculation for divergent fields is not very efficient, and will give no terma in lower voxels if the beam is angulated such that the beam is at least a whole voxel width wider than at the surface eg. at 100 cm SSD, for a 20×20 cm^2 field, using 0.5 cm wide voxels, the depth where the beam becomes wider than a voxel width is 5 cm.

A.2.7 c_input_tracks.c

c_input_tracks.c reads in the pre-generated Monte Carlo electron track data, and converts the x, y, z co-ordinates to $\Delta x, \Delta y, \Delta z$ and inputs flag, E and E_{dep}. $\Delta\theta$ and $\Delta\phi$ are also calculated if the ELECTRON option is used.

A.2.8 t_calc_prim_dose.c

t_calc_prim_dose.c transports the pre-generated electron tracks from a user defined number of points within each voxel with positive terma (generally from the centre of the voxel

only) by calling *transport_elec*. In *transport_elec* each electron is transported NUM_ELEC times and records the energy deposited in en_dep_grid. This program is continually evolving and changing over time as I try to include more accurate physics, and squeeze computation time.

A.2.9 t_calc_scat_dose.c

t_calc_scat_dose.c calculates the scattered dose due to superposition if the Super-Monte Carlo method is used.

A.2.10 c_calc_dose.c

c_calc_dose.c calculates the superposition dose (using either the FE_SCALING, NO_SCALING, Z_SCALING and RAY_TRACE options).

A.3 Changes

7 Oct 95	Reduced *t_calc_prim_dose* differentiating between electrons and photons.
9 Oct 95	Included variable NUM_ELEC to choose whether electron is transported 1,2,3 or 4 times.
12 Oct 95	Included structure DATA to make assigning scattering and stopping power values more efficient.

12 Oct 95 Made file *c_input.h* which is the subset of *c_convolution.h* which can change at each run time. Still not ideal (better way would be as Mackie did it so don't need to recompile when a header file is changed) but better than before.

6 Nov 95 Changed *c_input_tracks.c* and *t_calc_prim_dose.c* to explicitly account for the scattering of δ-rays.

10 June 96 Changed *t_calc_prim_dose.c* to initiate the electrons in a rasta fashion from the boundary surface. This eliminated the discrepency in the penumbra between SMC and Monte Carlo observed when all the electrons were initiated from the centre of the voxel.

15 June 96 Changed boundary crossing algorithm in *t_calc_prim_dose.c* to allow for transport through air by stepping the electron up to a boundary, and then restarting from the boundary as a new step with smaller step length and energy, but the same direction.

Appendix B

Using Restricted Stopping Powers to Vary Electron Step Length

Strictly, as δ-ray production and bremsstrahlung production are explicitly modeled in EGS4 when producing the electron tracks, the stopping power ratio used should be a sum of the restricted collision stopping power, $(L_\Delta)_k^w$ [where Δ = AE = 10 keV], plus the restricted radiative stopping power, $(L_{rad,\Delta'})_k^w$ [where Δ' = AP = 10 keV], ie.

$$S_k^w = (L_\Delta)_k^w + (L_{rad,\Delta'})_k^w \,. \tag{B.1}$$

The restricted radiative stopping power is the radiative stopping power due only to bremsstrahlung interactions below Δ'.

However, in this work only the collision stopping was used because:
(i) L_{10keV} is approximately 0.8 of S_{col},[25] whereas $L_{rad,10keV}$ is only a small fraction of S_{rad} (calculated by replacing the upper limits of the integrals of Eq. 9.1 in ICRU 37[26] with Δ', and using the cross sectional data from Berger and Seltzer[27]), therefore

$L_{rad,10keV}$ can be neglected, and

(ii) $(L_{10keV})_k^w$ / $(S_{col})_k^w$ for aluminium differs by less than 1% from 0.5 to 20 MeV.[26]

Hence the use of $(S_{col})_k^w$ to scale step length.

Appendix C

Changing the Electron Step Scattering Angle in Non-waterlike Media

To fully account for the change in electron scattering angle between the electron steps **A** and **B**, four angles are needed: α, the azimuthal angle of **A** with respect to (wrt) the beam axis frame; Ω, the polar angle of **A** wrt the beam axis frame; ϕ, the azimuthal angle of **B** wrt $\hat{\mathbf{A}}$ (the frame of vector **A**); and θ, the polar angle of **B** wrt $\hat{\mathbf{A}}$.

α is found from the x and y components of vector **A**, A_x and A_y respectively,

$$\alpha = \tan^{-1} \frac{A_y}{A_x}. \tag{C.1}$$

As the $\tan^{-1}$ function is only defined between $-\pi/2$ and $\pi/2$, α may have π added or subtracted depending on the sign of A_x and A_y (this is also the case when calculating ϕ).

Ω is obtained from

$$\Omega = \tan^{-1} \frac{\sqrt{A_x^2 + A_y^2}}{A_z} \tag{C.2}$$

θ_w can be determined from the scalar product of $\mathbf{A}$ and $\mathbf{B}$,

$$\theta_w = \cos^{-1} \left(\frac{\mathbf{A}.\mathbf{B}}{AB} \right). \tag{C.3}$$

To calculate ϕ_w, a co-ordinate transformation using angles α and Ω from the beam axis frame into the $\hat{\mathbf{A}}$ frame is necessary,

$$\mathbf{B}' = S\mathbf{B}, \tag{C.4}$$

where $S = \begin{bmatrix} \cos\Omega\cos\alpha & \cos\Omega\sin\alpha & -\sin\Omega \\ -\sin\alpha & \cos\alpha & 0 \\ \sin\Omega\cos\alpha & \sin\Omega\sin\alpha & \cos\Omega \end{bmatrix}$.

Hence ϕ_w is obtained from

$$\phi_w = \tan^{-1} \frac{B'_y}{B'_x}. \tag{C.5}$$

In the frame of $\hat{\mathbf{A}}$, in medium k, the polar scattering angle θ_k is obtained by

$$\theta_k = \theta_w \times \sqrt{(T)_w^k \, S_{col}(E)_k^w}, \tag{C.6}$$

as shown in section II.B. (As stated previously, the $\sqrt{S_{col}(E)_k^w}$ term is used because the electron step lengths have been altered by the change in scattering power.) Hence, when accounting for the different θ in medium k, vector

$$\mathbf{B}' = B \begin{bmatrix} \sin\theta_w\cos\phi_w \\ \sin\theta_w\sin\phi_w \\ \cos\theta_w \end{bmatrix} \tag{C.7}$$

becomes

$$\mathbf{B}'' = B \begin{bmatrix} \sin\theta_k \cos\phi_w \\ \sin\theta_k \sin\phi_w \\ \cos\theta_k \end{bmatrix}. \tag{C.8}$$

A co-ordinate transformation is needed to revert back to the beam axis frame. Hence, vector $\mathbf{B}$ in the beam axis frame becomes

$$\mathbf{B} = S^{-1}\mathbf{B}'', \tag{C.9}$$

as shown schematically in Fig. 5.6.

Bibliography

[1] I. Castle. *Year Book Australia 1995.* Australian Bureau of Statistics, Canberra, 1995.

[2] E. J. Hall. The biological basis of altered fractionation patterns- accelerated treatment and hyperfractionation. In *Clinical Oncological Society of Australia Conference Proceedings*, page 93, 1994. Abstract.

[3] International Commission on Radiation Units and Measurements. *Determination of absorbed dose in a patient with beams of X or gamma rays in radiation procedures*, volume 24. ICRU, Bethesda, Maryland, 1976.

[4] A. L. Boyer and T. Schultheiss. Effects of dosimetric and clinical uncertainty on complication-free local tumour control. *Rad. Onc.*, 11:65–71, 1988.

[5] J. E. Cunningham. Tissue inhomogeneity corrections in photon beam treatment planning. In C. G. Orton, editor, *Progress in Medical Radiation Physics*, volume 1, pages 103–131. Plenum Publishers, 1982.

[6] P. E. Metcalfe, T. P. Y. Wong, and P. W. Hoban. Radiotherapy x-ray beam inhomogeneity corrections: the problem of lateral electronic disequilibrium in lung. *Aust. Phys. Eng. Sci. Med.*, 16(4):155–67, 1993.

[7] J. Cygler, J. J. Battista, J. W. Scrimger, E. Mah, and J. Antolak. Electron dose distributions in experimental phantoms: a comparison with 2D pencil beam calculations. *Phys. Med. Biol.*, 32(9):1073–1086, 1987.

[8] W. R. Nelson, H. Hirayama, and D. W. O. Rogers. *The* EGS4 *Code System.* Stanford Linear Accelerator Centre, 1985. Publication 265.

[9] M. J. Berger and S. M. Seltzer. ETRAN, *Monte Carlo code system for electron and photon transport through extended media. Documentation for RSIC Computer Code Package CCC-107.* Oak Ridge National Laboratories, 1973.

[10] L. Eyges. Multiple scattering with energy loss. *Phys. Rev.*, 74:1534–1535, 1948.

[11] H. E. Johns and J. R. Cunningham. *The Physics of Radiology.* Thomas Springfield Press, Illinois, 4th edition, 1983.

[12] F. M. Khan. *The Physics of Radiation Therapy.* Williams and Wilkins, Baltimore, Maryland, 1994. Second edition.

[13] W. Heitler. *The Quantum Theory of Radiation.* Oxford University Press, New York, 1954.

[14] International Commission on Radiation Units and Measurements. *Radiation Quantities and Units*, volume 33. ICRU, Washington, D.C., 1980.

[15] F. H. Attix. The partition of kerma to account for bremsstrahlung. *Health Phys.*, 36:347–354, 1979.

[16] A. Ahnesjö, P. Andreo, and A. Brahme. Calculation and application of point spread functions for treatment planning with high energy photon beams. *Rad. Onc.*, 26:49–56, 1987.

[17] P. J. Keall. The angular and energy distribution of a 15 MeV electron beam. Master's thesis, University of Adelaide, Adelaide, 1994.

[18] C. Møller. Passage of hard beta-rays through matter. *Ann. Physik*, 14:531, 1932.

[19] H. J. Bhahba. Scattering of positrons by electrons with exchange on Dirac's theory of the positron. In *Proc. Roy. Soc. A154*, page 195, 1936.

[20] M. J. Berger and S. M. Seltzer. *Tables of Energy Losses and Ranges of Electrons and Positrons.* National Aeronautics and Space Agency Publication SP-3036, Washington, D.C., 1964.

[21] R. P. Feynman, R. B. Leighton, and M. Sands. *The Feynman Lectures on Physics.* Addison-Wesley, Reading, Massachusetts, 1964.

[22] A. E. Nahum. The interaction of electrons with matter. In A. E. Nahum, editor, *The Computation of Dose Distributions in Electron Beam Radiotherapy.* UMEA University, 1985. Lecture 3.

[23] B. B. Rossi. *High Energy Particles.* Prentice Hall, New York, 1952.

[24] H. W. Koch and J. W. Motz. Bremsstrahlung cross-section formulas and related data. *Rev. Mod. Phys.*, 31:921, 1959.

[25] International Commission on Radiation Units and Measurements. *Radiation Dosimetry: Electrons with Initial Energies Between 1 and 50 MeV*, volume 35. ICRU, Bethesda, Maryland, 1984.

[26] International Commission on Radiation Units and Measurements. *Stopping Powers for Electrons and Positrons*, volume 37. ICRU, Bethesda, Maryland, 1984.

[27] M. J. Berger and S. M. Seltzer. Bremsstrahlung energy spectra from electrons with kinetic energy 1 keV - 10 GeV incident on screened nuclei and orbital electrons of neutral atoms with Z = 1-100. *At. Data Nucl. Data Tables*, 35:345–418, 1986.

[28] P. Andreo. The interaction of electrons with matter. In A. E. Nahum, editor, *The Computation of Dose Distributions in Electron Beam Radiotherapy.* UMEA University, 1985.

[29] G. Starkschall, A. S. Shiu, S. W. Bugnowski, L. L. Wang, D. A. Low, and K. R. Hogstrom. Effect of dimensionality of heterogeneity corrections on the implementation of a three dimensional electron pencil-beam algorithm. *Phys. Med. Biol.*, 36(2):207–27, 1991.

[30] P. W. Hoban. *Lateral Electron Disequilibrium in Radiotherapy Treatment Planning.* PhD thesis, University of Waikato, 1991.

[31] W. A. McKinley and H. Feshback. *Phys. Rev.*, 74:1759, 1948.

[32] S. Goudsmit and J. L. Saunderson. Multiple scattering of electrons. *Phys. Rev.*, 57:24–29, 1940.

[33] G. Molière. Theorie die Strueuung schneller geladener Teilchen I: Einzelstreuung am abgeschirmten Coulomb field. *Z. Naturforsch*, 2a:133–145, 1947.

[34] G. Molière. Theorie die Strueuung schneller geladener Teilchen II: Mehrfach and Vielfachstreuung. *Z. Naturforsch*, 3a:78–97, 1948.

[35] B. B. Rossi and K. Greisen. Cosmic ray theory. *Rev. Mod. Phys.*, 15:240, 1941. Fermi's work is given on pages 265-268.

[36] J. McLellan, G. A. Sandison, L. Papiez, and W. Huda. A restricted angular scattering model for electron penetration in dense media. *Med. Phys.*, 18(1):1–7, 1991.

[37] D. Jette, L. H. Lanzl, and M. Rosenfeld. The application of multiple scattering theory to therapeutic electron dosimetry. *Med. Phys.*, 10(2):141–146, 1983.

[38] K. R. Hogstrom. Evaluation of electron pencil beam dose calculation. *Med. Phys.*, 12(4):554, 1985. Abstract.

[39] A. Brahme. Multiple scattering of relativistic electrons in air. TRITA-EPP 71-22. Technical report, Royal Inst. Tech., Stockholm, 1971.

[40] E. J. Hall. *Radiobiology for the Radiologist.* J. B. Lippincott, Philadelphia, 1994.

[41] C. K. Ross and N. V. Klassen. Water calorimetry for radiation dosimetry. *Phys. Med. Biol.*, 41(1):1–29, 1996.

[42] C. J. Karzmark, C. S. Nunan, and E. Tanabe. *Medical electron accelerators.* McGraw Hill, New York, 1993.

[43] R. Mohan, C. Chui, and L. Lidofsky. Energy and angular distributions of photons from medical linear accelerators. *Med. Phys.*, 12(5):592–97, 1985.

[44] P. W. Hoban, D. C. Murray, and W. H. Round. Photon beam convolution using polyenergetic energy deposition kernels. *Phys. Med. Biol.*, 39:669–685, 1994.

[45] M. A. Ebert, November 1995. Personal communication.

[46] P. J. Keall and P. W. Hoban. The angular and energy distribution of the primary electron beam. *Aust. Phys. Eng. Sci. Med.*, 17(3):116–123, 1994.

[47] B. L. Werner, F. M. Khan, and F. C. Deibel. A model for calculating electron beam scattering in treatment planning. *Med. Phys.*, 9(2):180–7, 1982.

[48] P. E. Metcalfe and W. A. Beckham. Radiotherapy planning accuracy in terms of C.T. numbers and inhomogeneity correction techniques. *Aust. Rad.*, 32(3):371–379, 1988.

[49] S. Webb. *The Physics of Three Dimensional Radiation Therapy.* Institute of Physics Publishing, Bristol, 1993.

[50] D. W. O. Rogers, B. A. Fadeggon, G. X. Ding, C.-M. Ma, T. Wei, and T. R. Mackie. BEAM: A Monte Carlo code to simulate radiotherapy treatment units. *Med. Phys.*, 22:503–24, 1995.

[51] P. W. Hoban and P. J. Keall. Accounting for electron applicator scatter in Monte Carlo calculations. In *APSEM Conference Proceedings*, 1993.

[52] P. J. Keall and P. W. Hoban. Determination of the angular distribution of a clinical electron beam. In *APSEM Conference Proceedings*, 1993.

[53] E. W. Korevaar, J. J. Janssen, P. R. M. Storchi, and H. Huizenga. Description of a clinical electron beam: The initial phase space as input of the phase space evolution model. *Med. Phys.*, 22(6):948, 1995. Abstract.

[54] M. A. Ebert and P. W. Hoban. A model for electron beam applicator scatter. *Med. Phys.*, 22(9):1419–1429, 1995.

[55] M. A. Ebert and P. W. Hoban. A Monte Carlo investigation of electron beam applicator scatter. *Med. Phys.*, 22(9):1431–1435, 1995.

[56] M. R. Sontag and J. R. Cunningham. The equivalent tissue-air ratio method for making absorbed dose calculations in heterogeneous medium. *Radiology*, 129:787–794, 1978.

[57] J. E. O'Connor. The variation of scattered x-rays with density in an irradiated body. *Phys. Med. Biol.*, 1(4):352–369, 1957.

[58] J. W. Wong and R. M. Henkelman. A new approach to ct pixel-based photon dose calculations in heterogeneous media. *Med. Phys.*, 10(2):199–208, 1983.

[59] J. R. Cunningham. Scatter-air ratios. *Phys. Med. Biol.*, 17:42–51, 1972.

[60] D. W. O. Rogers and A. F. Bielajew. Experimental benchmarks of EGS. In T. M. Jenkins, W. R. Nelson, and A. Rindi, editors, *Monte Carlo Transport of Electrons and Photons*, pages 307–321. Plenum, 1988.

[61] P. Andreo. Monte Carlo techniques in medical radiation physics. *Phys. Med. Biol.*, 36(7):861–920, 1991.

[62] D. C. Murray. *The Application of Parallel Processing to Radiotherapy Dose Computation.* PhD thesis, University of Waikato, 1991.

[63] W. R. Nelson and D. W. O. Rogers. Structure and operation of the EGS4 code system. In T. M. Jenkins, W. R. Nelson, and A. Rindi, editors, *Monte Carlo Transport of Electrons and Photons*, pages 287–307. Plenum, 1988.

[64] S. M. Seltzer. An overview of ETRAN Monte Carlo methods. In T. M. Jenkins, W. R. Nelson, and A. Rindi, editors, *Monte Carlo Transport of Electrons and Photons*, pages 153–182. Plenum, 1988.

[65] J. A. Halblieb and T. A. Mehlhorn. ITS: the integrated tiger series of coupled electron/photon transport codes. Technical report, Sandia National Laboratories Report Publication SAND84-0573, 1984.

[66] J. A. Halblieb. Structure and operation of the ITS code system. In T. M. Jenkins, W. R. Nelson, and A. Rindi, editors, *Monte Carlo Transport of Electrons and Photons*, pages 249–262. Plenum, 1988.

[67] J. F. Briesmeister (ed). MCNP- *A General Monte Carlo Code for Neutron and Photon transport, Version 3A*. Los Alamos National Laboratory, 1986. LA-7369-M, Rev. 2.

[68] C. L. Hartmann-Siantar, W. P. Chandler, M. B. Chadwick, H. M. Blann, L. J. Cox, D. A. Resler, J. A. Rathkopf, T. R. Mackie, J. V. Siebers, M. A. Ross, P. M. DeLuca Jr., K. A. Weaver, and R. M. White. Dose distributions calculated with the PEREGRINE all-particle Monte Carlo code. *Med. Phys.*, 22(6):994, 1995. Abstract.

[69] K. A. Weaver, C. L. Hartmann-Siantar, and W. P. Chandler. Clinical brachytherapy calculations with a CT based Monte Carlo code. *Med. Phys.*, 22(6):942, 1995.

[70] K. R. Shortt, C. K. Ross, A. F. Bielajew, and D. W. O. Rogers. Electron beam dose distributions near standard inhomogeneities. *Phys. Med. Biol.*, 31(3):235–249, 1986.

[71] H.A. Bethe. Molière's theory of multiple scattering. *Phys. Rev.*, 89:1256–1266, 1953.

[72] M. J. Berger. ETRAN- experimental benchmarks. In T. M. Jenkins, W. R. Nelson, and A. Rindi, editors, *Monte Carlo Transport of Electrons and Photons*, pages 183–219. Plenum, 1988.

[73] L. V. Spencer. *Energy Dissipation by Fast Electrons.* National Bureau of Standards, 1959. Monograph 1.

[74] W. L. McLaughlin and E. K. Hussman. *The Measurement of Electron and Gamma-ray Dose Distributions in Various Media, Large Radiation Sources for Industrial Processes.* Int. Atom. Energy Agency Pub. IAEA sm-123/43, 1969.

[75] M. J. Berger. Monte Carlo calculation of the penetration and diffusion of fast charged particles. In *Methods of Computational Physics volume I*, page 135. Academic Press, New York, 1963.

[76] A. F. Bielajew and D. W. O. Rogers. A comparison of EGS and ETRAN. In T. M. Jenkins, W. R. Nelson, and A. Rindi, editors, *Monte Carlo Transport of Electrons and Photons*, pages 323–342. Plenum, 1988.

[77] D. C. Murray. Using EGS4 Monte Carlo in medical radiation physics. *Aust. Phys. Eng. Sci. Med.*, 13(3):128–37, 1990.

[78] A. F. Bielajew and D. W. O. Rogers. Variance reduction techniques. In T. M. Jenkins, W. R. Nelson, and A. Rindi, editors, *Monte Carlo Transport of Electrons and Photons*, pages 407–434. Plenum, 1988.

[79] J. Baró, J. Sempeau, J. M. Fernandez-Varea, and F. Salvat. PENELOPE: An algorithm for Monte Carlo simulations of the penetration and energy loss of electrons and positrons in matter. *Nucl. Instr. Meth.*, 100:31–49, 1995.

[80] E. O. Brigham. *The Fast Fourier Transform and its Applications.* Prentice-Hall, Singapore, 1988.

[81] A. Ahnesjö. Collapsed cone convolution of radiant energy for photon dose calculation in heterogeneous media. *Med. Phys.*, 16:577–592, 1989.

[82] A. Ahnesjö, M. Saxner, and A. Trepp. A pencil beam model for photon dose calculation. *Med. Phys.*, 19:263–273, 1992.

[83] A. L. Boyer and E. C. Mok. A photon dose distribution model employing convolution calculations. *Med. Phys.*, 12:169–177, 1985.

[84] A. L. Boyer and E. C. Mok. Calculation of photon dose distributions in an inhomogeneous media using convolutions. *Med. Phys.*, 13:503, 1986.

[85] T. R. Mackie. *The study of megavoltage X-ray beams.* PhD thesis, University of Alberta, 1985.

[86] T. R. Mackie, J. W. Scrimger, and J. J. Battista. A convolution method of calculating dose for 15 MV X-rays. *Med. Phys.*, 12(2):188–96, 1985.

[87] T. R. Mackie, A. F. Bielajew, D. W. O. Rogers, and J. J. Battista. Generation of photon energy deposition kernels using the EGS Monte Carlo code. *Phys. Med. Biol.*, 33(1):1–20, 1988.

[88] P. W. Hoban, D. C. Murray, P. E. Metcalfe, and W. H. Round. Superposition dose calculation in lung for 10 MV photons. *Aust. Phys. Eng. Sci. Med.*, 13(2):81–92, 1990.

[89] P. E. Metcalfe, P. W. Hoban, D. C. Murray, and W. H. Round. Modelling polychromatic high energy photon beams by superposition. *Aust. Phys. Eng. Sci. Med.*, 12(3):138–48, 1989.

[90] R. Mohan, C. Chui, and L. Lidofsky. Differential pencil beam dose computation model for photons. *Med. Phys.*, 13:64–73, 1986.

[91] M. B. Sharp and J. J. Battista. Dose calculations using convolution and superposition principles: The orientation of dose spread kernels in divergent x-ray beams. *Med. Phys.*, 20(6):1685–94, 1993.

[92] T. Bortfeld, W. Schlegel, and B. Rhein. Decomposition of pencil beam kernels for fast dose calculations in three-dimensional treatment planning. *Med. Phys.*, 20(2):311–318, 1993.

[93] B.J. Salter. Extraction of pencil beam kernels by simulated annealing optimisation. *Med. Phys.*, 22(6):977, 1995. Abstract.

[94] Y. Zhu L. Wang and D. Jette. Analytic modeling of the primary X-ray dose deposition kernels. *Med. Phys.*, 22(6):977, 1995. Abstract.

[95] M. K. Woo and J. R. Cunningham. The validity of the density scaling method in primary electron transport for electron and photon beams. *Med. Phys.*, 17(2):187–194, 1990.

[96] M. K. Woo, J. R. Cunningham, and J.J. Jezioranski. Extending the concept of primary and scatter separation to the condition of electronic disequilibrium. *Med. Phys.*, 17(4):588–95, 1990.

[97] R. Mohan and C. Chui. Validity of the concept of separating primary and scatter dose. *Med. Phys.*, 12(6):726–30, 1985.

[98] N. Papanikalaou, T. R. Mackie, C. Meger-Wells, M. Gehring, and P. Reckwerdt. Investigation of the convolution method for polyenergetic spectra. *Med. Phys.*, 20(5):1327–36, 1994.

[99] P. W. Hoban. Accounting for the variation in collision kerma to terma ratio in polyenergetic photon beam convolution. *Med. Phys.*, 22(12):2035–2044, 1996.

[100] P. J. Reckwerdt and T. R. Mackie. Superposition/Convolution speed improvements using run-length raytracing. *Med. Phys.*, 19:784, 1992. Abstract.

[101] HELAX AB. Uppsala, Sweden.

[102] ADAC Laboratories. 540 Alder Drive, Milpitas, California, USA.

[103] R. Mohan and C. Chui. Use of fast Fourier transforms in calculating dose distributions for irregularly shaped fields for three-dimensional treatment planning. *Med. Phys.*, 14:70–77, 1987.

[104] G. C. Field and J. J. Battista. Photon dose calculations using convolution in real and Fourier space: Assumptions and estimates. In I. A. D. Bruinvis, P. H. van der Giessen, H. J. van Kleffens, and F. W. Wittkämper, editors, *The Use of Computers in Radiation Therapy*, pages 103–106. Elsevier Science Publications, North Holland, 1987.

[105] A. L. Boyer, R. Wackwitz, and E. C. Mok. A comparison of the speed of three convolution algorithms. *Med. Phys.*, 15(2):224–227, 1988.

[106] A. L. Boyer, Y. Zhu, L. Wang, and P. Francois. Fast Fourier transform convolution calculations of x-ray isodose distributions in homogeneous media. *Med. Phys.*, 16(2):248–253, 1989.

[107] D. C. Murray, P. W. Hoban, P. E. Metcalfe, and W. H. Round. 3-d Superposition for radiotherapy treatment planning using fast Fourier transforms. *Aust. Phys. Eng. Sci. Med.*, 13(3):128–137, 1989.

[108] J. Battista and M. B. Sharpe. True 3-D dose computation for megavoltage X-ray therapy: A role for the superposition principle. *Aust. Phys. Eng. Sci. Med.*, 15:159–78, 1992.

[109] N. Papanikalaou and T. R. Mackie. Extension of the convolution/superposition based algorithm to include atomic number effect superposition. *Med. Phys.*, 22(6):977, 1995.

[110] I. Kawrakow, M. Fippel, and K. Friedrich. 3D electron dose calculation using a Voxel-based Monte Carlo algorithm (VMC). *Med. Phys.*, 23(4):445–457, 1996.

[111] K. Kawachi. Calculation of electron dose distribution for radiotherapy treatment planning. *Phys. Med. Biol.*, 20(4):571–577, 1975.

[112] K. R. Hogstrom, M. D. Mills, and P. R. Almond. Electron beam dose calculations. *Phys. Med. Biol.*, 26(3):445–459, 1981.

[113] A. Brahme, I. Lax, and P. Andreo. Electron beam dose planning using discrete Gaussian beams: Mathematical background. *Acta Rad. Onc.*, 20:147–158, 1981.

[114] I. A. D. Bruinvis, A. van Amstel, A. J. Elevelt, and R. van der Laarse. Calculation of electron beam dose distributions for arbitrarily shaped fields. *Phys. Med. Biol.*, 28(6):667–683, 1983.

[115] K. R. Hogstrom, M. D. Mills, J. A. Meyer, J. R. Palta, D. E. Mellenberg, R. T. Meoz, and R. S. Fields. Dosimetric evaluation of a pencil-beam algorithm for electrons employing a two-dimensional heterogeneity correction. *Int. J. Rad. Onc. Biol. Phys.*, 10(4):561–569, 1984.

[116] I. Lax and A. Brahme. Electron beam dose planning using Gaussian beams: Energy and spatial scaling with inhomogeneities. *Acta Rad. Onc.*, 24:75–85, 1985.

[117] I. Lax. A generalised Gaussian model for electron beam dose planning. In A. E. Nahum, editor, *The Computation of Dose Distributions in Electron Beam Radiotherapy.* UMEA University, 1985. Lecture 12.

[118] H. M. Kooy and H. Rashid. A three-dimensional electron pencil beam algorithm. *Phys. Med. Biol.*, 34(2):229–243, 1989.

[119] E. Mah, J. Antolak, J. W. Scrimger, and J. J. Battista. Experimental evaluation of a 2D and 3D electron pencil beam algorithm. *Phys. Med. Biol.*, 34(9):1179–1194, 1989.

[120] P. R. M Storchi and H. Huizenga. On a numerical approach of the pencil beam. *Phys. Med. Biol.*, 30(5):467–473, 1985.

[121] A. S. Shiu and K. R. Hogstrom. A pencil beam redefinition algorithm for electron dose distributions. In I. A. D. Bruinvis, P. H. van der Giessen, H. J. van Kleffens, and F. W. Wittkämper, editors, *The Use of Computers in Radiation Therapy*, pages 445–448. Elsevier Science Publications, North Holland, 1987.

[122] A. S. Shiu and K. R. Hogstrom. Pencil beam redefinition algorithm for electron dose distributions. *Med. Phys.*, 18(1):7–18, 1991.

[123] D. J. Perry and J. G. Holt. A model for calculating the effects of small inhomogeneities on electron beam dose distribution. *Med. Phys.*, 7:207–215, 1980.

[124] C. X. Yu, W. S. Ge, and J. W. Wong. A multiray model for calculating electron pencil beam dose distribution. *Med. Phys.*, 15:662–671, 1988.

[125] D. Jette. Second-order multiple scattering theory for charged particle teletherapy beams. *Med. Phys.*, 12(2):178–182, 1985.

[126] D. Jette. Electron dose calculation using multiple scattering theory. A. Gaussian multiple scattering theory. *Med. Phys.*, 15(2):123–137, 1988.

[127] D. Jette and A. F. Bielajew. Electron dose calculation using multiple scattering theory: Second-order multiple scattering theory. *Med. Phys.*, 16(5):698–711, 1989.

[128] D. Jette, L. H. Lanzl, A. Pagnamenta, M. Rozenfeld, D. Bernard, M. Kao, and A. M. Sabbas. Electron dose calculation using multiple scattering theory: Thin planar inhomogeneities. *Med. Phys.*, 16(5):712–725, 1989.

[129] D. Jette. Electron dose calculation using multiple scattering theory: Localised inhomogeneities- A new theory. *Med. Phys.*, 18(2):123–132, 1991.

[130] D. Jette and S. Walker. Electron dose calculation using multiple scattering theory: Evaluation of a new model for inhomogeneities. *Med. Phys.*, 19(5):1241–1254, 1992.

[131] D. Jette. Incorporation of single scattering into Gaussian multiple-scattering theory. *Med. Phys.*, 22(6):1006, 1995. Abstract.

[132] H. Huizenga and P. R. M. Storchi. Numerical calculation of energy deposition by broad high-energy electron beams. *Phys. Med. Biol.*, 34(10):1371–96, 1989.

[133] M. Morawska-Kaczyńska and H. Huizenga. Numerical calculation of energy deposition by broad high-energy electron beams: II. Multi-layered geometry. *Phys. Med. Biol.*, 37(11):2103–16, 1992.

[134] J. J. Janssen, D. E. J. Riedeman, M. Morawska-Kaczyńska, P. R. M. Storchi, and H. Huizenga. Numerical calculation of energy deposition by broad high-energy electron beams: III. Three-dimensional heterogeneous media. *Phys. Med. Biol.*, 39:1351–66, 1994.

[135] T. R. Mackie. Calculating electron dose using a superposition/convolution method. In I. A. D. Bruinvis, P. H. van der Giessen, H. J. van Kleffens, and F. W. Wittkämper, editors, *The Use of Computers in Radiation Therapy*, pages 445–448. Elsevier Science Publications, North Holland, 1987.

[136] P. Bloch. A unified electron/photon approach. *Phys. Med. Biol.*, 33(3):373–377, 1988.

[137] M. D Altschuler, P. Bloch, E. L. Buhle, and S. Ayyalasomayajula. 3D dose calculations for electron and photon beams. *Phys. Med. Biol.*, 37(2):391–411, 1992.

[138] H. Neuenschwander and E. J. Born. A macro Monte Carlo method for electron beam dose calculations. *Phys. Med. Biol.*, 37(1):107–125, 1992.

[139] H. Neuenschwander, T. R. Mackie, and P. J. Reckwerdt. `MMC`- a high performance Monte Carlo code for electron beam treatment planning. *Phys. Med. Biol.*, 40:543–574, 1995.

[140] P. R. Almond, A. E. Wright, and M. L. M. Boone. High energy electron dose perturbations in regions of tissue heterogeneity. II. Physical models for tissue heterogeneities. *Radiology*, 88:1146–1153, 1967.

[141] F. M. Khan, K. P. Doppke, K. R. Hogstrom, G. J. Kutcher, R. Nath, S. C. Prasad, J. A. Purdy, M. Rozenfeld, and B. L. Werner. Clinical electron-beam dosimetry: Report of AAPM Radiation Therapy Committee Task Group No. 25. *Med. Phys.*, 18(1):73–109, 1991.

[142] I. A. D. Bruinvis, W. A. F. Mathol, and P. Andreo. Inclusion of electron range straggling in the Fermi-Eyges multiple scattering theory. In I. A. D. Bruinvis, P. H. van der Giessen, H. J. van Kleffens, and F. W. Wittkämper, editors, *The Use of Computers in Radiation Therapy*, pages 133–136. Elsevier Science Publications, North Holland, 1987.

[143] I. Lax. Inhomogeneity corrections in electron-beam dose planning: Limitations with the semi-infinite slab approximation. *Phys. Med. Biol.*, 31(8):879–892, 1986.

[144] A. Brahme. Current algorithms for computed electron beam dose planning. *Rad. Onc.*, 3:347–362, 1985.

[145] I. Lax, A. Brahme, and P. Andreo. Electron dose planning using Gaussian beams. *Acta Rad. Supp.*, 364:49–59, 1983.

[146] M. J. Berger and S. M. Seltzer. *Tables of Energy-Deposition Distributions in Water Phantoms Irradiated by Point-Monodirectional Electron Beams with Energies from 1 to 60 MeV, and Applications to Broad Beams. NS-BIR 82-2541.* National Bureau of Standards, Washington D. C., 1982.

[147] J. Antolak, E. Mah, and J. W. Scrimger. Optimization of pencil beam widths for electron beam dose calculations. *Med. Phys.*, 22(4):411–419, 1995.

[148] A. F. Bielajew, J. Cygler, and J. J. Battista. A comparison of electron pencil beam and Monte Carlo calculation methods. In I. A. D. Bruinvis, P. H. van der Giessen, H. J. van Kleffens, and F. W. Wittkämper, editors, *The Use of Computers in Radiation Therapy*, pages 65–68. Elsevier Science Publications, North Holland, 1987.

[149] L. Landau. On the energy loss of fast charged particles by ionisation. *J. Phys*, 8:201–205, 1944.

[150] M. C. Cordaro and M. S. Zucker. A method for solving time dependent electron transport problems. *Nucl. Eng. Sci.*, 45:107–116, 1971.

[151] M. K. Woo and J. R. Cunningham. Comments on a unified electron/photon dosimetry approach. *Phys. Med. Biol.*, 33(8):981–982, 1988. Letter to editor.

[152] T. R. Mackie and J. J. Battista. A macroscopic Monte Carlo method for electron beam dose calculations: a proposal. In *Proc. 8th Conf. on Use of Computers in Radiation Therapy*, pages 123–127, 1984.

[153] D. R. White, C. Constantinou, and R. J. Martin. Foamed epoxy resin-based lung substitutes. *Brit. J. Rad.*, 59:732–8, 1986.

[154] I. Kawrakow. Improving modeling of multiple scattering in the `VMC` model. *Nuc. Instr. Meth.*, B, 1996. In press.

[155] I. Kawrakow. Electron transport: lateral and longitudinal correlation algorithm. *Nuc. Instr. Meth.*, B, 1996. Submitted.

[156] C. X. Yu, T. R. Mackie, and J. W. Wong. Photon dose calculation incorporating explicit electron transport. *Med. Phys.*, 22(7):1157–1165, 1995.

[157] A. F. Bielajew and D. W. O. Rogers. `PRESTA`: The parameter reduced electron step transport algorithm for electron Monte Carlo transport. *Nuc. Instr. Meth.*, B 18:165–171, 1987.

[158] T. Knöös, A. Ahnesjö, P. Nilsson, and L. Weber. Limitations of a pencil beam approach to photon dose calculations in lung tissue. *Phys. Med. Biol.*, 40:1411–1420, 1995.

[159] International Commission on Radiological Protection. *Report of the Task Group on Reference Man*, volume 23. Pergamon Press, New York, 1974.

[160] S. N. Rustgi and J. E. Rodgers. Analysis of the bremsstrahlung component in 6-18 MeV electron beams. *Med. Phys.*, 14(5):884–8, 1987.

[161] A. H. Brahme and A. K. Ågren. Optimal dose distribution for eradication of heterogeneous tumours. *Acta Oncologica*, 26:377–385, 1987.

[162] G. J. Kutcher, C. Burman, L. Brewster, M. Goitein, and R. Mohan. Histogram reduction method for calculating complication probabilities for three-dimensional treatment planning evaluations. *Int. J. Rad. Onc. Biol. Phys.*, 21:137–146, 1991.

[163] A. Niemerko, M. Urie, and M. Goitein. Optimization of 3D radiation therapy with both physical and biological endpoints. *Int. J. Rad. Onc. Biol. Phys.*, 23:99–108, 1992.

[164] T. R. Mackie, T. Holmes, S. Swerdloff, P. Reckwerdt, J. O. Deasy, J. Yang, B. Paliwal, and T. Kinsella. Tomotherapy: A new concept for the delivery of dynamic conformal radiotherapy. *mp*, 20(6):1709–1719, 1993.

[165] E. P. Lief, A. Larsson, and J. L. Humm. Electron scanning beam intensity modulation. *Med. Phys.*, 22(6):930, 1995. Abstract.

[166] C. X. Yu. Intensity-modulated arc therapy with dynamic multileaf collimation: an alternative to tomotherapy. *Phys. Med. Biol.*, 40:1435–1449, 1995.

[167] T. E. Schultheiss, C. G. Orton, and R. A. Peck. Models in radiotherapy: Volume effects. *Med. Phys.*, 10(4):410–415, 1983.

[168] H. R. Withers, J. M. G. Taylor, and B. Maciejewski. Treatment volume and tissue tolerance. *Int. J. Rad. Onc. Biol. Phys.*, 16:1623–1630, 1988.

[169] D. R. Wigg. A Radiobiological Basis for Bioeffect Planning. Royal Adelaide Hospital, 1990.

[170] A. Niemerko and M. Goitein. Calculation of normal tissue complication probability and dose-volume histogram reduction schemes for tissues with a critical element architecture. *Rad. Onc.*, 20:166–176, 1991.

[171] J. F. Fowler. The volume effect in radiotherapy. *J. Jpn. Soc. Ther. Radiol. Oncol.*, 5:75–87, 1993.